Karlsruher Forschungsberichte aus dem
Institut für Hochleistungsimpuls- und Mikrowellentechnik

Band
21

Adel Omrani Hamzekalaei

Multistatic Uniform Diffraction Tomography and Time-Reversal Algorithms for Microwave Imaging of Multilayered Media

KIT Scientific Publishing

Adel Omrani Hamzekalaei

Multistatic Uniform Diffraction Tomography and Time-Reversal Algorithms for Microwave Imaging of Multilayered Media

Karlsruher Forschungsberichte aus dem
Institut für Hochleistungsimpuls- und Mikrowellentechnik

Herausgeber: Prof. Dr.-Ing. John Jelonnek

Band 21

Multistatic Uniform Diffraction Tomography and Time-Reversal Algorithms for Microwave Imaging of Multilayered Media

by
Adel Omrani Hamzekalaei

KIT Scientific Publishing

Karlsruher Institut für Technologie
Institut für Hochleistungsimpuls- und Mikrowellentechnik

Multistatic Uniform Diffraction Tomography and Time-Reversal Algorithms for Microwave Imaging of Multilayered Media

Zur Erlangung des akademischen Grades eines Doktors der Ingenieurwissenschaften von der KIT-Fakultät für Elektrotechnik und Informationstechnik des Karlsruher Instituts für Technologie (KIT) genehmigte Dissertation

von Adel Omrani Hamzekalaei, M.Sc.

Tag der mündlichen Prüfung: 3. Mai 2024
Hauptreferent: Prof. Dr.-Ing. John Jelonnek
Korreferent: Prof. Dr.-Ing. Mahmoud Shahabadi

Impressum

KIT Scientific Publishing

Karlsruher Institut für Technologie (KIT)
KIT Scientific Publishing
Straße am Forum 2
D-76131 Karlsruhe

www.bibliothek.kit.edu/ksp.php | E-Mail: info@ksp.kit.edu | Shop: www.ksp.kit.edu

Print on Demand 2025 – Gedruckt auf FSC-zertifiziertem Papier

ISSN 2192-2764
ISBN 978-3-7315-1395-7
DOI 10.5445/KSP/1000176182

Foreword of the Editor

In this study, Dr.-Ing. Adel Omrani explores a novel application of microwave imaging to microwave drying systems, addressing the challenges posed by industrial constraints and real-time data collection requirements.

Microwave imaging has long been recognized for its diverse applications, ranging from biomedical imaging to ground-penetrating radar. However, its adaptation to microwave drying systems presents unique obstacles, including signal interference and the need for real-time image reconstruction. Dr.-Ing. Adel Omrani adeptly navigates these challenges, developing innovative imaging algorithms compatible with limited-view antenna arrays and capable of retrieving critical parameters such as dielectric constants.

One of the key contributions of this work is the introduction of the multistatic uniform diffraction tomography (MUDT) algorithm, which enables real-time imaging with a reduced number of antennas while maintaining high spatial resolution. Additionally, Dr.-Ing. Adel Omrani extends the Time Reversal Imaging (TRI) algorithm to address high-contrast scenarios in multilayered media, demonstrating a remarkable advancement in imaging techniques.

Furthermore, Dr.-Ing. Adel Omrani presents a quantitative Bayesian inversion framework for Microwave Tomography (MWT), which integrates with the MUDT method to enhance image quality and extract valuable structural and dielectric information from the imaging domain.

This work represents a significant contribution to microwave imaging, offering innovative solutions to practical challenges and advancing our understanding of microwave drying systems.

Zusammenfassung

Mikrowellen-Bildgebungssysteme werden in verschiedenen Anwendungen umfangreich eingesetzt, z.B. für die biomedizinische Bildgebung, Bodenradar (GPR), Bildgebung durch Wände (TWRI) und zerstörungsfreie Prüfung (NDT). In dieser Arbeit wird eine neue Anwendung der Bildgebung mittels Mikrowellen für Mikrowellentrocknungssysteme beschrieben. Diese Anwendung ist besonders schwierig, da industrielle Mikrowellentrocknungssysteme die Anwendung von Mikrowellenbildgebungssystemen einschränken, weil sie mit den Signalen interferieren, die zur Rekonstruktion des Bildes des Mediums verwendet werden. Zusätzlich erfordert die Echtzeitinspektion des Mediums eine Echtzeitdatenerfassung und eine Echtzeitbildrekonstruktion. In diesem Zusammenhang muss der verwendete Mikrowellenbildgebungsalgorithmus mit einer ausreichend geringen Anzahl von Antennen kompatibel sein. Darüber hinaus ist nicht nur die Lokalisierung der Ziele im Medium wichtig, sondern auch der Wert der zugehörigen Dielektrizitätskonstante ist ein kritischer Parameter für die Bewertung des Prozesses. In dieser Arbeit werden zwei neuartige Bildgebungsalgorithmen entwickelt, die mit einer geringen Anzahl von Antennen und einer beschränkten Anordnung des Antennenarrays kompatibel sind. Eine weitere Technik wird in die entwickelten Bildgebungsalgorithmen integriert, um die Dielektrizitätskonstante der detektierten Ziele im interessierten Medium abzurufen.

Um eine Echtzeitbildrekonstruktion zu erreichen, wird zunächst die Greensche Funktion des geschichteten mehrschichtigen Mediums im spektralen Bereich abgeleitet. Zur Implementierung eines schnellen Bildgebungsalgorithmus wird eine stationäre Phasenapproximation gewählt, um eine geschlossene Form für die Greensche Funktion des mehrschichtigen Mediums herleiten zu können. Ein neuer Bildgebungsalgorithmus, die „Multistatische Gleichmäßige Beugungstomographie (MUDT)“, wird entwickelt, um Änderungen im Dielektrikum in mehrschichtigen Medien zu erfassen.

Der MUDT Algorithmus wird aus der gleichmäßigen Beugungstomographie (UDT) entwickelt. Dieser Algorithmus ermöglicht zwar eine Echtzeitbildgebung, idessen datenbasierte, inverse Streuformulierung mit einem Eingang und einem Ausgang führt jedoch automatisch zu einer zeitaufwändigen Datenerfassung. Darüber hinaus ist die Leistung des UDT Algorithmus mit einer geringen Anzahl von Antennen in den meisten Fällen nicht ausreichend. Demgegenüber ermöglicht der MUDT-Bildgebungsalgorithmus eine Echtzeitbildgebung aus dem betrachteten Medium mit einer geringen Anzahl von Antennen und besserer räumlicher Auflösung.

Im Fall hoher Kontraste, wenn also der Unterschied in den Dielektrizitätskonstanten zweier benachbarter Schichten hoch ist, scheitern viele Bildgebungsalgorithmen daran, die Änderungen im Dielektrikum innerhalb einer Schicht zu rekonstruieren. Dies liegt daran, dass nur die Transmissionanteil der Greenschen Funktion berücksichtigt wird. Um dieses Problem zu lösen, wird in dieser Arbeit ein Zeitumkehr- (TRI)-Algorithmus eingesetzt und erweitert, um Die Änderungen im hochkontrastigen mehrschichtigen Medium zu ermitteln. Für die Anwendung des TRI ist allerdings die genaue, mindestens jedoch näherungsweise ermittelte, dyadische Greensche Funktion (DGF) des Mediums erforderlich. Daher wird in dieser Arbeit ein ungefährer Ausdruck der DGF konstruiert, indem sowohl der Übertragungsals auch der Reflexionsanteil des mehrschichtigen Mediums berücksichtigt werden. Darüber hinaus wird ein neues Ein-Frequenz Verfahren (SF)-TRI-DORT (Dekomposition des TRI-Operators) basierend auf dem Verhalten der Eigenwerte des Zeitumkehroperators (TRO) eingeführt, um eine schnelle Datenerfassung zu erreichen.

Quantitative Mikrowellenbildgebungsmethoden liefern sowohl die Lage als auch die dielektrische Konstante der lokalisierten Objekte in geschichteten Medien. Dies erfordert jedoch im Allgemeinen die Lösung zeitaufwändiger nichtlinearer inverser Probleme. Daher sind diese Methoden nicht für die Echtzeitbildgebung geeignet. In dieser Arbeit wird durch Kenntnis der Lage der Ziele daher ein schneller Optimierungsalgorithmus abgeleitet, indem die Eigenwerte und Eigenvektoren der Streumatrix berechnet werden, um die dielektrische Konstante der lokalisierten Ziele zu erhalten und eine quadratische Fehlerfunktion zu verwenden.

Ein quantitatives Bayessches Netzwerk für Mikrowellentomographie (MWT) wird mit der MUDT-Methode gekoppelt, um (i) die Form zu erhalten, (ii) die dielektrische Konstante der Ziele zu erhalten und (iii) die Bildqualität der Ziele im Vergleich zu den aktuellen Bildgebungsalgorithmen zu verbessern.Im Wesentlichen werden die Informationen aus dem Bayesianischen Inversionsrahmen mit Einzel-Frequenz, unter Verwendung hochauflösender komplementärer struktureller Informationen des Bildgebungsbereichs, durch einen qualitativen Ansatz, den MUDT-Algorithmus, modifiziert. Diese Methode zur Gewinnung vorheriger struktureller Informationen ist effektiv, da sie die Daten aus demselben Mikrowellensensorsystem nutzt.

Abstract

Microwave imaging systems have been extensively used in different applications e.g. for biomedical imaging, ground penetrating radar (GPR), through-the-wall imaging (TWRI), and non-destructing testing (NDT). In this work, a new application of microwave imaging to microwave drying systems is described. This application is particularly difficult, as industrial microwave drying systems limit the application of microwave imaging systems because they interfere with the signals used to reconstruct the image of the medium. Additionally, the real-time inspection of the media demands real-time data collection in addition to real-time image reconstruction. In this regard, the employed microwave imaging algorithm must be compatible with a sufficiently low number of antennas. Moreover, not only the location of the targets in the media is important to obtain, but also the value of the associated dielectric constant is a critical parameter for the evaluation of the process. In this work, two novel imaging algorithms that are compatible with a low number of antennas and a limited-view arrangement of the antenna array are developed. Another technique is incorporated in the developed imaging algorithms to retrieve the dielectric constant of the detected targets in the interested media.

To form the real-time image reconstruction, at first, the Green's function of the stratified multilayered media is derived in the spectral domain. For the fast implementation of the imaging algorithm, a stationary phased approximation is applied to obtain a closed form for the Green's function of the multilayered media. A new microwave imaging algorithm called multistatic uniform diffraction tomography (MUDT) is developed to acquire the location of the targets in the multilayered media. Uniform diffraction tomography (UDT) is one technique that can provide real-time imaging. However, its single-input single-output data-based inverse scattering formulation leads to time-consuming data acquisition. Moreover, the performance of the UDT with a low number of antennas is not sufficient in most cases. Instead, the

MUDT imaging algorithm enables a real-time image from the inspected media with a low number of antennas and better spatial resolution.

In the high contrast case when the different dielectric constant of the two adjacent layers is high, many imaging algorithms fail to reconstruct truly the location of the targets in the multilayered media. It employs only the transmission part of the Green's function. Here, a Time Reversal Imaging (TRI) algorithm is employed and extended to obtain the position of the targets inside the high-contrast multilayered media. An exact or approximate Dyadic Green's Function (DGF) of the medium is required to apply the TRI. Therefore, an approximate expression of the DGF is constructed by incorporating both, the transmission and reflection parts of the multilayered media. Furthermore, a new Single-Frequency (SF)-TRI-DORT (decomposition of TR operator) is introduced based on the behavior of eigenvalues of the Time-Reversal operator (TRO) to foster high-speed data acquisition.

Quantitative microwave imaging methods deliver both the location and the dielectric constant of the localized objects. However, they should generally solve computationally time-consuming nonlinear inverse problems. Hence, they are not appropriate for real-time imaging. Here, by knowing the location of the targets, a fast optimization algorithm is derived by deriving the eigenvalues and eigenvectors of the scattering matrix to obtain the dielectric constant of the localized targets and by using a square error function.

A quantitative Bayesian inversion framework for Microwave Tomography (MWT) is coupled with MUDT method (i) to obtain the shape, (ii) to obtain the dielectric constant of the targets, and (iii) to improve the image quality of the targets. In essence, the information from the single-frequency Bayesian inversion framework is modified using high-resolution complementary structural information of the imaging domain from a qualitative approach MUDT utilizing broadband frequency-domain data. This way of obtaining structural prior information is effective as it utilizes the data from the same microwave sensor setup.

List of Publications in Frame of This Work

Journals

1. **A. Omrani**, R. Yadav, G. Link, and J. Jelonnek, "A Multistatic Uniform Diffraction Tomography Algorithm for Microwave Imaging in Multilayered Media for Microwave Drying," *in IEEE Transactions on Antennas and Propagation*, vol. 70, No. 10, pp. 9538-9595, May 2022.
2. **A. Omrani**, R. Yadav, G. Link, T. Lähivaara, M. Vauhkonen, and J. Jelonnek, "Multistatic Uniform Diffraction Tomography Derived Structural-Prior in Bayesian Inversion Framework for Microwave Tomography," *IEEE Transactions on Computational Imaging*, vol. 8, No. 10, pp. 986-995, Oct. 2022.
3. **A. Omrani**, R. Yadav, G. Link, T. Lähivaara, M. Vauhkonen, and J. Jelonnek, "An Electromagnetic Time-Reversal Imaging Algorithm for Moisture Detection in Polymer Foam in an Industrial Microwave Drying System," *Sensors*, vol. 21, No. 21, pp. 7409, Nov. 2021.
4. R. Yadav, **A. Omrani**, G. Link, M. Vauhkonen, and T. Lähivaara, "Correlated Sample based Prior in Bayesian Inversion Framework for Microwave Tomography," *in IEEE Transactions on Antennas and Propagation*, vol. 70, no. 7, pp. 5860-5872, July 2022.
5. R. Yadav, **A. Omrani**, G. Link, M. Vauhkonen, and T. Lähivaara, "Microwave Tomography Using Neural Networks for Its Application in an Industrial Microwave Drying System," *Sensors*, vol. 21, no. 20, pp. 6919, Oct. 2021.
6. Y. Zhang, **A. Omrani**, R. Yadav, and M. Field, "Supporting visualization analysis in industrial process tomography by using augmented

reality—a case study of an industrial microwave drying system," *Sensors*, vol. 21, no. 19, pp. 6515, Sep. 2021.

7. Y. Zhang, **A. Omrani**, R. Yadav, M. Field, and M Fratarcangeli, "Automated microwave tomography (Mwt) image segmentation: State-of-the-art implementation and evaluation," *Václav Skala-UNION Agency*, 2020.

Conferences

1. **A. Omrani**, G. Link, and J. Jelonnek, "A multistatic uniform diffraction tomographic algorithm for real-time moisture detection," *In Proceedings of the 2020 IEEE Asia-Pacific Microwave Conference (APMC)*, pp. 437-439, Dec. 2020.
2. **A. Omrani**, R. Yadav, G. Link, M. Vauhkonen, T. Lähivaara, and J. Jelonnek, "A combined microwave imaging algorithm for localization and moisture level estimation in multilayered media," 15th *European Conference on Antennas and Propagation (EuCAP)*, pp. 1-5, March 2021.
3. **A. Omrani**, R. Yadav, G. Link, and J. Jelonnek, "A time-reversal imaging algorithm for localization and moisture level detection in the polymer foam in an industrial microwave drying system," *AMPERE 2021 Proceedings.*
4. R. Yadav, **A. Omrani**, G. Link, M. Vauhkonen, and T. Lähivaara, "Microwave tomography for moisture level estimation using Bayesian framework," 15th *European Conference on Antennas and Propagation (EuCAP)*, pp. 1-5, March 2021.
5. R. Yadav, **A. Omrani**, G. Link, M. Vauhkonen, and T. Lähivaara, "Imaging porous materials with microwave sensor and learning- based reconstruction algorithm: Experimental study for industrial drying application," 10th *World Congress on Industrial Process Tomography (WCIPT 2021)*, Sep. 2021.
6. R. Yadav, **A. Omrani**, G. Link, M. Vauhkonen, and T. Lähivaara, "Complex-permittivity estimation of a polymer foam using microwave

tomography for the application of microwave drying," 18th *International Conference on Microwave and High Frequency Application (AMPERE 2021)*, Sep. 2021.

7. Y. Zhang, **A. Omrani**, R. Yadav, M. Field, and M Fratarcangeli, "Automatic image segmentation for microwave tomography (mwt) from implementation to comparative evaluation," *Proceedings of the* 12th *International Symposium on Visual Information Communication and Interaction*, pp. 1-2, Sep. 2019.
8. Y. Zhang, **A. Omrani**, R. Yadav, and M. Field, "A novel augmented reality system to support volumetric visualization in industrial process tomography," *Proceedings of the 2021 Conference on Interfaces and Human Computer Interaction*, pp. 3-9, July 2021.

Abbrevations and Variables

Abbreviations

CL	Characteristic lengths
DAQ	Data acquisition
DGF	Dyadic Green function
DORT	Decomposition of the TR operator
DT	Diffraction tomography
EM	Electromagnetic
EV	Eigenvalues
FEM	Finite element method
FT	Fourier transform
GPR	Ground-penetrating-radar
MMI	Millimeter-wave imaging
MDM	Multistatic data matrix
MIMO	Multiple-input-multiple-output
MUDT	Multistatic uniform diffraction tomography
MWT	Microwave tomography
NDT	Non-destructive testing
NRMSE	Normalized root means square error
PC	Processor

PML	Perfectly matched layer
RC	Resemblance coefficient
RMSE	Root mean square error
ROI	Region of interest
SAR	Synthetic aperture radar
SCR	Signal-to-clutter power ratio
SF	Spatial-frequency
SF-TR-MUSIC	Single-frequency time-reversal-multiple signal classification
SISO	Single-input-single-output
SNR	Signal-to-noise ratio
SP	Stationary point
SPA	Stationary phase approximation
SPR	Surface penetrating radar
SVD	Singular value decomposition
TE	Transverse electric
TR	Time-reversal
TRI	Time-reversal imaging
TRO	Time-reversal operator
TR-DORT	Time-reversal decomposition of the TR operator
TR-MUSIC	Time-reversal-multiple signal classification
TM	Transverse magnetic
TWRI	Through-the-wall-radar imaging

UDT	Uniform diffraction tomography
UWB	Ultra-wideband
VNA	Vector network analyzer

Constants

$c_0 = 299792458$	Speed of light	m/sec
$\varepsilon_0 = 8.854187817 \times 10^{-12}$	Vacuum permittivity	F/m
μ_0	Vacuum permeability	Hz
j	Imaginary unit	
π	Pi	

Lower Case Letters

d_a	distance between two adjacent antennas
$\boldsymbol{e}_p(\omega)$	new excitation for the transmitting antennas in TRI
$f(h)$	real and continuous and infinitely differentiable
fl_{max}	maximum fluctuations of the interfac
$\mathbf{g}_{br}$	Green's function vector
k_0	wavenumber in free space
k_{ls}	ls element of MDM matrix
k_n	wavenumber in layer n
k_y	wavenumber in y-direction
$k_{y,\mathrm{sp}}$	stationary point
k_{zn}	wavenumber in z-direction in layer n
$\vec{r} = (y, z)$	denotes point in the media
$\vec{r} = (y', z')$	denotes source point
$\vec{r}_{r_l}$	location of the l^{th} receiver antenna
$\vec{r}_{t_s}$	location of the s^{th} transmitter antenna
$\hat{r}$	unit vector in spherical coordinates

t_0	distance of the antenna to the first layer
t_q	thickness of each layer

Upper Case Letters

$\boldsymbol{D}$	image matrix constructed by time-reversal algorithm
$\vec{E}_n^{\mathrm{inc}}$	incident EM electric fields in layer n
$\vec{E}_n^{\mathrm{sct}}$	scattered EM electric fields in layer n
$\tilde{E}_n^{\mathrm{sct}}$	Fourier transform of scattered EM fields in layer n
$\vec{E}_n^{\mathrm{tot}}$	total EM electric fields in layer n
$\vec{\mathcal{E}}$	electric field in the time domain
$\bar{\bar{G}}_{\mathrm{e}}$	electric dyadic Green's function
G_{R}	reflection part of Green's function
G_{T}	transmission part of Green's function
$\bar{\bar{I}}$	idem factor
$I(\kappa)$	solution of integral with an oscillatory kernel
$\vec{J}(\vec{r})$	current source
$\vec{J}_{\mathrm{eq}}^{\mathrm{E}}(\vec{r})$	equivalent current density
$\boldsymbol{K}$	MDM matrix
$M\%$	moisture content
O	object function
R_n^{TM}	Fresnel reflection coefficient in layer n
RC_o	resemblance coefcient
SNR	signal-to-noise ratio
$S_{ls_{tot}}$	scattered fields with the target in the medium
$S_{ls_{free}}$	scattered fields without the target in the medium
T_n^{TM}	Fresnel transmission coefficient in layer n
$\boldsymbol{T}$	time-reversal operator
$\boldsymbol{U}$	left matrix consisting of normalized eigenvectors
$\boldsymbol{V}$	right matrix consisting of normalized eigenvectors
W_d	weight of the dry sample
W_m	weight of the foam sample after adding the water

Greek Symbols and Variables

$\varepsilon_{r,n}$	relative dielectric constant without irregularity
$\varepsilon_{r,n}(\vec{r})$	dielectric constant of the layer n with irregularity
ω	angular frequency
δ	Kronecker delta function
$\varkappa$	real, large and dimensionless parameter
ϕ	continuous function and infinitely differentiable
$\mathbf{\Sigma}$	real diagonal matrix consisting of eigenvalues

Contents

1 Introduction

Microwave imaging received much attention from various research groups in the last two or three decades. The significance of this subject is more due to the non-destructive nature and penetration of electromagnetic (EM) waves into different media or passing through them. Active and passive remote sensing in the microwave (300 MHz to 300 GHz) and millimeter-wave (30 GHz to 300 GHz) ranges, in addition to detection, has provided a remarkable capability for concealed-object imaging [1, 2]. Employed frequencies in microwave and millimeter-wave imaging (MMI) technologies are much lower than visible light. Consequently, MMI technologies provide adequate penetration into different media and materials for examination purposes [3].

It must be mentioned that X-rays can be used for imaging and remote sensing, especially in medical applications. In this case, the tissue is illuminated by the X-rays, and the reflected rays are recorded. The amount of absorption by the tissue is then measured by these rays. Considering that the absorption of healthy and cancerous tissues is not the same, their presence and absence, as well as their location, are detected. However, the problems caused by the destruction of living cells due to ionization are usually worrying and may cause cancer. In addition, employing X-rays technologies in industrial applications will be costly. Hence, their use has restrictions. Microwave and millimeter-wave radiation offer a non-ionizing alternative for imaging at moderate power levels, making them a safer and less costly option compared to X-rays. Microwave testing also does not require the same safety precautions as X-rays [4].

Since microwave and millimeter waves can penetrate smoke, fog, and dust better than optical and infrared systems, remote sensing in these frequencies in forest environments or rescue and fire fighting conditions are very remarkable. Moreover, the wideband measurement of data and acquiring both phase and magnitude is challenging at frequencies higher than microwave and millimeter-wave [5]. So, even in the situation that microwave and millimeter waves do not have a special superiority over other remote sensing methods, because the implementation of multi-sensor systems or systems with distributed sensors is associated with greater comfort, they play a significant role. Developing microwave technology demands various specializations in the electrical engineering area [6]. Particularly those related to signal, array, and image processing, as well as radars, antennas, and EM waves.

Different components are utilized to build a typical microwave imaging system, such as a microwave source, processor (PC), control, multiplexer, data acquisition (DAQ), switch, and transmit/receive antennas [5, 7–9]. Transmitting antennas are used to illuminate the inspected media, which includes the background media and any targets present within it. Fig. 1.1 illustrates a simplified schematic of the transmitter and receiver antennas, multi-layered medium, and the object inside it. Targets refer to objects in the media that have dielectric properties distinct enough to scatter electromagnetic fields. The scattered field collected by the receiving antenna consists of the scattered fields from any objects in the media and the background media. The acquired data is then processed to reconstruct 2D or 3D images of the inspected media.

The configuration of transmitting and receiving antennas in microwave imaging systems is commonly classified as monostatic, bistatic, or multistatic [10–12]. The monostatic case, also known as single-input-single-output (SISO) involves using a single antenna for both transmission and reception. In the bistatic scenario, one antenna is responsible for transmitting the EM waves into the media, and another antenna is responsible for receiving the scattered waves. Finally, in the multistatic scenarios, also known as multiple-input-multiple-output (MIMO), an array of the antenna is responsible for transmitting and receiving scattered EM waves. Additionally, DAQ can be achieved through stationary or non-stationary methods [13, 14]. Stationary DAQ involves an electronic switch to record scattered fields over a fixed antenna array, while non-stationary DAQ involves mechanical scanning to collect fields at different positions. Non-stationary DAQ may result in positioning errors. It is a time-consuming process and makes the

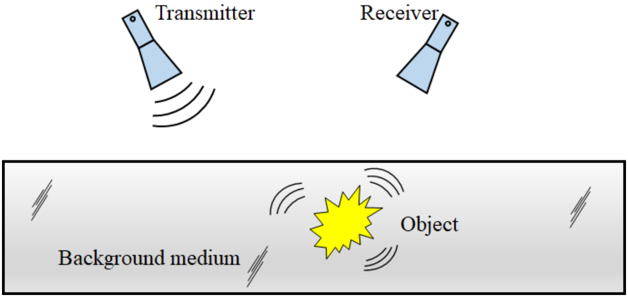

Fig. 1.1: A schematic of a bistatic microwave imaging setup. The transmitter antenna illuminates the background medium, and the object inside the background media scatters the EM field. Part of the scattered field receives by the receiver antenna for further process to locate the object.

measurement less repeatable. It may not be applicable in real-time applications.

Microwave imaging techniques have been vastly employed in the time domain and frequency domain based on data collection and reconstruction in the different applications [15–20]. In frequency domain techniques, measurements are performed at different frequencies using a frequency synthesizer. The analysis is performed in the frequency domain and frequency range, but for several discrete frequencies. The implementation of those methods is relatively simple and inexpensive due to the narrow-band nature of the techniques. It should be mentioned that the frequency domain techniques are used in the current work. In contrast, time-domain techniques employ narrowband Gaussian-like pulses separated by sufficiently long quiet intervals for wideband measurements. Unlike frequency domain methods, the analysis in the time domain utilizes a signal with a wide bandwidth. A wide bandwidth has a higher resolution limit due to high-frequency components and a greater penetration depth due to the presence of low-frequency components. A wideband antenna with a sufficiently large bandwidth is used to radiate these pulses. These techniques are more complicated to implement compared to the frequency domain techniques due to the large frequency bandwidth. Hence it will result in higher costs. However, the algorithms used in the time domain are much simpler to be derived than the algorithms in the frequency domain. But, the functional advantage of the frequency-domain techniques over the time-domain methods is the larger dynamic range. In time domain techniques, the signals are measured over a period of time. Any noise or interference present during this entire time can affect the measurements, reducing the dynamic range. In contrast, frequency-domain techniques often involve measurements at discrete frequencies, which can be analyzed independently and then combined. This allows for the exclusion of noise that is not consistent across all frequencies.

1.1 Applications of Microwave Imaging

During the last years, many microwave tomography (MWT) systems have been developed for different applications and purposes like medical imaging [21–23], subsurface imaging or ground-penetrating-radar (GPR) [24–26], through-the-wall-radar imaging (TWRI) [27–29], non-destructive testing (NDT) [30, 31], homeland security, etc. Here some growing applications for microwave imaging systems are listed.
For instance, using TWRI, behind as well as inside a wall, enclosed structure,

Fig. 1.2: (Left) A GPR system for mapping the location of the underground abandoned pipe, (right) a TWRI system that provides a clear position of people behind the wall.

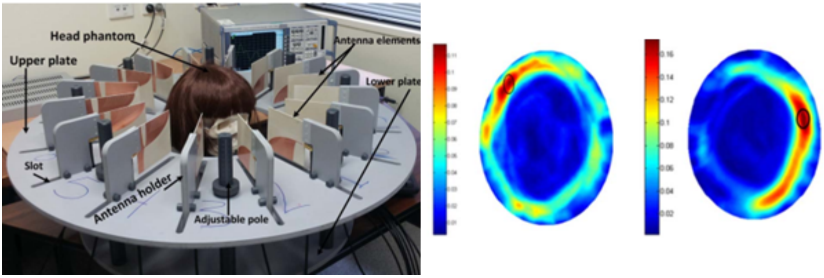

Fig. 1.3: (Left) Configuration of the whole microwave imaging system, (right) Imaging results with the locations of a hemorrhagic stroke. The exact locations of the strokes are indicated by black ellipses [40].

or man-made building materials, can be inspected, classified, and tracked for the hidden target(s), and persons, moving objects. This characteristic is favorably profitable for various organizations, including police, fire, and rescue, and defense forces [5, 32–35].

Ground penetrating radar (GPR), also known as surface penetrating radar (SPR), is another microwave imaging system for scanning beneath the ground for both civil and military programs. GPR can be used for monitoring underground pipes, environmental remediation, detecting landmines, archeology, and measuring the thickness of ice. Hence, it can be employed by civil and structural engineers, surveyors, or in environmental resources and archaeological applications [36–39].

Microwave imaging systems have a well-established application in synthetic aperture radar (SAR), which has been utilized for over 40 years in earth remote sensing. SAR provides high-resolution images that are independent of weather conditions and can be captured day or night, making it suitable for a range of applications such as geoscience, climate change research, environmental and earth system monitoring, 2D and 3D mapping, change detection, 4D mapping (space and time), security-related use, and planetary exploration [41–43]. The ability of microwaves to penetrate through farmland, herbage, and foliage enables the imaging system to detect hidden targets in forested environments. Additionally, remote sensing can be employed in agriculture applications, including identifying crop conditions, determining soil moisture content, and analyzing crop health.

It is worth mentioning that microwave imaging has been widely used in biomedical applications for breast cancer detection, osteoporosis detection, head imaging for tumor detection, etc [44–47]. In Fig. 1.3 (left) [40], a clinical prototype of a microwave imaging system for brain imaging is shown. The head phantom is surrounded by the transceiver Vivaldi antenna in order to achieve a wideband operation in the frequency range of 1 GHz-4 GHz in a monostatic configuration. In Fig. 1.3 (right), reconstructed images represent the position of the strokes marked with the black ellipse [40].

1.2 Emerging Application of Microwave Imaging and Challenges

Another new emerging application of the microwave imaging system is in industrial applications. Drying by microwaves has been widely used, especially in the industry, for different applications and purposes. This method provides volumetric heating and is more effective than conventional drying procedures. However, ensuring a uniform distribution of heat is crucial in industrial-scale production to avoid hot-spot formation and thermal runaway [48], which can decrease efficiency, compromise safety, and result in low-quality processing. In addition to these considerations, reducing drying time, energy consumption, and process intensification are also important factors for the industry.

It is well known that microwave heating is a non-linear process which means that an increase in the dielectric loss factor with increasing temperature as the drying process leads to a rapid rise in the rate of change of temperature causing a thermal runaway effect. This necessitates an intelligent control of the input power to prevent overheating. Thus, in most industrial heating systems temperature is used as the feedback parameter for online control [49]. Temperature output can be used to (i) switch the input power off at a set temperature, (ii) maintain the temperature at a set level for a specific period, or (iii) achieve a constant rate of heating. An excellent overview of the control strategies for the industrial microwave

Fig. 1.4: A side view of the HEPHAISTOS microwave oven system. The main modules of the oven are represented by number tags 1, 2, 3, 4, 5. Tag 1 and Tag 5 represent the entrance of the wet foam and exit doors for the dry foam on the conveyor belt, respectively. Tags 2, 3, and 4 indicate the three modular heating systems which inbuilt the hexagonal cavity with high-power microwave heating sources and control system block.

oven is provided in [50, 51]. In [52], an intelligent temperature control is demonstrated by controlling the power of distributed microwave power sources (magnetrons). However, for non-uniform moisture distributions in the samples, temperature controlled process alone is not sufficient as the electromagnetic (EM) heating might cause some parts of the samples to be over dried which might cause catastrophic overheating. For precise control of the distribution, in this case, [53], the control requires an in-situ and non-invasive measurement of the unknown distribution of moisture inside the samples.

1.3 Literature Review

There are two main categories of microwave imaging methods: quantitative and qualitative. Quantitative methods, also known as inverse scattering or optimization-based methods, aim to solve nonlinear inverse problems to retrieve information such as the shape, location, and properties of an object, respectively. Those problems are typically approximated by a linear inverse problem using the Born or Rytov approximations [54]. Direct inversion methods can be used to reconstruct the image. However, this approach can be time-consuming, particularly for large-scale imaging scenarios for which the computation time increases with the number of pixels in the image. As a result, quantitative methods may not be suitable for real-time processing. The main issue of these methods is the costly and time-consuming inverse operation process if dealing with large matrices of coefficients. Usually, in those cases, an iterative-based method is used for the inversion of the problem. Distorted born approximation [55], subspace-based optimization [56], and contrast source inversion [57] are some examples. In qualitative techniques, a reflective function (qualitative image) is illustrated to represent the desired object. Generally, those methods are not time-consuming and deliver the reconstruction image in real-time. However, the value of the constitutive parameters is not expected from those methods. To form an image by those methods, some simplifications are made. Synthetic aperture radar (SAR) [58, 59], time-reversal (TR) [60–64], and diffraction tomography (DT) [65–68] are some of the prevalent qualitative microwave imaging methods employed to reconstruct the image.

The fundamental difference between ultrasound and microwave tomography imaging on one side and X-ray imaging on the other side is that the latter travel on a straight path and are non-diffracted. Hence, it makes it possible to employ the Fourier slice theorem for inversion [69]. It implies employing inversion algorithms that assume straight ray traveling may lead to an inaccurate reconstruction of the media of interest [70]. The diffraction tomography algorithm, which is the generalization of the X-ray tomography, was introduced to reconsider the diffraction effect. Diffraction tomography is based on a simple relation between the spatial Fourier transform of the object function and the scattered field. Moreover, those algorithms reconstruct the quasi-real-time images under the conditions i) the object is a weak scatterer (Born approximation), and ii) the far-field assumption [71–75]. A DT algorithm for the geophysical survey was developed by Devaney [71] to generalize the medical diffraction tomography for geophysical applications. In this numerical study, the transmitter and receivers are deployed on opposite sides of the media, which might be not applicable to GPR applications.

In the GPR application, the effect of the planar air-soil interface was considered to cast the 3D diffraction tomography algorithm for detecting the pipelines under the ground [68]. The spectral representation of Green's function of the half-space in conjunction with the Born approximation was considered to estimate the object function. However, for the proper implementation, the pipelines should be located shallow enough, and the effect of the other layers of the ground was neglected, which is not realistic. In the work of [76], in addition to the planar soil interface, the loss of the soil was considered by applying the Tikhonov-regularized pseudo-inverse operator instead of the Fourier transform to obtain a more general object function, resulting in fewer artifacts if compared to [68].

In [65] a diffraction tomography (DT) was employed in the TWRI application to provide valuable information about the target extent in length, height, and width in real-time. The spectral representation of the dyadic Green's function of the layered media is used. As a result, a linear relationship between the received scattered field and the spectral representation of the object was obtained.

A uniform diffraction tomography (UDT) algorithm was proposed in [77] that correctly applies the stationary phase approximation to improve the estimate in comparison to the DT for embedded targets in a multilayered media. The reconstruction provided by the UDT is in real-time. It uses a monostatic antenna configuration and the algorithm incorporates only the reflected field. For its suitable implementation in the fixed array case, the following guidelines have to be taken into account: i) desired antenna type and specifications to achieve a good spatial resolution, ii) a large number of antennas or measurement points should be considered, and iii) the antennas should be positioned in close vicinity to meet the Nyquist sampling rate

criteria. It should be mentioned, that the uniform diffraction tomography algorithm utilizes the Fourier transform of the scattered field at the antenna locations. To ensure accurate target localization and prevent aliasing, it's essential to maintain a minimum distance between the antennas. Consequently, this necessitates the use of a substantial number of antennas within a fixed aperture. But, considering real-time monitoring in the industrial application, the given guidelines have to be compromised. The use of a large number of antennas increases the DAQ time and overall system cost.
A TR UDT was proposed for the TWRI application to address specifically the localization of the weak targets behind the wall [78, 79]. A pole extraction algorithm was performed to extract the wall information, including thickness, the dielectric constant of the wall layers, and the conductivity. Then by removing the reflected fields from the wall, a singular value decomposition was applied to the scattering matrix. A new set of excitations for the UDT algorithm was generated. This new set of excitation provides selective focusing and also detects weak scatterers. However, to implement the imaging algorithm, all scattering data is required, which makes DAQ time-consuming.

TR imaging is another method to reconstruct the location of a target in different media and under various conditions. This method was first demonstrated in 1989 by Fink et al. using ultrasound signals. It was inspired by the conjugate phase method in optics. The most significant difference between the method presented and the conjugate phase method in optics is that instead of the operation in the frequency domain, Fink et al. performed its equivalent in the time domain. Consequently, instead of a single frequency, a conjugation operation was applied in the entire frequency band. To experimentally investigate the TR technique, Fink et al. sent a signal to the region of interest. The reflected signal was recorded using the transducers surrounding the media. The received signal was time reversed and used as a new excitation for the transducers. Later, Fink et al. retransmitted this new excitation (time-reversed signal) to the region of interest (ROI), and it was observed that the newly sent signals focused on the target. It indicates that the converged time-reversed signals travel the same path as the diverged signal travels from the inhomogeneity [60, 80, 81]. The super-resolution property, i.e., the ability to resolve scatterers beyond the classical diffraction limit, of the TRI helps to better focus on and detect a target embedded in a background medium [82, 83]. This property comes from the utilization of the multipath in strong clutter condition. TRI is mainly divided into experimental and computational categories where experimental TRI's major advantage over computational TRI is that the former does not require the dyadic Green function (DGF) of the medium containing the scatterers. In computational TRI, however, the images of the target are synthetically generated. Indeed computational TRI needs an exact or approximate knowledge of the DGF of the total medium (e.g. the background medium with the presence of the scattering target). Computational TRI is based on the decomposition of the TR operator (TRO). The method of decomposition of the TR operator (DORT) uses the signal subspace of the decomposition while the method of multiple signal classification uses the null subspace of the decomposition. The null space in time-reversal imaging helps to identify areas or configurations within the medium that do not contribute significantly to the recorded scattered fields.

TR imaging has been applied in numerous practical applications of ultrasound [84, 85] and EMs. It is also used in medical applications like diagnosis and treatment of breast cancer [86], and to keep track of kidney stones for lithotripsy process [87]. Further, this method is employed in non-destructive testing, such as the detection of the defects in pipelines [61] and solids [88], and retrieving the dielectric constant of a hidden dielectric target in a cylindrical multilayered structure [64]. The high-resolution characteristic of TR facilitates the detection of the targets even under strong clutter conditions [62, 63, 89]. In [62], ultra-wideband TR imaging is used to detect the target location in the free space continuous random media. A TR-DORT method was used to achieve selective focusing to distinguish different targets from each other. It was shown that under continuous random media, the multiple scattering effect increases, which increases the effective aperture of the TRI. In [63], the performance of the TR-DORT and time reversal-multiple signal classification (TR-MUSIC) were investigated under non-ideal conditions. The multistatic data matrix (MDM) was collected in the spatial-frequency domain (SF). In media with strong multiple scattering or clutter, unlike the

time domain (TD)-DORT, the SF-DORT can provide a coherent MDM for TR imaging (TRI).
A TR-DORT and TR-MUSIC methods were used to identify the moving targets in a free space media [83]. The steps were as follows: i) at first, an average MDM matrix was constructed by performing several measurements, ii) this average MDM corresponds to the stationary targets present in the media, iii) Next, by subtracting the constructed MDM from the new measurement and average MDM, those MDM corresponding to the moving targets can be produced, and utilized for the moving target detection. In [90], TRI was used in the GPR application to discover the location of the dielectric and metallic targets under the Gaussian rough surface. It was shown by increasing the distance of the antenna from the top of the rough surface, the signal-to-clutter power ratio (SCR) significantly increases, which enhances the TRI detectability of buried targets on a strong rough surface. Moreover, in order to reduce the rough surface scattering effect, time-gating was used. Furthermore, a single-frequency TR-MUSIC (SF-TR-MUSIC) was proposed for image reconstruction. In [91], Green's function of the air-soil interface with the rough surface, was estimated using the transmitted electric field. The reflected field was not considered. In [77–79, 90–93], only the transmission part of Green's function was considered to locate the target in the multilayered media. However, it is not sufficient to take into account the presence of a metal plate or high-contrast layered media. Therefore, it is required to construct an expression of the DGF by incorporating both the transmission and reflection parts of the multilayered media. Here, it should be noted that in diffraction tomography-based algorithms, e.g., UDT [77], MUDT [93], incorporating the reflected part will render the integral undefined as closed-form of the object function cannot be evaluated by applying stationary phase approximation (SPA).

1.4 Objective and Content

This dissertation introduces two microwave imaging algorithms for the detection of multilayered media, along with two distinct approaches for determining the dielectric constant of targets within those media. Firstly, a closed form for Green's function of the multilayered media is obtained using the stationary phase approximation. In this case, the integral, which involves an integrand exhibiting rapid oscillations, is simplified by concentrating on the contributions from stationary points (points where the derivative of the phase of the integrand is zero) while neglecting other oscillatory terms.

Secondly, a multistatic uniform diffraction tomography algorithm (MUDT) is proposed, which is specifically designed for the measurement case of a MIMO fixed array sensor configuration. The MUDT algorithm utilizes a reduced number of antennas compared to current diffraction tomography-based algorithms and produces superior reconstructed images by utilizing the non-diagonal element of the scattering matrix. Additionally, the performance of the proposed algorithm is evaluated under non-ideal conditions, such as random rough interfaces of the dielectric layer and random dielectric constant distribution in the background media.

To address the microwave imaging of high-contrast layered media for which the dielectric constants of adjacent layers differ significantly, TRI is proposed by incorporating both, the transmission and reflection parts of the multilayered media. Additionally, a new single-frequency (SF)-TRI-DORT method is introduced, exploiting the behavior of eigenvalues of the TRO to enhance high-speed data acquisition (DAQ). The performance of both the TRI and SF-TRI algorithms is evaluated using numerical data, particularly focusing on scenarios without metal-plate backing conditions.

Additionally, a singular value decomposition (SVD)-based approach is used to determine the dielectric constant of targets within multilayered media without the need to use the time-consuming quantitative method. Furthermore, a coupled microwave imaging algorithm combining MUDT or TRI with a quantitative Bayesian inversion framework is developed to determine the location and dielectric constants of targets, with MUDT providing prior information to the Bayesian inversion framework.

This thesis is organized as follows: Chapter 2 describes the EM scattering equation between the received scattered field and the object function. A closed-form expression using stationary phase approximation is obtained. The MUDT and TRI are formulated. Chapter 3 presents the simulation and experimental results of MUDT and TRI for different scenarios and conditions. In Chapter 4, the SVD-based approach and coupled method for retrieving the dielectric constant of the detected targets are presented. Finally, Chapter 6 discusses the results and provides a final conclusion.

2 Multistatic Uniform Diffraction Tomography and Time-Reversal Imaging Formulation

The objective of the study is to determine the distribution and values of dielectric constants of irregularities within a media, which is described as stratified media. To achieve this goal, the inverse problem is solved. This problem is addressed using different microwave imaging algorithms and MWT sensors.

There are two main categories of sensors: passive and active. Passive sensors include different types of radiometers and spectrometers, which are commonly used in remote sensing applications in the visible, infrared, thermal infrared, and microwave portions of the EM spectrum. On the other hand, active sensors transmit a signal into the environment and then measure the scattered response. Examples of some active sensor-based technologies include scanning electron microscopes, LiDAR, radar, GPS, x-ray, sonar, infrared, and seismic.

Sensor configurations can be mono-static, bi-static, or multistatic, with different considerations for the forward model. In previous work, the monostatic configuration was used for data collection, where one antenna transmits the signal and the other antenna (or the same antenna) receives the scattered field from the media under investigation. However, this scenario requires mechanical scanning to scan the aperture length, since two antennas are used for receiving the scattered fields, which might not be applicable when real-time data collection is required.

In this chapter, multistatic microwave imaging through multilayered media is investigated. The array of antennas is positioned linearly and transmits/receives EM waves. In numerous applications such as GPR and TWRI, accessing both sides of the medium is often impractical. Therefore, it is crucial to develop algorithms that can effectively operate when linearly positioned on only one side. Even in industrial scenarios where access to the other side of the product is possible, challenges arise due to the presence of conveyor belts, making it challenging to install an antenna array on the opposite side. Consequently, positioning the antenna array on a single side is the preferred approach. Moreover, in this configuration, a reduced number of antennas is typically utilized in comparison to dual-sided positioning.

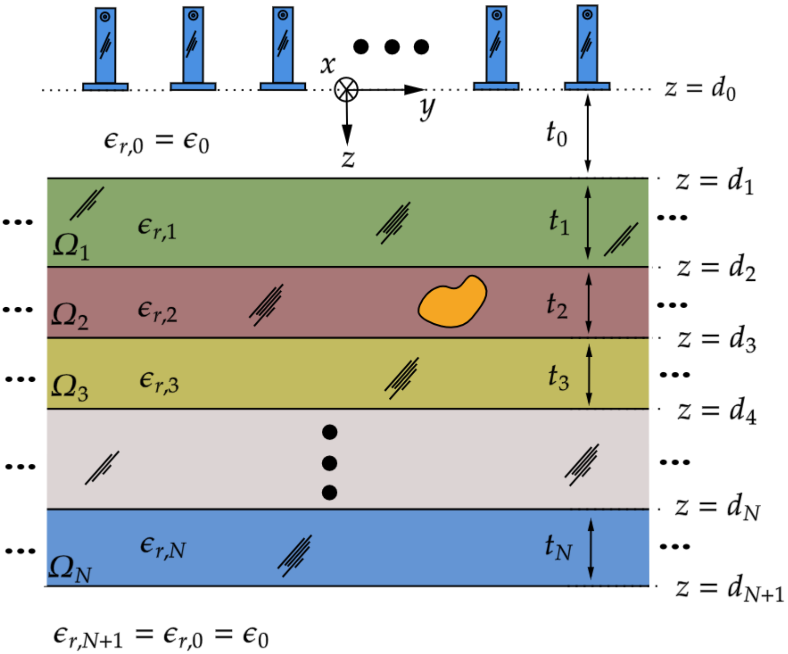

Fig. 2.1: Generalized geometry of the multilayered media with N layers. The inhomogeneities can be located anywhere inside the multilayered media.

2.1 Introduction

To acquire the microwave image, a relation between the scattered field at the position of the antenna array and the objects positioned in layer n must be obtained.

The generalized configuration of the multistatic imaging system for the layered media is represented in Fig. 2.1. The multistatic array resides in semi-infinite free space above the media. Generally, in practical scenarios like TWRI, or GPR, the antenna array cannot be positioned on both sides of the media. It can make the problem more severe since the transmitting waves shall propagate twice through the media when the transmitter/receiver array is co-located. In the following, the formulation of the inverse problem is represented in the frequency domain. The measurements are performed at different frequencies using a synthesizer. Each measured data point (scattered field) is represented by a complex number characterized by its magnitude and phase terms.

The distance of the antenna to the first layer is defined as t_0, and the thickness of each layer is $t_q = d_{q+1} - d_q$ where $q = 1, 2, \cdots N$, and the center to center distance between two adjacent antennas is d_a. The free space is represented as layers 0 and $N+1$. In free space, the relative dielectric constant is denoted as $\varepsilon_{r,0} = \varepsilon_{r,N+1} = 1$ whereas the relative dielectric constant of the layer n (background without irregularities) is set to $\varepsilon_{r,n}$, and dielectric constant of the layer n with irregularity is set to $\varepsilon_{r,n}(\vec{r})$. The background media is the medium without any scatterer. The dielectric constant (of the background media) varies only in the z-direction, and diffractions from the corners are neglected.

To obtain a relation between the received scattered field and the object(s) in the n^{th} layer, the *inhomogeneous vector wave equations* in layer n for the incident and total electric field is formulated as follows

$$\nabla \times \nabla \times \vec{E}_n^{\text{inc}}(\vec{r}) - k_0^2 \varepsilon_{r,n} \vec{E}_n^{\text{inc}}(\vec{r}) = -j\omega\mu_0 \vec{J}(\vec{r}) \tag{2.1}$$

$$\nabla \times \nabla \times \vec{E}_n^{\text{tot}}(\vec{r}) - k_0^2 \varepsilon_{r,n}(\vec{r}) \vec{E}_n^{\text{tot}}(\vec{r}) = -j\omega\mu_0 \vec{J}(\vec{r}) \tag{2.2}$$

where $\vec{E}_n^{\mathrm{tot}}$ and $\vec{E}_n^{\mathrm{inc}}$ are the total and the incident EM electric fields in layer n, respectively. $\vec{J}(\vec{r})$ is the current source or antenna, exciting the media. $\vec{r} = (y, z)$ denotes point in the media, and k_0 represents the wavenumber in free-space. $\varepsilon_{r,n}$ is the dielectric constant of the background in layer n. All through the equations, $e^{-j\omega t}$ harmonic time-convention is assumed. ω is the angular frequency, and μ_0 is the permeability constant in the dielectric media.

By adding $\pm k_0^2 \varepsilon_{r,n} \vec{E}_n^{\mathrm{tot}}(\vec{r})$ to the left-hand side of Equation (2.2), and then subtracting the Equation (2.2) from the Equation (2.1), an inhomogeneous vector wave equation for the scattered field generated by the object is derived

$$\nabla \times \nabla \times \vec{E}_n^{\mathrm{sct}}(\vec{r}) - k_0^2 \varepsilon_{r,n}(\vec{r}) \vec{E}_n^{\mathrm{sct}}(\vec{r}) = -k_0^2 \Big(\varepsilon_{r,n}(\vec{r}) - \varepsilon_{r,n} \Big) \vec{E}_n^{\mathrm{tot}}(\vec{r}) \tag{2.3}$$

where the scattered electric field is the subtraction of the total electric field from the incident one, represented as follows

$$\vec{E}^{\mathrm{sct}} = \vec{E}^{\mathrm{tot}} - \vec{E}^{\mathrm{inc}}. \tag{2.4}$$

In (2.3), the right-hand side can be shown as an equivalent current density as follows

$$\vec{J}_{\mathrm{eq}}^{\mathrm{E}}(\vec{r}) = -j\omega \Delta\varepsilon(\vec{r}) \vec{E}_n^{\mathrm{tot}} \tag{2.5}$$

where $\Delta\varepsilon(\vec{r}) = \varepsilon_{r,n}(\vec{r}) - \varepsilon_{r,n}$ is the difference between the dielectric constant of the layer n and the dielectric constant of the background media in layer n. From the Equation of (2.5), it can be perceived that the scatterer is replaced by an equivalent induced current source in the layer n, that generates the scattered electric field. It is interpreted as the *volumetric current model* [94].

To find the solution for the Equation (2.3), the dyadic Green's technique is employed. The electric dyadic Green's function is the response to the three infinitesimal electric dipoles (point source) located at $\vec{r} = \vec{r}'$ with the triple orthogonal orientation (for example $\hat{x}, \hat{y}, \hat{z}$ in the Cartesian coordinate) that satisfies the following equation [95]

$$\nabla \times \nabla \times \bar{\bar{G}}_{\mathrm{e}}(\vec{r}, \vec{r}') - k^2 \bar{\bar{G}}_{\mathrm{e}}(\vec{r}, \vec{r}') = \bar{\bar{I}} \delta(\vec{r} - \vec{r}') \tag{2.6}$$

where $\bar{\bar{G}}_e$ is defined as the electric dyadic Green's function [95], $\bar{\bar{I}}$ is a idem factor [95], and δ is the Kronecker delta function. The wave equations for the electric DGF are to be used to integrate the eq. (2.3) are

$$\nabla \times \nabla \times \bar{\bar{G}}_{\mathrm{e}}^{(0n)}(\vec{r}, \vec{r}') - k_0^2 \bar{\bar{G}}_{\mathrm{e}}^{(0n)}(\vec{r}, \vec{r}') = 0 \tag{2.7}$$

$$\nabla \times \nabla \times \bar{\bar{G}}_{\mathrm{e}}^{(nn)}(\vec{r}, \vec{r}') - k_n^2 \bar{\bar{G}}_{\mathrm{e}}^{(nn)}(\vec{r}, \vec{r}') = \bar{\bar{I}} \delta(\vec{r} - \vec{r}'). \tag{2.8}$$

Subscribe in $\bar{\bar{G}}_{\mathrm{e}}^{(nn)}$ denotes both source and observation points are located in layer n, and superscript in $\bar{\bar{G}}_{\mathrm{e}}^{(0n)}$ means the observation point is located in layer 0, and source point is positioned in layer n. Using the second vector Green's theorem [95] as shown below

$$\iiint_{\Omega} \left[\vec{P}.\nabla\times\nabla\times\bar{\bar{Q}} - (\nabla\times\nabla\times\vec{P}).\bar{\bar{Q}}\right] d\Omega = -\oiint_{\partial\Omega} \hat{n}.\left[\vec{P}\times\nabla\times\bar{\bar{Q}} + (\nabla\times\vec{P})\times\bar{\bar{Q}}\right] dS, \tag{2.9}$$

where $\partial\Omega$ is the boundary surface surrounded the region Ω. By letting $\vec{P} = \vec{E}_0(\vec{r})$ and $\bar{\bar{G}} = \bar{\bar{G}}_{\mathrm{e}}^{(nn)}(\vec{r}, \vec{r}')$, it follows

$$\vec{E}_0^{\mathrm{sct}}(\vec{r}) = j\omega\mu_0 \iiint_{\Omega_n} \bar{\bar{G}}_{\mathrm{e}}^{(0n)}(\vec{r}, \vec{r}') \cdot \vec{J}_{\mathrm{eq}}^{\mathrm{E}}(\vec{r}) dr' \tag{2.10}$$

where the range of integration is all volume of the region Ω_n. Note that in Eq. (2.10), the *Sommerfeld radiation condition* [96] is employed. This condition indicates that the far-zone EM field due to any current distribution satisfies the condition

$$\lim_{r\to\infty} \left[\nabla \times \begin{pmatrix} \vec{E} \\ \vec{H} \end{pmatrix} - jk_0 \hat{r} \times \begin{pmatrix} \vec{E} \\ \vec{H} \end{pmatrix}\right] = 0, \tag{2.11}$$

where $\hat{r}$ is the unit vector in spherical coordinates. Since $\Delta\varepsilon(\vec{r}) = \varepsilon_{r,n}(\vec{r}) - \varepsilon_{r,n}$, $\vec{J}_{\mathrm{eq}}^{\mathrm{E}} = -j\omega\Delta\varepsilon\vec{E}_n^{\mathrm{tot}}$, it can be written from Eq. 2.10

$$\vec{E}_0^{\mathrm{sct}}(\vec{r}) = -j\omega\mu_0 \iiint_{\Omega_n} \left[\bar{\bar{G}}^{(n0)}(\vec{r}', \vec{r})\right]^T \cdot \left[j\omega(\varepsilon(\vec{r}) - \varepsilon_{r,n})\right] \vec{E}_n^{\mathrm{tot}}(\vec{r}', \Delta\varepsilon(r')) d\vec{r}' \tag{2.12}$$

The above expression is the well-known Lippmann-Schwinger integral equation [97] of the EM scattering problem and relates the scattered electric field at the position of the antenna array to the target in the Region Of Interest (ROI). This integral equation is intrinsically non-linear because the total internal electric field is an implicit function of the unknown dielectric coefficients.

To obtain the characteristics of the targets, an inverse integral equation must be derived. Depending on the scenario and application, the above integral equation can be solved differently. In the above equation, as noted earlier, $\bar{\bar{G}}_{\mathrm{e}}^{(n0)}(\vec{r},\vec{r}')$ is the Green's function of the media,. In this work, it is a stratified multilayered media. The Green's function only depends on the observation point, the source point, but not the type of antenna. Before addressing the above integral equation to exploit the characteristics of the target, the integral representation of the Green's function of the stratified multilayered media in the spectral-frequency domain is obtained. Next, for fast implementation of the imaging algorithm, using the stationary phase approximation method, a simplified expression of the Green's function will be derived.

2.2 Green's Function of the Multilayered Media

2.2.1 Spectral Representation of Green's Function

Here the multilayered media shown in Fig. 2.1 with the planar interfaces parallel to the xy plane of the Cartesian coordinate system is considered. Without loss of generality, it is assumed that the multilayered media does not have any variation concerning the x position. Moreover, the EM field in the source-free region can be expressed as the sum of a transverse magnetic (TM) field and a transverse electric (TE) field [98, 99]. For TM waves all fields can be expressed in terms of the x-component of the electric field $\vec{E}$ and for TE waves the electric field can be expressed in terms of the x-component of the magnetic field $\vec{H}$. Here, it is assumed that the equivalent currents in the media and antenna locations are located at the top of the multilayered media and predominant by x-polarized (both transmitting and receiving antennas are x-polarized), so only one term (xx) of the dyadic Green's function (DGF) is employed. That implies the Eq. (2.12) reduces to a scalar form.

The spectral representation of the Green's function in the source layer (the layer where the scatterer is located) is given by [94, 100]

$$\bar{\bar{G}}_{\mathrm{e}}^{(00)}(\vec{r}_r,\vec{r}_t) = \frac{1}{\pi}\int_{-\infty}^{+\infty}\frac{1}{k_{z0}}\Big[e^{-jk_{z0}|z-d_0|} + R_0^{TM}(k_y)e^{+jk_{z0}|z-d_0|}\Big]\cdot e^{-jk_y(y-y_t)}dk_y \tag{2.13}$$

where k_{z0} is the wavenumber in z-direction in layer 0, k_{zn} is the wavenumber in z-direction in layer n, and k_y denotes the wavenumber in y-direction. $\vec{r}_t = (y_t, z_t = d_0)$ is the source point. $R_0^{\mathrm{TM}}(k_y)$ is the Fresnel reflection coefficient in layer 0. The first and second terms in the kernel of the integral represent the transmission and reflection terms, respectively. The spectral representation of the Green's function in layer n, where $z > d_0$ is as follows

$$G_{\mathrm{e}}^{(n0)}(\vec{r},\vec{r}_t) = \frac{1}{\pi}\int_{-\infty}^{+\infty}\frac{1}{k_{z0}}\Big[T_n^{TM}(k_y)e^{-jk_{zn}(z-d_0)} + R_n^{TM}(k_y)e^{+jk_{zn}(z-d_0)}\Big]\cdot\ e^{-jk_y(y-y_t)}dk_y. \tag{2.14}$$

where k_y is the wavenumber in y-direction. Subscribes in $G_{\mathrm{e}}^{(n0)}$ denotes the observation point is located in layer n and the source point is located in layer 0. The dispersion relation in the layer n is expressed by

$$k_{zn} = \sqrt{k_n^2 - k_y^2} \tag{2.15}$$

and $k_n = k_0\sqrt{\varepsilon_n}$ is the wavenumber in layer n while k_0 is the free-space wavenumber. $T_n^{\mathrm{TM}}(k_y)$ and $R_n^{\mathrm{TM}}(k_y)$ are the Fresnel transmission and reflection coefficients in layer n respectively and can be obtained by applying the boundary conditions between layers.

From the above expression, it is clear that Green's function is constructed from different plane waves. In other words, Green's function is a summation of the plane waves, with different weighted coefficients. To obtain transmission and reflection coefficients of Green's function, the boundary conditions for one arbitrary plane wave at the different layers are applied, and then these coefficients are calculated [101]. As long as the integral is a linear operator, by applying integration to the coefficients with the various spectral weights, Green's function, can be achieved. The detail of the derivation of the coefficients is provided in the Appendix section.

Once the reflection/transmission coefficients of a layer are determined, it is possible to construct the behavior of the EM field within that layer. Using Equation (2.14) and substituting the reflection and transmission coefficients of layer n, the spectral representation of Green's function can be obtained. It is important to note that only the first-order reflection and transmission coefficients within each layer are taken into account. It's worth emphasizing that when referring to 'first-order reflection', the specific emphasis is on the reflection of a wave within the dielectric layer while disregarding any additional reflections occurring within that same layer. An expression for the Green's function with the source point located in the 0^{th} layer and the observation point in the n^{th} layer can be derived as follows

$$
\begin{aligned}
&G_{\mathrm{e}}^{(n0)}(\vec{r}_r,\vec{r}_t)\\
&=\frac{1}{\pi}\int_{-\infty}^{+\infty}\frac{1}{k_{z0}}\times\Bigg[\prod_{q=0}^{n-1}T_{q(q+1)}^{\mathrm{TM}}e^{-j\left[k_{zn}(z-d_0-\sum\limits_{q=0}^{n-1}\Delta d_q)+\sum\limits_{q=0}^{n-1}k_{zq}\Delta d_q\right]}\\
&+\prod_{q=0}^{n-1}R_{q(q+1)}^{\mathrm{TM}}T_{q(q+1)}^{\mathrm{TM}}e^{+j\left[k_{zn}(z-d_0-\sum\limits_{q=0}^{n-1}\Delta d_q)+\sum\limits_{q=0}^{n-1}k_{zq}\Delta d_q\right]}\Bigg]e^{-jk_y(y-y_t)}dk_y.
\end{aligned}
\tag{2.16}
$$

where $\vec{r}_r=(y_r,z_r)$ is the receiver point. $T_{n(n+1)}^{\mathrm{TM}}$ is the Fresnel transmission coefficient for interface between layers n and $n+1$ and is given by [94]

$$
T_{n(n+1)}^{\mathrm{TM}}=\frac{2k_{zn}}{k_{zn}+k_{z(n+1)}}. \tag{2.17}
$$

2.2.2 Stationary phase approximation

In this part, a new closed-form representation for the Green's function of the multilayered media will be derived. The Green's function in the above equation is composed of two parts, and it can be written as a summation of the transmission and reflection terms, i.e., $G_{\mathrm{e}}^{(n0)} = G_{\mathrm{T}}^{(n0)} + G_{\mathrm{R}}^{(n0)}$, where the subscribe T in $G_T^{(n0)}$ denotes the transmission part and the subscribe R in $G_R^{(n0)}$ denotes the reflection part. In the following, each part is addressed individually and a closed form for Green's function of the multilayer media is obtained by employing the stationary phase approximation (SPA) method. The stationary phase approximation estimates a solution for the integral with an oscillatory kernel [102] as follows [103]

$$I(\varkappa) = \int_{-\infty}^{+\infty} f(h) e^{j\varkappa\phi(h)} dh$$

$$\approx \left[\frac{2\pi}{\varkappa\left|\phi''(h_0)\right|}\right]^{\frac{1}{2}} f(h_0) e^{j\left[\varkappa\phi(h_0) - \frac{\beta}{2} + \frac{\pi}{4}\right]}, \quad (2.18)$$

$$\phi''(h_0) = \left[\phi''(h_0)\right] e^{j\beta} \qquad \phi'(h_0) = 0, \quad (2.19)$$

$\varkappa$ is real large and dimensionless. f and ϕ are real and continuous functions and infinitely differentiable, so that an infinite asymptotic expansion can be obtained via the integration-by-parts method [102]. Also, h_0 is the point where $\phi' = \frac{d\phi}{dh} = 0$ so called a stationary point (SP). Later to separate the stationary point for the transmission and the reflection parts, one will be represented as sp_1, and the other one will be represented as sp_2, respectively.

So, the first term of (2.16) is derived using the SPA and reduced to a simple summation given as

$$G_{\mathrm{T}}^{(n0)} = \frac{1}{\pi}\left(\prod_{q=0}^{n-1} T_{q(q+1)}^{\mathrm{TM}}(k_{y,\mathrm{sp}_1})\right)\left[\frac{2\pi}{|\Phi_T''(k_{y,\mathrm{sp}_1})|}\right]^{\frac{1}{2}} e^{-j\left[k_{y,\mathrm{sp}_1}(y-y_t)+\tilde{k}_{zn}(z-d_0-\sum_{q=0}^{n-1}\Delta d_q)+\sum_{q=0}^{n-1}\tilde{k}_{zq}\Delta d_q\right]} e^{-j\left(\frac{\beta}{2}-\frac{\pi}{4}\right)} \tag{2.20}$$

where

$$\Phi_{\mathrm{T}}''(k_{y,\mathrm{sp}_1}) = -\frac{k_n^2}{k_{zn}^3}\left(z-d_0-\sum_{q=0}^{n-1}\Delta d_q\right)+\sum_{q=0}^{n-1}\frac{k_q^2}{k_{zq}^3}\Delta d_q \tag{2.21}$$

$$\Phi_T''(k_{y,\mathrm{sp}_1}) = \left|\Phi_T''(k_{y,\mathrm{sp}_1})\right| e^{-j\beta}, \tag{2.22}$$

where k_{y,sp_1} is the stationary point and is the solution of the following equation

$$k_{y,\mathrm{sp}_1} = \frac{y-y_t}{\sum_{q=0}^{n-1}\frac{\Delta d_q}{k_{zq}}+\frac{1}{k_{zn}}\left(z-d_0-\sum_{q=0}^{n-1}\Delta d_q\right)} \tag{2.23}$$

$$\tilde{k}_{zn} = \sqrt{k_n^2-k_{y,\mathrm{sp}_1}^2} \tag{2.24}$$

Analogous to the transmission term, a closed form for the reflection term can be derived leading to

$$G_{\mathrm{R}}^{(n0)} = \frac{1}{\pi}\left(\prod_{q=0}^{n-1} T_{q(q+1)}^{\mathrm{TM}}(k_{y,\mathrm{sp}_2})R_{q(q+1)}^{\mathrm{TM}}(k_{y,\mathrm{sp}_2})\right)\left[\frac{2\pi}{|\Phi_T''(k_{y,\mathrm{sp}_2})|}\right]^{\frac{1}{2}} .e^{-j\left[k_{y,\mathrm{sp}_2}(y-y_t)+\tilde{k}_{zn}(z-d_0-\sum_{q=0}^{n-1}\Delta d_q)-\sum_{q=0}^{n-1}\tilde{k}_{zq}\Delta d_q\right]} e^{-j\left(\frac{\beta}{2}-\frac{\pi}{4}\right)} \tag{2.25}$$

where

$$\Phi''_{\mathrm{R}}(k_{y,\mathrm{sp}_2}) = -\frac{k_n^2}{k_{zn}^3}\left(z - d_0 - \sum_{q=0}^{n-1} \Delta d_q\right) - \sum_{q=0}^{n-1} \frac{k_q^2}{k_{zq}^3} \Delta d_q \tag{2.26}$$

where k_{y,sp_2} is the stationary point and is the solution of the following equation

$$k_{y,\mathrm{sp}_2} = \frac{y - y_t}{\sum_{q=0}^{n} \frac{\Delta d_q}{k_{zq}} - \frac{1}{k_{zn}}\left(z - d_0 - \sum_{q=0}^{n-1} \Delta d_q\right)} \tag{2.27}$$

Equations (2.20) and (2.25) represent the closed forms of the transmission and the reflection part of Green's function of the multilayered media. This representation will be used later in TRI algorithm, and to determine the dielectric constant of the target in the mutilayered media.

2.3 Multistatic Uniform Diffraction Tomography

As mentioned earlier, a uniform diffraction tomography (UDT) algorithm was proposed in [78, 104] to achieve improved estimates in comparison to diffraction tomography for embedded targets in a multilayered media. The reconstruction provided by the UDT is in real-time with monostatic antenna configuration and the algorithm incorporates only reflection data. For its suitable implementation in the fixed array case, the following guidelines should be taken into account: i) desired antenna type and specifications to achieve good spatial resolution, ii) to cover a large imaging domain, a high number of antennas or measurement points should be employed, and iii) the antennas should be positioned in close vicinity to meet the Nyquist sampling rate criteria. But, considering real-time monitoring in the industrial application, given guidelines are compromised. The use of a large number of antennas increases the DAQ time and overall system cost. Thus, an obvious choice would be to use a fixed array, i.e. a multistatic MWT system with a low number of antennas. However, with the use of a limited number of antennas, the aliasing effect is seen in the reconstructed image, and spatial resolution is affected when multiple scatterers in the multilayered media are present. The former is caused due to the Nyquist criteria not being met. While, the latter are: first, less spectral components of scattered fields are present at the antennas aperture, second, in multiple scatterers case, the different spectral components from respective scatterers cannot be distinguished [105–107]. As mentioned earlier, an inverse scattering problem has to be solved to extract the location and characteristics of the target in the ROI. In this work, a multistatic uniform diffraction tomography algorithm (MUDT) for multilayered media is proposed [93]. The MUDT algorithm developed here specially caters to the measurement case of a multiple-input multiple-output fixed array sensor configuration. In this section, the MUDT algorithm is formulated.

2.3.1 Forward model

In the above integral expression of Equation (2.12), in addition to the object function, the total electric field in the ROI is unknown. In order to have a fast solution in real-time, the integral must be linearized. By applying the first-order Born approximation that converts intrinsically a non-linear problem to a linear one, the total electric field can be replaced by the background electric field of the layer as follows

$$\vec{E}_n^{\mathrm{tot}}(\vec{r}', \Delta\varepsilon(\vec{r}')) \approx \vec{E}_n^{\mathrm{inc}}(\vec{r}') \tag{2.28}$$

Due to the excitation by a point source, the incident electric field can be replaced by the background Green's function and can be expressed $\vec{E}^{\mathrm{inc}}(\vec{r}, \vec{r}') \approx \hat{x}.\bar{\bar{G}}_{\mathrm{e}}^{(n0)}$. Moreover, using the reciprocity theorems, it can be written $\left[\bar{\bar{G}}_{\mathrm{e}}^{(n0)}(\vec{r}', \vec{r})\right]^T = \bar{\bar{G}}_{\mathrm{e}}^{(n0)}(\vec{r}, \vec{r}')$ [94]. Hence, a model for the scattering electric field can be derived [94]

$$\vec{E}_n^{\mathrm{sct}}(\vec{r}_r, \vec{r}_t) = k^2 \int_{\Omega_n} \hat{x}.\bar{\bar{G}}_{\mathrm{e}}^{(n0)}(\vec{r}_r, \vec{r}') \cdot O_n(\vec{r}')\hat{x}.\bar{\bar{G}}_{\mathrm{e}}^{(n0)}(\vec{r}', \vec{r}_t)\, d\vec{r}'. \tag{2.29}$$

where $O_n(\vec{r}) = \Delta\varepsilon(\vec{r}) = \left[\varepsilon_{r,n}(\vec{r}) - \varepsilon_{r,n}\right]$. As mentioned earlier, both transmitting and receiving antennas are assumed as $\hat{x}$-polarized and equivalent current is predominantly $\hat{x}$-polarized, so the following scalar model for the multistatic scenario can be attained

$$E_n^{\mathrm{sct}}(\vec{r}_r, \vec{r}_t) = k^2 \int_{\Omega_n} G_{\mathrm{e}}^{(n0)}(\vec{r}_r, \vec{r}\,') O_n(\vec{r}\,') G_{\mathrm{e}}^{(n0)}(\vec{r}\,', \vec{r}_t)\, d\vec{r}\,'. \tag{2.30}$$

The spectral representation of Green's function in layer n when the line source is located in the region 0 is

$$\begin{aligned} G_{\mathrm{e}}^{(n0)}(\vec{r}, \vec{r}_t) = \frac{1}{\pi} \int_{-\infty}^{+\infty} \frac{1}{k_{z0}} \Big[& T_n^{\mathrm{TM}}(k_y) e^{-jk_{zn}(z-z_t)} \\ & + R_n^{\mathrm{TM}}(k_y) e^{+jk_{zn}(z-z_t)} \Big] \cdot e^{-jk_y(y-y_t)} dk_y, \end{aligned} \tag{2.31}$$

As mentioned earlier, the electric field is composed of the incident and reflected parts. Here, it's assumed the contrast between the layers is small, therefore, the reflected electric field is not zero but negligible compared to the transmitted field inside that layer.

To show this effect, in Fig. 2.2, the electric field response at 8 GHz and 12 GHz from COMSOL multiphysics simulation software based on the finite element method (FEM) and the analytical formulations computed in MATLAB are compared. For the COMSOL simulation, the imaging domain consists of three layered media with $\varepsilon_{r,0} = 1$, $\varepsilon_{r,1} = 1.16$, and $\varepsilon_{r,2} = 1$ with thickness $t_0 = 10\,\mathrm{cm}$, $t_1 = 8\,\mathrm{cm}$, and t_2 is infinite free space, respectively. Open regions are truncated by using a perfectly matched layer (PML) of the circular shape of the inner radius and outer radius of 80 cm and 90 cm, respectively. The imaging medium is excited by a line current with an amplitude of 1 A and placed at (0 cm, 16 cm). The following parameters are set to define the triangular mesh in the model: maximum element size = 0.5 cm, minimum element size: 3.6×10^{-2} cm, maximum element growth rate= 1.1, curvature factor= 0.2. To simulate the electric field response, the electromagnetic module is employed with electromagnetic waves (emw) interface in the frequency domain. It is clear that the results of FEM and numerical integration are in excellent agreement. Moreover, to better represent the differences between the analytical model and FEM, the normalized root means square error (NRMSE) is calculated, and the result is shown in Table

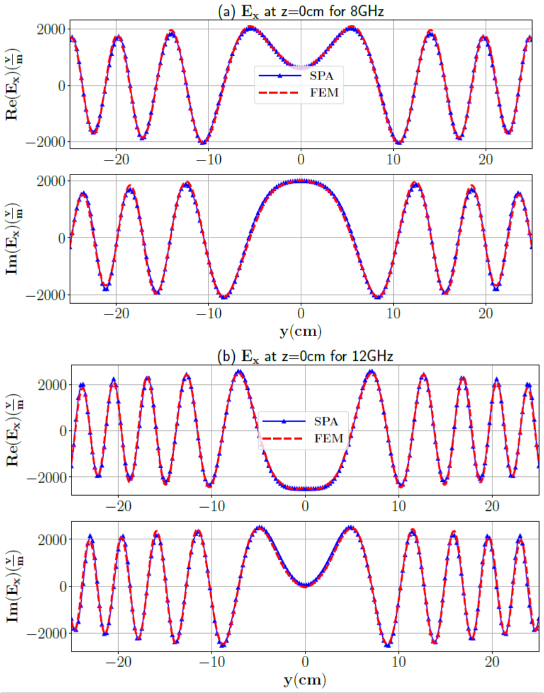

Fig. 2.2: The real and imaginary part of the total electric field component inside a three-layer media with dimension 50 cm × 8 cm and $\varepsilon_{r,1} = 1.16$ field for frequency of (top) 8 GHz and (bottom) 12 GHz.

Table 2.1: NRMSE error values for compared analytical model and FEM in Fig. 2.2.

	$Re(E_x)$, 8 GHz	$Im(E_x)$, 8 GHz	$Re(E_x)$, 12 GHz	$Im(E_x)$, 12 GHz
NRMSE %	1.76	2.06	2.11	2.74

2.1. From the NRMSE, it is clear that the SPA and FEM of COMSOL are in good agreement. As a consequence, the Green's function of any layer is approximated only by the transmitted part as an asymptotic Green's function expression, i.e, $G_{\mathrm{e}}^{(n0)} \approxeq G_{\mathrm{T}}^{(n0)}$, and by substitution in (2.30), it can be obtained

$$\begin{aligned} E_n^{\mathrm{sct}}(\vec{r}_r,\vec{r}_t) = \frac{k^2}{\pi^2}\int_{\Omega_n} O_n(y',z')\Bigg(&\int_{-\infty}^{+\infty}\int_{-\infty}^{+\infty} dk_y dk_y' \\ &\frac{T_n^{\mathrm{TM}}(k_y)T_n^{\mathrm{TM}}(k_y')}{k_{z0}k_{z0}'}\, e^{-j\left[(k_y+k_y')y' - k_y y_r - k_y' y_t\right]} \\ &\cdot\, e^{-j\left[(k_{zn}+k_{zn}')(z' - \sum\limits_{q=0}^{n-1} t_q) + \sum\limits_{q=0}^{n-1}(k_{zq}+k_{zq}')t_q\right]}\Bigg) dr', \end{aligned} \tag{2.32}$$

where $G_{\mathrm{T}}^{(n0)}$ is replaced with the primed variable for the second integral. This is the scattered field obtained due to the irregularities in layer n for a multistatic array scenario. This representation enables to use of all the transmitter-receiver pairs of the multistatic configuration. In comparison to the monostatic configuration (with $y_r = y_t$), more spectral components of the embedded targets can be recorded by the multistatic array, and also, higher order spectral frequency components are more discernible. For intuitive explanations of the above, consider two scatterers with their both centers positions at y_1 and y_2 the same z-position separated by a distance $L = y_1 - y_2$. The first phase term in (2.32) can be recast in the monostatic case as $(k_y + k_y')(y' - y_{ri})$ for the i^{th} receiver. Since the spectral domain of integration is from negative infinity to infinity, a pair of high-frequency terms (k_y, k_y') can satisfy $(k_{y1} + k_{y1}')(y_1 - y_{ri}) = (k_{y2} + k_{y2}')(y_2 - y_{ri})$. This implies the spectral components are indiscernible. As a consequence, secondary fields from the targets are indistinguishable at the receiver position. As a result, it is expected that a higher distortion effect in the case of multiple scatterers for the monostatic case if compared with the multistatic case.

2.3.2 MUDT inversion scheme

To obtain the analytical expression of the object function that contains the scattered field information in the multistatic scenario, one begins with the spatial Fourier Transform (FT) of the received scattered field at y_r due to the transmitter at y_t. The FT pair is defined as

$$E_n^{\mathrm{sct}}(y_t, y_r, \omega) = \frac{1}{2\pi} \int_{-\infty}^{+\infty} \tilde{E}_n^{\mathrm{sct}}(k_y, \omega) e^{jk_y y_t} dk_y, \tag{2.33}$$

$$\tilde{E}_n^{\mathrm{sct}}(k_y, \omega) = \int_{-\infty}^{+\infty} E_n^{\mathrm{sct}}(y_t, y_r, \omega) e^{-jk_y y_t} dy_t. \tag{2.34}$$

the spectral representation of the scattered field in the multistatic case can be written as

$$\begin{aligned}\tilde{E}_n^{\mathrm{sct}}(k_y'', \omega) = \frac{2k^2}{\pi} \int_{\Omega_n} & O_n(y', z') e^{-jk_y'' y'} \\ & \left(\int_{-\infty}^{+\infty} \frac{k^2}{k_{z0} k_{z0}'} T_n^{\mathrm{TM}}(k_y) T_n^{\mathrm{TM}}(k_y'' - k_y) e^{-j\left[k_y(y_t - y_r)\right]} \right. \\ & \left. \cdot\, e^{-j\left[(k_{zn} + k_{zn}')(z' - \sum_{q=0}^{n-1} t_q) + \sum_{q=0}^{n-1} (k_{zq} + k_{zq}') t_q\right]} dk_y \right) dr', \end{aligned} \tag{2.35}$$

where $k_y'' = k_y + k_y'$, and

$$k_{zn}' = \sqrt{k_n^2 - (k_y'' - k_y)^2}. \tag{2.36}$$

The term $k_y(y_t - y_r)$ in the phase of the inner integral of eq. (2.35) is the difference between UDT and MUDT. Comparing (2.18) and the inner integral of eq. (2.35), can write

$$f(h) = \frac{k^2}{k_{z0} k_{z0}'} T_n^{\mathrm{TM}}(k_y) T_n^{\mathrm{TM}}(k_y'' - k_y), \tag{2.37}$$

$$\phi(h) = \frac{1}{k_0}\left[k_y(y_t - y_r)\right] + \frac{1}{k_0}\left[(k_{zn} + k_{zn}')(z' - \sum_{q=0}^{n-1} t_q) + \sum_{q=0}^{n-1} (k_{zq} + k_{zq}') t_q\right] \tag{2.38}$$

where $h = k_y$, and $\kappa = k_0 z$. The stationary phase approximation is calculated with respect to the $k_0 z$. This assumption is a general case compared to applying the stationary phase with respect to the k_0 which provides a smooth transition at boundaries in the presence of a target. The second integral in (2.35) can be simplified, and the above expression reduces to a simple form given

$$\begin{aligned}\tilde{E}_n^{\mathrm{sct}}(k_y'', \omega) = \frac{2}{\pi} \int_{\Omega_n} & O_n(y', z') e^{-jk_y'' y'} \frac{k^2}{\bar{k}_{z0} \bar{k}_{z0}'} T_n^{\mathrm{TM}}(\bar{k}_y) T_n^{\mathrm{TM}}(k_y'' - \bar{k}_y) \\ & \left[\frac{2\pi}{k_0 z |\phi''(\bar{k}_y)|}\right]^{\frac{1}{2}} e^{-j(\frac{\beta}{2} + \frac{\pi}{4})} e^{[\bar{k}_y (y_t - y_r)]} \\ & \cdot e^{-j\left[(\bar{k}_{zn} + \bar{k}_{zn}')\left(z' - \sum\limits_{q=0}^{n-1} t_q\right) + \sum\limits_{q=0}^{n-1} (\bar{k}_{zq} + \bar{k}_{zq}') t_q\right]} dr', \end{aligned} \tag{2.39}$$

where

$$\phi''(\bar{k}_y) = -\frac{k_n^2}{k_0}\left(\frac{1}{\bar{k}_{zn}^3} + \frac{1}{\bar{k}'^3_{zn}}\right)\left(1 - \sum_{q=0}^{n-1} \frac{t_q}{z}\right) - \sum_{l=0}^{n-1} \frac{k_q^2}{k_0}\left(\frac{1}{\bar{k}_{zq}^3} + \frac{1}{\bar{k}'_{zq}{}^3}\right), \tag{2.40}$$

$$\phi''(\bar{k}_y) = |\phi''(\bar{k}_y)| e^{j\beta}, \tag{2.41}$$

and $\bar{k}_y$ is the solution of the following equation:

$$\begin{aligned}\frac{1}{k_0 z}(y_t - y_r) + \frac{1}{k_0}\left(-\frac{\bar{k}_y}{k_{zn}} + \frac{k_y'' - \bar{k}_y}{k_{zn}}\right)\left(1 - \sum_{q=0}^{n-1} \frac{t_q}{z}\right) + \\ \sum_{q=0}^{n-1}\left(-\frac{\bar{k}_y}{k_{zq}} + \frac{k_y'' - \bar{k}_y}{k_{zq}}\right)\frac{t_q}{z} = 0.\end{aligned} \tag{2.42}$$

$$O_n(y,z) = \frac{\int_\omega \int_{-\infty}^{+\infty} \frac{k_{z0}k''_{z0}}{k_n^2} \frac{e^{j(\frac{\beta}{2}+\frac{\pi}{4})}}{T_n^{\mathrm{TM}}(\bar{k}_y)T_n^{\mathrm{TM}}(k''_y-\bar{k}_y)} e^{j\left[\bar{k}_y(y_t-y_r)\right]} e^{j\left[k''_{zn}\sum_{q=0}^{n-1} t_q - \sum_{q=0}^{n-1} k''_{zq}t_q\right]} \tilde{E}^{\mathrm{sct}}(k''_y,k)M(k''_y)dk''_y d\omega}{(\frac{\pi}{8})^{\frac{1}{2}} \int_\omega \int_{-\infty}^{+\infty} \frac{M(k''_y)}{\left[k_0 z|\phi''(\bar{k}_y)|\right]^{\frac{1}{2}}} dk''_y d\omega} \tag{2.45}$$

Here, $\bar{k}_{zn}$, $\bar{k}'_{zn}$ are those defined earlier when k_y is replaced by $\bar{k}_y$.
After some arrangement, the above integral can be written as follow

$$\tilde{E}_n^{\mathrm{sct}}(k''_y,\omega) = \frac{2}{\pi}\frac{k^2}{\bar{k}_{z0}\bar{k}'_{z0}} T_n^{\mathrm{TM}}(\bar{k}_y)T_n^{\mathrm{TM}}(k''_y-\bar{k}_y) e^{-j(\frac{\beta}{2}+\frac{\pi}{4})} e^{-j\left[\bar{k}_y(y_t-y_r)\right]}$$
$$\cdot e^{-j\left[\sum_{q=0}^{n-1}\bar{k}''_{zq}t_q - \bar{k}''_{zn}\sum_{q=0}^{n-1}t_q\right]} \int_{\Omega_n} \frac{O_n(y',z')}{\left[\frac{k_0 z}{2\pi}|\phi''(\bar{k}_y)|\right]^{\frac{1}{2}}} e^{-j(k''_y y + k''_z z)} dr', \tag{2.43}$$

where $k''_z = \bar{k}_z + \bar{k}'_z$. Using the definition for the spectral reflectivity [77]

$$\tilde{O}_n(k''_y,k''_z,k) = \int\int_{\Omega_n} \frac{O_n(y',z')}{\left[\frac{k_0 z}{2\pi}|\phi''(\bar{k}_y)|\right]^{\frac{1}{2}}} e^{-j(k''_y y + k''_z z)} dydz, \tag{2.44}$$

a linear relation between the scattered field and reflectivity function can be obtained
Substituting eq. (2.45) in eq. (2.39), the object function can be obtained as represented in (2.45) at the top of the page, where

$$M(k''_y) = \frac{\omega\varepsilon}{c^2}\left[\left(k_n^2-(k''_y-\bar{k}_y)\right)^{-\frac{1}{2}} + \left(k_n^2-\bar{k}_y\right)^{-\frac{1}{2}}\right]. \tag{2.46}$$

Equation (2.45) expresses a relation between the spatial Fourier transform of the scattered field and the contrast function.

For the implementation of the MUDT algorithm, the position of each transmitter-receiver pair in the multistatic array is approximated by its mid-point which is equivalent to a monostatic array configuration. This implies that each of the N_1 elements of the multistatic array can be replaced by the $N_2 \geq N_1$ elements in the equivalent configuration and represented $N_1 : N_2$. In this case, the spatial sampling rate will be $L/(2N_1N_2)$ where L is the length of N_1 elements in multistatic array. For example, $1 : 2$ denotes 1 elements of the multistatic array are replaced by 2 element in the equivalent monostatic array this implies that 13 sampling points exist for 7 element antenna array. Conceivably, the aforementioned procedure is stated to be very similar to the effective aperture concept utilized in multistatic mm-wave imaging systems [108–110].

2.4 Time-Reversal Imaging

The following section will present the TR imaging algorithm and demonstrate its integration with Green's function of the multilayered media to facilitate microwave imaging of high-contrast multilayered media. This is particularly useful when the media is supported by a PEC plate.

2.4.1 Concept and theory of time reversal

The TR concept was first introduced for ultrasonic applications to locate the position of inhomogeneity in a certain media [60, 81]. In a non-dispersive and linear media, where the permittivity ε does not vary with time, the wave equation is time-symmetric. Both $\vec{\mathcal{E}}(\vec{r},t)$ and $\vec{\mathcal{E}}(\vec{r},-t)$ are solutions of the well-known wave equation

$$\nabla^2 \vec{\mathcal{E}}(\vec{r},t) - \mu\varepsilon \frac{\partial^2}{\partial t^2} \vec{\mathcal{E}}(\vec{r},t) = 0 \tag{2.47}$$

where μ and ε denote the permeability and permittivity of the medium, respectively. $\mathcal{E}$ is the electric field in the time domain. $\vec{r}$ denotes any point in the media, and t represents the time. This guarantees for any EM wave diverging away from a source that there exists a "time-reversed" EM wave that precisely retraces the path of the original EM wave back to the source.

To experimentally examine the TR method, an excitation signal is sent to the region of interest, and the reflected signal is recorded using the transducers surrounding the media. The received signal is time-reversed and used as a new excitation for the transducers. Later, this new excitation (time-reversed signal) is retransmitted to the region of interest. It is observed that the newly sent signals focus on the target (inhomogeneity). It shows that the converged time-reversed signals travel the same path as the diverged signal travels from the inhomogeneity [80]. TR methods have been used widely in many areas like ultrasound, microwave, millimeter-wave, and optic. Nevertheless, existing TR imaging algorithms encounter challenges in accurately reconstructing target locations within high-contrast multilayered media, as they do not account for the reflected part of the Green's function. In the following, the TR theory for microwave image generation in multilayered media is reviewed, and the extension of the TR method to the high-contrast media is investigated and analyzed.

2.4.2 Scattering model and time-reversal imaging

Consider an active array of N transceivers from which an $N \times N$ MDM is constructed. Each element in the MDM matrix corresponds to the scattered field received by the l^{th} $(l = 1, 2, \ldots, N)$ antenna when the s^{th} $(s = 1, 2, \ldots, N)$ antenna transmits, due to the presence of inhomogeneities in the region of interest [94, 95, 111]

$$\bar{\bar{G}}_{\mathrm{s}}(\vec{r}_{r_l}, \vec{r}_{t_s}) = k^2 \int\int\int_{\Omega_1} \bar{\bar{G}}_{\mathrm{e}}^{(0n)}(\vec{r}_{r_l}, \vec{r}') \cdot O(\vec{r}')\bar{\bar{G}}_{\mathrm{e}}(\vec{r}', \vec{r}_{t_s}) d\vec{r}' \tag{2.48}$$

Here, $\bar{\bar{G}}_{\mathrm{e}}(\vec{r}', \vec{r}_{t_s})$ denotes the total electric Green's function in the presence of irregularities, $\bar{\bar{G}}_{\mathrm{s}}(\vec{r}_{r_l}, \vec{r}_{t_s})$ is the Green's function when there are no irregularities in the media, and where $O_n(\vec{r}) = \Delta\varepsilon(\vec{r}) = \left[\varepsilon_{r,n}(\vec{r}) - \varepsilon_{r,n}\right]$. The MDM matrix will be constructed from $\bar{\bar{G}}_\mathrm{s}$. It should be noted, that there is no assumption in the above expression, and (2.48) is exact. In many applications, the calculation of the total Green's function of a media is difficult. Hence, a proper estimation for $\bar{\bar{G}}_\mathrm{e}(\vec{r}', \vec{r}_{t_s})$ is inevitable. In (2.48), the vectors $\vec{r}_r$ and $\vec{r}_t$ represent the points of the transmitter and receiver while $\vec{r}' = (y', z')$ is the location of the pixel point in the ROI. $\bar{\bar{G}}_\mathrm{eb}^{(0n)}$ is the background (multilayer media without any inhomogeneities) DGF. The superscript $(0n)$ denotes that the source point is located in layer n and the observation point is in layer 0. It should be noted that the analytical equations are written for the electric fields, however, in real scenarios, the S-parameters will be measured. Hence, a de-embedding procedure will be applied later to relate the measured S-parameters to the electric field. The details of the employed procedure are represented in [78, 79, 92].

Using the Born approximation, the total Green's function will be replaced by the Green's function of the media when there are no irregularities. Hence, (2.48) can be approximated as follow:

$$\bar{\bar{G}}_\mathrm{s}(\vec{r}_{r_l}, \vec{r}_{t_s}) \approx k^2 \int\int\int_{\Omega_1} \left[\bar{\bar{G}}_\mathrm{e}^{(0n)}(\vec{r}_{r_l}, \vec{r}')\right]^T \cdot O(\vec{r}')\bar{\bar{G}}_\mathrm{e}(\vec{r}', \vec{r}_{t_s})d\vec{r}'. \tag{2.49}$$

Assuming that the transmitting and receiving antennas are both polarized in the x direction and that the dominant currents are x-polarized, the Eq. (2.49) can be written in scalar form [91]. This allows for the creation of a multistatic model that describes the received scattered field for each element of the multistatic data matrix (MDM) as

$$k_{ls} = k^2 \int\int\int_{\Omega_1} G_\mathrm{e}(\vec{r}_{r_l}, \vec{r}')O(\vec{r}')G_\mathrm{e}(\vec{r}', \vec{r}_{t_s})d\vec{r}'. \tag{2.50}$$

k_{ls} corresponds to signal received at l^{th} antenna when the s^{th} antenna is used as the transmitter shown in Fig. 2.3 (left). In deriving (2.50) from (2.49) the symmetry property [95] of the DGF is used. The $N \times N$ symmetric (due

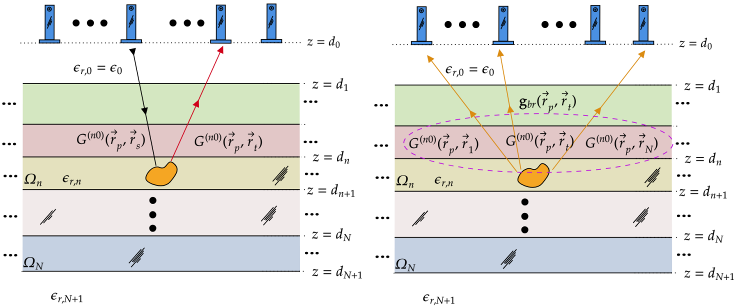

Fig. 2.3: Visualizations of obtaining $k_{ij}(\omega)$ and the steering vector (in the absence of multiple scattering among scatterers): (a) $k_{ij}(\omega)$ is obtained by transmitting a short pulse from the jth antenna and recording the received scattered field at the ith antenna, (b) Steering vectors connecting each scatterer to the array elements.

to the reciprocity) MDM denoted as $\boldsymbol{K}(\omega)$ can be expressed in a compact form in the angular frequency domain ω

$$\boldsymbol{K}(\omega) = k^2 \int\int\int_{\Omega_1} O(\vec{r}')\mathbf{g}_{br_l}(\vec{r}', \omega)\mathbf{g}_{br_s}^{\top}(\vec{r}', \omega)d\vec{r}', \tag{2.51}$$

where $\mathbf{g}_{br_l}$ and $\mathbf{g}_{br_s}$ are $N \times 1$ frequency-domain Green's function vectors of the background Green's function and $(\cdot)^{\top}$ is the transpose operator shown in Fig. 2.3 (right).

$$\mathbf{g}_{br} = [G_e(\vec{r}, \vec{r}_1), G_e(\vec{r}, \vec{r}_2), ..., G_e(\vec{r}, \vec{r}_N)]_{\mathrm{N}\times 1}, \tag{2.52}$$

The Green's function vector relates the scatterer's location in the media to the array of antennas.

It has been shown the eigenstructure of the MDM matrix has valuable information about the target location in the ROI [82]. The SVD of the matrix $\boldsymbol{K}(\omega)$ is expressed in terms of the eigenvalues as follow

$$\boldsymbol{K}(\omega) = \boldsymbol{U}(\omega) \cdot \boldsymbol{\Sigma}(\omega) \cdot \boldsymbol{V}^{\dagger}(\omega) \tag{2.53}$$

where † is the transposed conjugated operator. $\boldsymbol{\Sigma}\ \Big(\mathrm{diag}(\Sigma) = [s_1, s_2, \ldots, s_N]\Big)$ is a real diagonal matrix consisting of eigenvalues, while $\boldsymbol{U}\ \Big(\mathbf{u}_l(\omega), l =$

$1, 2, \ldots, N\big)$ and $\boldsymbol{V}$ $\big(\mathbf{v}_l(\omega), l = 1, 2, \ldots, N\big)$ are the left and right matrices consisting of normalized eigenvectors [63] of the TRO formed. From the eigenvalue and eigenvector definition, it can be written as:

$$\boldsymbol{K}(\omega)\mathbf{v}_i(\omega) = s_i(\omega)\mathbf{u}_i(\omega) \tag{2.54}$$

$$\boldsymbol{K}^{\dagger}(\omega)\mathbf{u}_i(\omega) = s_i^*(\omega)\mathbf{v}_i(\omega) \tag{2.55}$$

where s^* denotes the complex conjugate of s. Substituting the Eq. (2.51) in Eq. (2.54) yields

$$k^2 \int\int\int_{\Omega_1} O(\vec{r}')\mathbf{g}_{br_l}(\vec{r}', \omega)\mathbf{g}_{br_s}^{\top}(\vec{r}', \omega)d\vec{r}' = s_i\mathbf{u}_i(\omega) \tag{2.56}$$

By defining the inner product as $< x, y >= y^{\dagger}x = \int y_i^* x_i$, the left singular value can be written as follow

$$\mathbf{u}_i(\omega) = s_i(\omega)^{-1}k^2 \int\int\int_{\Omega_n} O(\vec{r}') < \mathbf{v}_i(\omega), \mathbf{g}_{br_s}^{*}(\vec{r}', \omega) > \mathbf{g}_{br_l}(\vec{r}', \omega)d\vec{r}' \tag{2.57}$$

The (2.57) represents that the left singular vector of the MDM matrix can be expressed as a linear combination of the steering vectors of the antenna which relates the target location to the time-reversal array. Analogous, the right singular vector can be written

$$\mathbf{v}_i(\omega) = s_i^*(\omega)^{-1}k^2 \int\int\int_{\Omega_n} O^*(\vec{r}') < \mathbf{u}_i(\omega), \mathbf{g}_{br_l}(\vec{r}', \omega) > \mathbf{g}_{br_s}^*(\vec{r}', \omega)d\vec{r}', \tag{2.58}$$

as can be seen from (2.57) and (2.58), the left and right singular vectors satisfy with the following equation

$$\mathbf{u}_i(\omega) = \mathbf{v}_i^*(\omega), \quad i = 1, 2, \ldots, N \tag{2.59}$$

It is because of the symmetry of $\boldsymbol{K}(\omega)$. It can be shown the following choice for the right and left eigenvector, and the eigenvalue can satisfy the singular system.

$$\mathbf{u}_i = \frac{\mathbf{g}_b(x_i, \omega)}{\left\|\mathbf{g}_b(x_i, \omega)\right\|} = \frac{\mathbf{g}_T(x_i, \omega) + \mathbf{g}_R(x_i, \omega)}{\left\|\mathbf{g}_b(x_i, \omega)\right\|} \quad i = 1, 2, \ldots, M \tag{2.60}$$

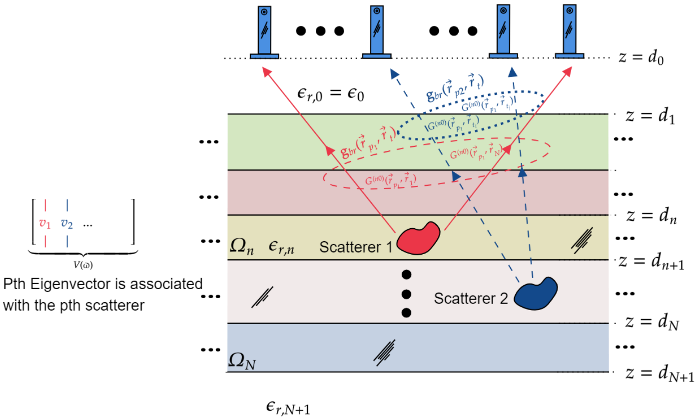

Fig. 2.4: Each significant eigenvalue and corresponding eigenvector of the TRO is associated with a single scatter in the domain. Specifically, each eigenvector is proportional to the steering vector connecting the single scatterer to the TR array antennas.

$$\mathbf{v}_i = \frac{\mathbf{g}_b^*(x_i,\omega)}{\left\|\mathbf{g}_b(x_i,\omega)\right\|} = \frac{\mathbf{g}_T^*(x_i,\omega) + \mathbf{g}_R^*(x_i,\omega)}{\left\|\mathbf{g}_b(x_i,\omega)\right\|} \quad i = 1, 2, \dots, M, \tag{2.61}$$

where the corresponding eigenvalues are

$$s_i(\omega) = k_0^2 \left\|\mathbf{g}_b(x_i,\omega)\right\|^2 \quad i = 1, 2, \dots, M, \tag{2.62}$$

So, each eigenvalue and corresponding eigenvector are associated with one target in ROI. By backpropagating the corresponding eigenvector, the focus on the target will be achieved. Earlier it was mentioned that the eigenvalues and eigenvectors of the TRO are dependent on the media's Green's function. In the case of non-high-contrast media, the green function can be substituted with the incident part ($g_b(x_i,\omega) \approx g_T(x_i,\omega)$), resulting in same eigenvalues and eigenvectors, ensuring accurate TR performance. However, neglecting the reflected part of the Green's function in high-contrast media leads to a notable discrepancy in the eigenvalues and eigenvectors, causing errors or significant shadowing effects in the reconstructed images.

Hence, if the array of antennas excites by the proper eigenvectors, plotting the electric field in the media represents a concentration near the irregularity. The number of eigenvalues (EV) with significant values denotes the number of dominant inhomogeneities present in the background medium. The remaining eigenvalues form the noise subspace. Hence, for focusing on the p^{th} target, the excitation of the TRA can be written as

$$e_p(\omega) = \boldsymbol{K}^{\dagger}(\omega)\mathbf{u}_p = s_p^* \frac{\mathbf{g}_b(x_p, \omega)}{\left\|\mathbf{g}_b(x_p, \omega)\right\|} \tag{2.63}$$

Here, s_p is the p^{th} eigenvalue and $\boldsymbol{u}_p$ is the p^{th} left singular vector. By back-propagating the mentioned excitation for the TRA using Green's function of the multilayered media, the focus on the p^{th} target can be achieved. As a result the location of p^{th} scatterer is synthetically obtained by the following imaging function

$$\boldsymbol{D}_p(\vec{r}) = \int_{\omega} \boldsymbol{e}_p^T(\omega) g_{br}(\vec{r}, \omega) d\omega, \tag{2.64}$$

where $\vec{r}$ is any arbitrary point in the ROI. The excitation for the p^{th} target is associated with the steering vector from the target to the TRA, and in the time domain, this excitation undergoes convolution with the Green's function of the media. At locations where $r' = \vec{r}_p$, this convolution reaches its maximum; otherwise, the product is zero. It is crucial to emphasize that utilizing only the transmission part of the Green's function can result in incorrect excitation of the TRA, leading to inaccuracies in the reconstructed image.

3 Experimental Setup

Designing and integrating a microwave diagnostics system into an industrial microwave drying system is a challenging task. These challenges come from the different restraints that have to be correctly considered and addressed for the successful operation of the system in industrial applications. Typically in biomedical and GPR applications, the lower GHz frequency range (0.5 GHz to 3 GHz) is desired to reach enough penetration into a lossy tissue or ground. However, the case might differ in an industrial scenario. For example, consider a high-power microwave drying system as shown in Fig. 1.4. The name is considered based on the patented HEPHAISTOS technology. The operational frequency of the HEPHAISTOS oven is 2.45 GHz. A conveyor belt, supported on a metal plate, is installed that enables a continuous drying process with the different variety of speeds. It delivers a total of 36 kW of microwave power. Hence, the unwanted EM leakage power coming from the entrance aperture can take down the near-operating MWT system and, it has to be blocked. In this regard, various types of antennas that are already employed for microwave imaging purposes can not be used in this application, like e.g. corrugated tapered slot antennas [112], ultra-wideband (UWB) tapered slot antenna [113], cavity backed aperture stacked patch antenna [114], and Vivaldi antennas [115].
An appropriate choice could be to move to the X-band for the MWT and employ WR90 open-waveguide [116, 117] to act simultaneously as an antenna and microwave stop band for the 2.45 GHz ISM band. Being in the cut-off region of the WR90 waveguide for the X-band, the EM field decays with $e^{-\alpha z}$ (z is the direction of propagating) at 2.45 GHz where α is the attenuation constant, providing more than 100 dB isolation along with the waveguide antenna with a length of 15.2 cm. In [118], a Vivaldi antenna is used to (i) create a single polarization that is compatible with the quantitative imaging algorithm, (ii) provide sufficient information in close vicinity of the object of interest, and (iii) provide a low mutual coupling between two adjacent

elements. Those parameters are essential for the proper performance of the proposed imaging algorithm. However, changing the type of antenna may strongly impact this fact since the mentioned constraints may not be met anymore.

By using a limited number of antennas, some current imaging algorithms may not be applied properly to reconstruct the image. For instance, numerous microwave imaging algorithms are compatible with a high number of data (or sampling data), and the performance will decrease or even annihilate when the number of antennas is not high enough. For example, in [77] and [27], 20 and 51 antennas are used with an aperture length of 20 cm and 120 cm to reconstruct the image in a layered media, and behind a cinder block wall, respectively. It is obvious the implementation of this number of antennas in a fixed aperture length may not be feasible due to the structure of the antenna or the acquisition time. So, a low number of the antenna is preferable, which leads to an inaccurate reconstructed image from the media.

Furthermore, fast DAQ is also essential to enable real-time monitoring and process control. Hence, choosing a limited number of antennas and arranging a limited-aspect configuration is inevitable. For continuous or batch processing, a metal plate is sometimes installed in a conveyor belt system that should be considered in the forward model/physical formulation. Otherwise, image reconstruction may be erroneous. For image reconstruction which can support low data from a low number of antennas, neural networks [119–121] have shown promising capabilities that may estimate the moisture in real-time (1 s) [122, 123] in comparison to iterative-based imaging algorithm. However, their performance can be plagued with changes in foam type, dimensions, and electrical properties; in that case, the network requires re-training. This necessitates the development of new algorithms and techniques for image-reconstruction purposes.

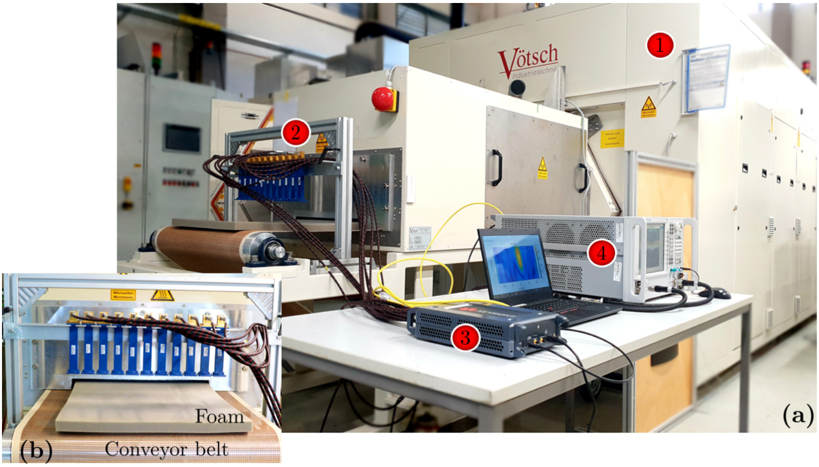

Fig. 3.1: (a) MWT system and its integration with the HEPHAISTOS (number Tag 1) is shown. The number Tags 2, 3, and 4 shows the MWT system, Solid state switch, and VNA respectively. (b) shows the enlarged view of the MWT sensor array of X-band open-ended waveguide antennas. Note here only 7 antennas are used in the measurement with the polymer foam.

3.1 Measurement setup

As shown in Fig. 3.1, an MWT setup is installed next to a high power microwave drying system. The MWT system consists of 11 WR90 open-ended waveguide antennas (VSWR 1.03 : 1) connected (using cables with phase stability of 3° at the maximum frequency) to the Agilent N5224A vector network analyzer (VNA) with a P9164C 2×16 USB Solid state switch matrix with a power level of 5 dBm and an IF bandwidth 500 Hz. For each combination of the positioned antennas, two port waveguide calibration is performed to extract the response of the medium from the stored scattering matrix. To illustrate, when working with 12 antennas, a total of 66 waveguide calibrations are necessary. It's important to note that these calibrations are conducted prior to mounting the antennas onto the holder, simplifying the procedure. The data is acquired from 8 GHz to 12 GHz with a frequency step of 5 MHz. Communication between the VNA, switch, and the controlling

computer is conducted through the Ethernet cable. The DAQ process is entirely automated using MATLAB R2018b. A Multistatic antenna array resides in the semi-infinite free space from -15 cm to 15 cm along the y-axis and the distance of the top antenna to the top of the multilayered media is 12 cm. The center to center distance between two adjacent antennas is 5 cm. The setup is surrounded by the microwave absorber to increase the signal-to-noise ratio.
Without losing the generality for other applications, the current MWT system, the developed MWT system will be integrated with a high-power microwave drying system within the scope of the European TOMOCON project. In this project, the goal is to use the information (both location and value) within the media (polymer foam) obtained by the MWT system for intelligent control of the moisture of the products (foam with different thicknesses). In this regard, later, some wet-spots will be used as the target inside the media (polymer foam).

3.1.1 Minimum Received Signal

Two separate calibrations were conducted to determine the minimum signal level and observe the impact of the phase-stable cable. Fig. 3.2 shows that the minimum detectable signal level is approximately -80 dB without any additional cables. However, it is expected that the addition of the phase-stable cable will increase this minimum level. Following the addition of the phase-stable cable, another calibration was performed, and the results are

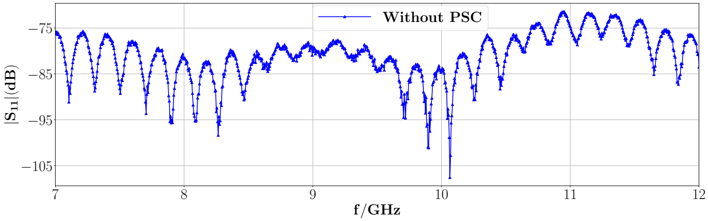

Fig. 3.2: The return loss when the cable is terminated to a broadband load.

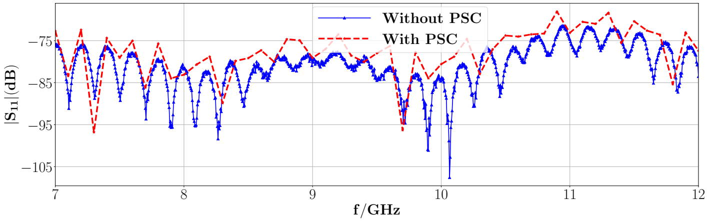

Fig. 3.3: The return loss when the cable and phase stable cable are terminated to a broadband load.

displayed in Fig. 3.3. This figure indicates that the signal level decreased by approximately 5 dB in the frequency band. In both scenarios, the minimum signal level at higher frequencies was greater than at lower frequencies. SMA calibration with short, open, and broadband loads were used to conduct these experiments. Furthermore, in both scenarios, some small reflections are visible. Because the cables were not stabilized using methods such as clamps, strain relief, or mechanical fixtures, there may have been slight shifts in cable positioning after the calibration and the mounting and dismounting of the loads, resulting in minor reflections in the measured data. Later, a time-gating procedure is used to remove this unwanted reflection from the measured data.

Fig. 3.4: A 2 × 16 USB 9164C Keysight Solid state switch used for the multistatic measurement.

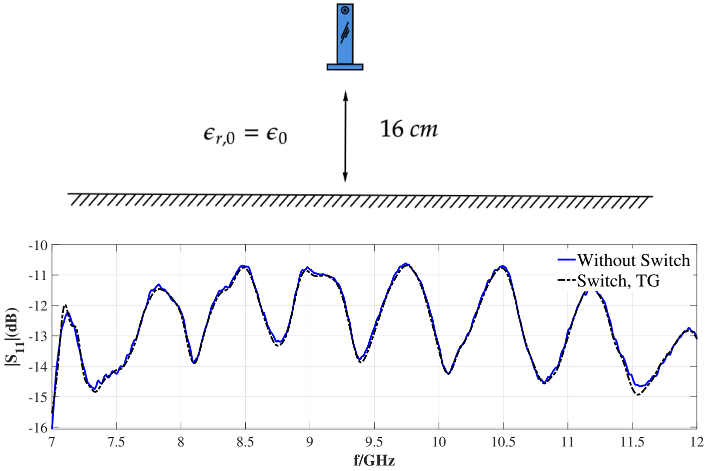

Fig. 3.5: (Top) An open waveguide antenna above a PEC plate, (bottom) the comparison of the return loss with/without the microwave switch.

3.1.2 Effect of the Switch

As the VNA utilized a two-port configuration, a microwave switch was employed to capture signals from all antennas. The employed switch is shown in Fig. 3.4. For accurate return loss measurement, it is crucial to terminate the unused ports with match loads. However, during the measurement process, the unused ports were not terminated as specified. Nevertheless, it has been observed that the isolation between different ports is sufficiently high to mitigate the impact of the unused ports. To assess the impact of this switch, two measurements were carried out, employing the configuration depicted in Figure 3.5 (top). In this scenario, an open waveguide antenna was positioned above a PEC plate. The first experiment involved connecting the open waveguide antenna directly to the VNA, while the second used a switch to connect the antenna to the VNA. The return loss with and without the switch remained unchanged, indicating proper switch performance, as depicted in Fig. 3.5. Therefore, as evident, the return loss remains identical with and without the switch, indicating the satisfactory performance of the switch, even when the unused ports are not terminated to the matching loads. It's worth mentioning, that in this experiment, a PEC plate was placed under the antenna, resulting in a semi-equal distance between the minimum locations in the return loss figure corresponding to the distance of the antenna to the PEC plate. It should be mentioned, that a time-gating process was applied when the microwave switch was installed to remove unwanted signals from the received signal. Additionally, three matched loads were terminated to the coaxial port of the switch to check isolation between different ports, and the results were consistent without using any matched load for the coaxial ports. A two-port waveguide calibration was used to exploit the response of the antenna from the measured return loss. For X-band waveguide calibration, a flush short and a waveguide load with a thickness of 4 mm (smaller than $\frac{\lambda}{4}$ at the center frequency) were selected, providing a delay of 133.3 ps in thru configuration assigned into the VNA for calibration purposes.

3.1.3 Signal to Noise Ratio

To determine the sensitivity of the microwave tomography system, the signal-to-noise ratio (SNR) was calculated for various scenarios. The SNR was defined as the ratio of the signal of interest to the noise level as follows

$$SNR = |\frac{S_{\text{sig}}}{S_{\text{noise}}}| \tag{3.1}$$

where S_{sig} and S_{noise} are the measured scattering parameters. The minimum detectable signal is measured and used as a reference for the noise level. Any signal lower than this value is considered as noise in the system. The measurement setup is depicted in Fig. 3.6(top), where three antennas are positioned at the distance of 12 cm above a polymer foam with a thickness of 7.6 cm and dielectric constant of $\varepsilon_{r,1} = 1.16$. In one scenario, the reflection response of an antenna is measured with and without a dielectric target with a dielectric constant of 2.1. Another measurement is conducted to measure the transmission response between two antennas with a center-to-center distance of 10 cm. Those responses, along with the minimum signal

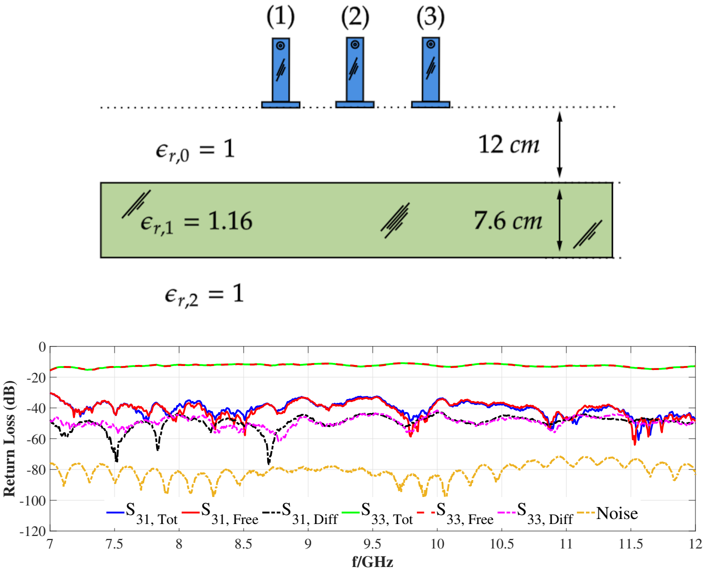

Fig. 3.6: (Top) The MWT setup for data collection, (bottom) the comparison of the return loss for different scenarios including from the media, and the targets inside it.

level, are plotted in Fig. 3.6. From Fig. 3.6, it is evident that the reflected signal ($|S_{11}|$) is 30 dB stronger than the transmitted signal between two antennas ($|S_{31}|$) in the scenario which the reflection response of an antenna is measured with and without a dielectric target with a dielectric constant of 2.1. By subtracting the responses with and without the target, the response of the target can be obtained in both reflection and transmission modes, which is approximately 30 dB stronger than the noise signal. To illustrate the differences, Fig. 3.7 shows the SNR for three scenarios. It should be mentioned, that those peaks in Fig. 3.7 are associated with the minimum in the measured noise. The received signal with and without any target in the media is around 75 dB, and the SNR of the target is approximately 35 dB.

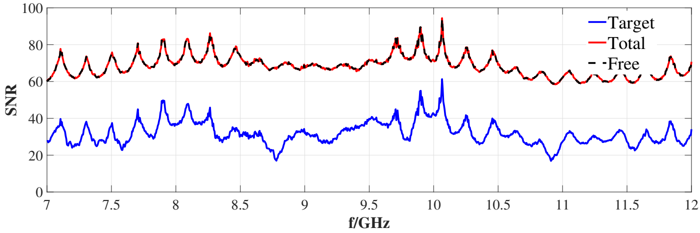

Fig. 3.7: SNR for the different scenarios.

3.1.4 CST Simulations

To assess the similarity between the measured and simulated scenarios in CST, the return loss in dB of a single antenna in free space is compared. As depicted in Fig. 3.8, the measured and simulated return losses exhibit good agreement within the X-band frequency range. Nevertheless, some differences become noticeable at higher frequencies. It's worth noting, however, that for the subsequent image reconstruction process, there won't be a direct comparison between the simulation and measurement data. Consequently, these differences hold no significance. In essence, the imaging algorithm relies on variations in the received scattered field relative to the other antennas in the same setup. Additionally, Fig. 3.9 displays the return loss of the antenna 4 (center antenna) for various dielectric constants in a spherical shape with a radius of 1.5 cm, highlighting the sensitivity of the measured data to changes in the dielectric constant. The different amounts of water are added to a foam sphere with the radius of 1.5 cm to create varying dielectric constants, and a dielectric characterization process is conducted to map the values to moisture content.

3.1.5 Dielectric characterization

In the dielectric characterization, a small cylinder of the foam is characterized as a cavity perturbation. It is used to obtain the complex dielectric value for different levels of moisture content. The developed dielectric measurement system is shown in Fig. 2. The foam sample is located in a quartz tube to have a stable position inside the cavity. Both sides of the cavity are terminated to a small iris of 10 mm width. It has the same height as the WR340 waveguides [38]. The moisture content is calculated on a wet basis using the equation

$$M\% = \frac{W_m - W_d}{W_m} \times 100 \tag{3.2}$$

where M is the moisture percentage, W_m is the weight of the foam sample after adding the water, and W_d is the weight of the dry sample. A mapping between the dielectric constant and the wet-basis moisture levels, measured by the cavity-perturbation method as well as transmission line technique [124] at 2.45 GHz is given in Table 3.1. For this characterization, the poly-

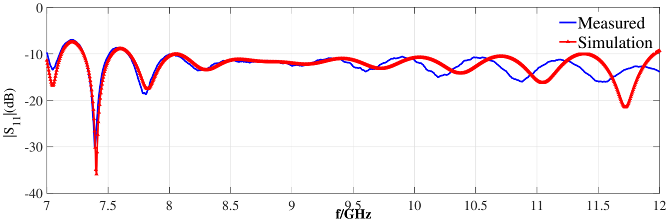

Fig. 3.8: Comparison between the simulated and measured return loss in dB of WR90 antenna.

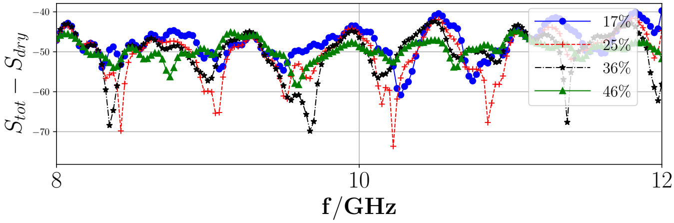

Fig. 3.9: Measured of the scattering response (in dB) in X-band of antenna 4 (middle antenna) for different moisture contents in the spherical wet-spot of radius 1.5 cm. S_{tot} and S_{dry} indicate the scattering response in the presence of the target and without targets, respectively.

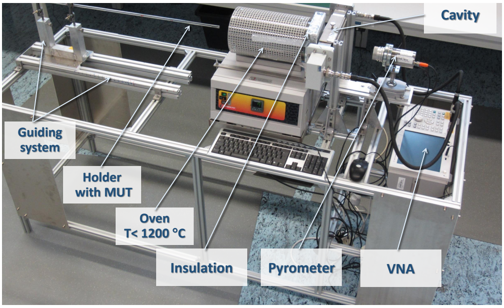

Fig. 3.10: Dielectric characterization of the polymer foam using cavity-perturbation method [124].

Table 3.1: Dielectric constant of the foam with different moisture contents $M_w\%$ on wet-basis.

$M_w\%$	0	30	36
ε_r	1.16-j0.01	1.69-j0.1	1.87-j0.12

mer foam density is 23 $\frac{kg}{m^3}$. Later, this characterization will be used for experimental studies.

Figure 2 displays another MWT setup where the media (Polymer foam) is encompassed by antennas. This specific configuration will be utilized in Chapter 5 for the Bayesian inversion framework. Twelve antennas are positioned, with six at the top and six at the bottom of the foam, spaced identically to the previous setup. In this configuration, both reflection and transmission data are required for accurate implementation of the Bayesian inversion framework. Although the number of antennas has increased, the MUDT algorithm, in conjunction with the proposed algorithm, can effectively reconstruct the target shape within the ROI.

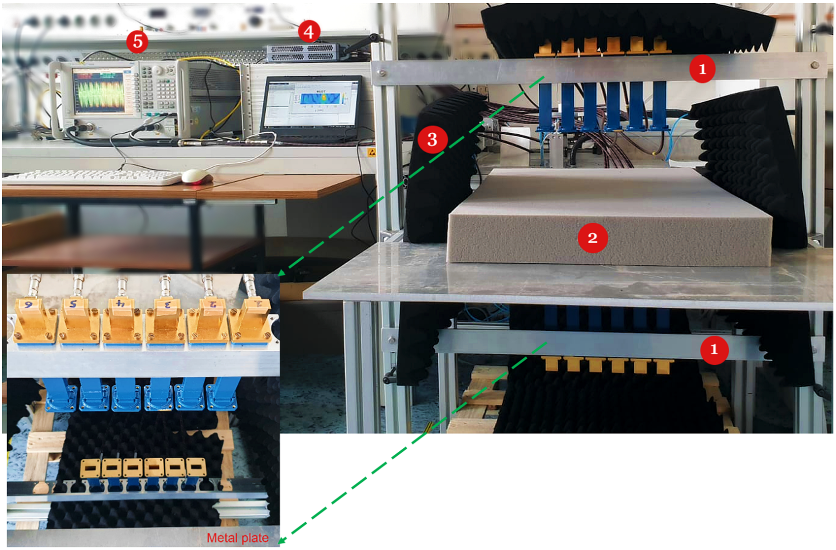

Fig. 3.11: MWT experimental setup. The MWT system consists of X-band open-ended waveguide antennas as sensors. Tag 1. The alignments of the top and bottom antennas are shown in the bottom left by the green arrow, and the portion of the metal plate is removed to enable wave propagation between the top and bottom antennas. The polymer foam is shown by number Tag 2 and surrounded by absorbers, as shown by number Tag 3. The measurement DAQ setup consists of the solid switch and VNA that are denoted by number Tags 4 and 5, respectively. The location plane of the test target is shown in right by white dash lines.

4 Multistatic Uniform Diffraction Tomography & Time-Reversal Microwave Imaging

In this section, the proposed microwave imaging methods, i.e., MUDT and TRI-DORT, are studied numerically and experimentally. In the beginning, the results of the MUDT for the different scenarios are shown and compared with the UDT approach. The element differences between the two approaches are discussed. Later the results of MUDT for media with different layers and different target(s) positions are presented. Then, the performance of the proposed technique under some non-ideal conditions, i.e., when i) if the surface of the media is a random rough and ii) if the inhomogeneities surround the targets are investigated. It is shown how the surface fluctuations can impact the reconstructed images in both imaging algorithms. In the following, the effect of the number of antennas and the number of frequencies on the reconstructed images are investigated.
It is shown when the contrast between two adjacent layers is high, that the MUDT is not be capable of locating the targets in the media, and the results are erroneous. The results of the TR-DORT approach are presented. It is shown that this approach will be capable of correctly locating the targets in the high-contrast media. Finally, experimental results of the TR-DORT method are presented.

4.1 Multistatic Uniform Diffraction Tomography

4.1.1 Numerical setup

To generate the synthetic data from the microwave imaging setup represented in Fig. 3.1, the 3D time-domain solver of the commercial software

CST Studio Suite is used. The data are generated in the X-band (8 GHz-12 GHz) with a frequency step of 5 MHz. The multistatic antenna array, including 7 WR90 antennas is fixed and located on the top of the media. The center-to-center distance between two adjacent elements is 5 cm, and the distance between the antennas to the top of the first layer is 12 cm.
The open boundary condition is chosen to truncate the medium as an infinite free space to simulate the imaging scenario using the 3D CST. It should be mentioned that in the previous chapter, the equations were obtained for the electromagnetic field. However, usually, the S-parameters are measured. Hence, it is necessary to convert the scattering parameters to the electromagnetic field. In this process, two antennas are located in front of each other with the distance of R, and the transmission coefficient S_{21} is stored. Then, using the equation (4.1), the scattered electric fields from the simulation and the experiment are calculated

$$\vec{E}^{sct} = j\omega\mu_0 \frac{S_{ls_{tot}} - S_{lsfree}}{S_{21}} \frac{e^{-jkR}}{4\pi R}, \tag{4.1}$$

$S_{ls_{tot}}$ and $S_{ls_{free}}$ are the measured scattered parameters with and without the target in the medium. The equation (4.1) is derived using the far-field assumption.

4.1.2 Numerical imaging results: three layered media

While recording the scattered field using the multistatic antenna array, it's important to acknowledge the influence of the multilayered media on the received signal. In fact, the signal received from the media often predominates over that from the target. Without mitigating this undesired effect, the reconstructed image may contain not only the target's images but also artifacts from the layered media.
One effective approach to remove the influence of the multilayered media is to acquire scattered field data in the absence of any targets within the media. Subsequently, this received scattered field, encompassing both the media and target contributions, can be subtracted from the received scattered field

originating solely from the media. This technique, known as 'background subtraction,' is applied prior to initiating any image reconstruction processes.

The imaging scenario from a media with three layers is shown in Fig. 4.1. The multistatic array is placed at a distance of 16 cm from the top of the second layer with a thickness of 8 cm. The third layer is a semi-infinite free space. The dielectric constant of the second layer is $\varepsilon_{r,2} = 1.16$, and the dielectric constant of the target is $\varepsilon_r = 2$. The reconstructed image using the UDT approach without applying the background subtraction and eliminating the effect of the multilayered media is shown in Fig. 4.2. As can be seen from this figure, the reflection from the background media is more predominant than the dielectric target inside it, and only the interfaces of the media are reconstructed. This is due to the change in the dielectric constant between the air-dielectric interface and the dielectric-air interface, which creates the scattered EM field. Hence, it is evident that without removing the effect of the background media, the target can not be detected.

Imaging aims to locate the position of the target in the plane after extracting the effect of the background media. From Fig. 4.3 (top), it is expected to see only one peak value in the second layer. As can be seen from Fig. 4.3 (top), strong aliasing effects are observed in UDT as marked by regions 1 and 2. This aliasing effect occurred since the antennas are not positioned in close

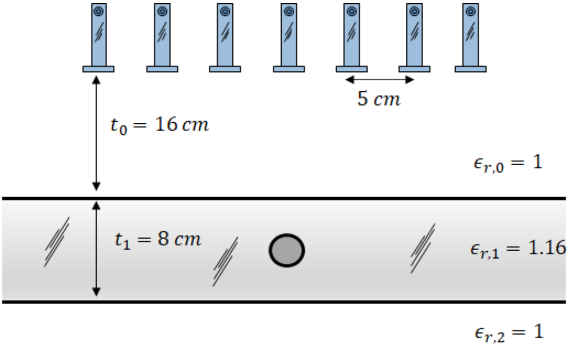

Fig. 4.1: One dielectric target with the dielectric constant of $\varepsilon = 2$ in three layered media. The thickness of the second layer is 8 cm, and the distance of the antenna to the second layer is 16 cm.

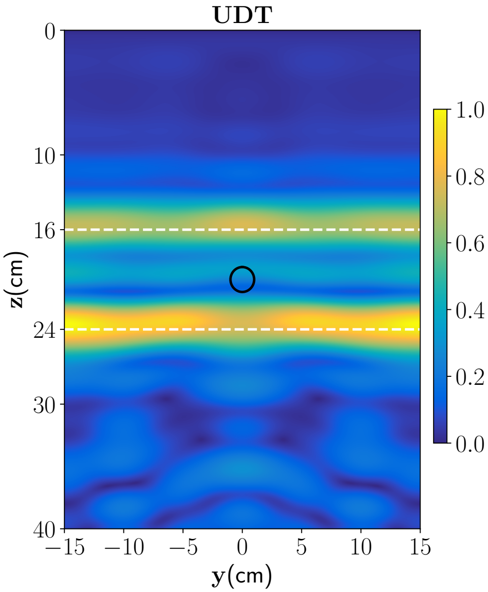

Fig. 4.2: UDT imaging results without extracting the effect of the background media for one dielectric target. The black lines are the location of the target sphere, and the white dashed lines show the background media's interfaces. The color scale is linear and normalized to the peak intensity [125].

vicinity of each other, so the Nyquist criteria could not be met in the UDT approach remember, in Eq. (2.45), the Fourier transform of the received scattered fields was used for the image reconstruction).

To diminish the aliasing effect, one can set the antennas close to each other. In other words, reducing the center-to-center distance between the elements of the array and increasing the number of the antenna is a fixed aperture length. Nonetheless, this might not always be possible due to the array configuration or antenna characteristics. Utilizing the multistatic array compared to the monostatic one addresses this issue more conveniently. Since, in the multistatic case, more of the scattered field is measured which is equivalent to having more spatial sampling points in a fixed aperture length with an equal or less number of antenna. It can be assumed that the Nyquist

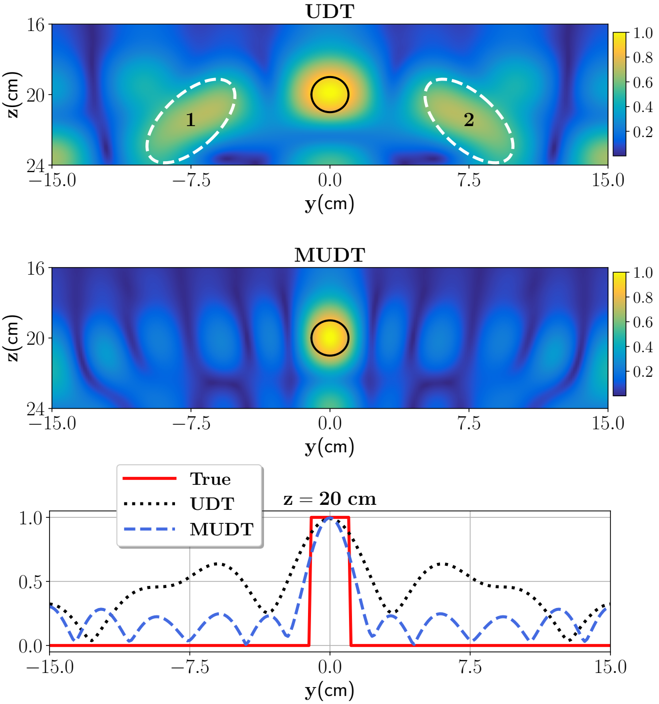

Fig. 4.3: Reconstruction of one dielectric target with UDT (top) and MUDT (middle) where the true location is marked by a black circle. The bottom figure shows the comparison of UDT and MUDT with the true case for the object function values located at -15 cm$\leq y \leq$ 15 cm for z=20 cm [125].

sampling rate criteria are satisfactorily met in this case. As can be seen from Fig. 4.3 (middle), those strong aliasing effects have disappeared, and there is only one peak in the reconstructed image of layer two (as can be clearly seen in Fig. 4.3(bottom)). It has to be mentioned that a slight artifact can be seen between the target and the bottom interface of the dielectric layer. The artifact is due to the multiple scattering between the target and the bottom interface. This multiple scattering has been ignored during the formulation of the problem since the Born approximation is employed. However, taking into account the multiple scattering would make the formulation complex.

A closed form of the objective function cannot be achieved accordingly.

The consequences of the multistatic case rather than the monostatic one can be seen better in the subsequent scenarios. Scenarios where two and three targets exist in the second layer, respectively, are considered. The location of the targets is shown in Fig. 4.5 (left) and Fig. 4.5 (right), respectively. The dielectric constant of the second layer is the same as in the previous case. The targets are located at (0 cm, 20 cm, 0 cm), (0 cm, 20 cm, 10 cm) for two target scenarios. For the three targets scenario, the position of the targets is the same as before, and the position of the third target is (0 cm, 19 cm, 12 cm). The other parameters are the same as in the previous case. In both cases, since there is multiple scattering between the targets, the scattered fields propagate in different directions. In the monostatic case, the antenna array is not able to distinguish these scattered fields from each other. It leads to the displacement and distortion of the reconstructed image. Reconstructed images with the UDT approach are illustrated in Fig. 4.5 (top) and Fig. 4.6 (top) for two and three target scenarios, respectively. It can be easily seen, that the location of the targets is shifted, and the UDT approach, when the number of targets increases, will not be able to reconstruct the position of the targets at all. However, in the MUDT approach, the scattered fields are more discernible. The antenna array would be able to recognize each target separately. Fig. 4.5 (middle) and Fig. 4.6 (middle) represent this effect. Further, the object function at z=0 cm for UDT and MUDT are plotted in Fig. 4.5 (bottom) and Fig. 4.6 (bottom) reconstruction differences

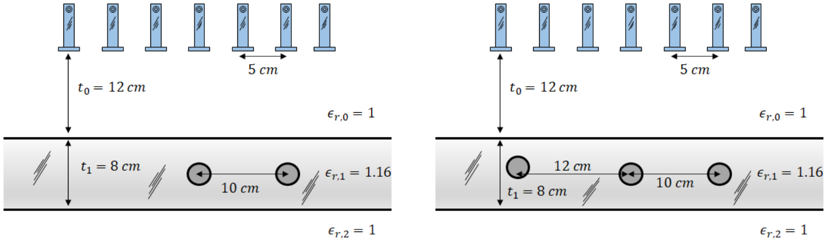

Fig. 4.4: (Left) Two, and (Right) Three dielectric targets with the dielectric constant of $\varepsilon_{r,1} = 2$ in three layered media. The thickness of the second layer is 8 cm, and the distance of the antenna to the second layer is 16 cm.

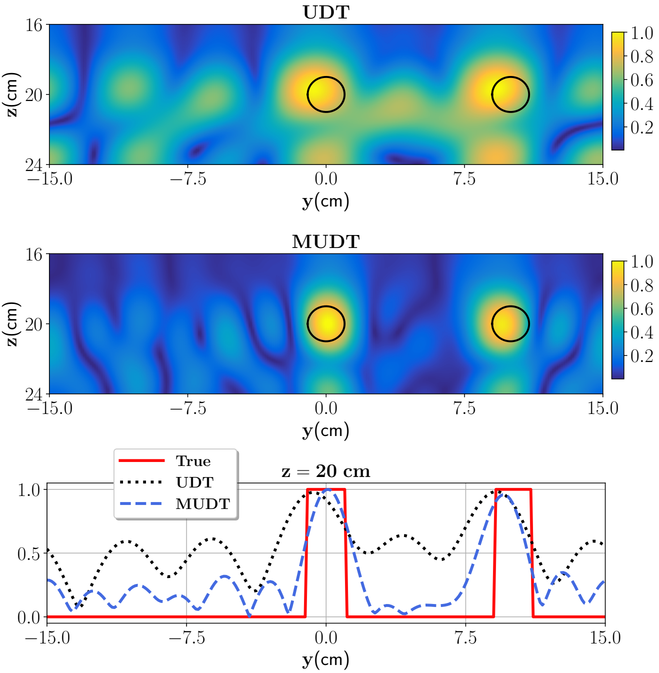

Fig. 4.5: Reconstruction of two targets with UDT (top) and MUDT (middle). The bottom figure shows the comparison of UDT and MUDT with the true case for the object function values located at -15 cm$\leq y \leq$ 15 cm for (left) z=0 cm.

can be better observed.

To quantitatively evaluate the accuracy of the reconstruction, the true and the reconstructed normalized object function by using root mean square error (RMSE) and resemblance coefficient (RC) performance metrics is compared. The RC parameter is calculated using (4.2) where $\overline{O^{\text{Rec}}} = O^{\text{Rec}} - \langle O^{\text{Rec}} \rangle$, and $\overline{O^{\text{True}}} = O^{\text{True}} - \langle O^{\text{True}} \rangle$. Where O^{Rec} is the reconstructed profile, $\langle O^{\text{Rec}} \rangle$ is

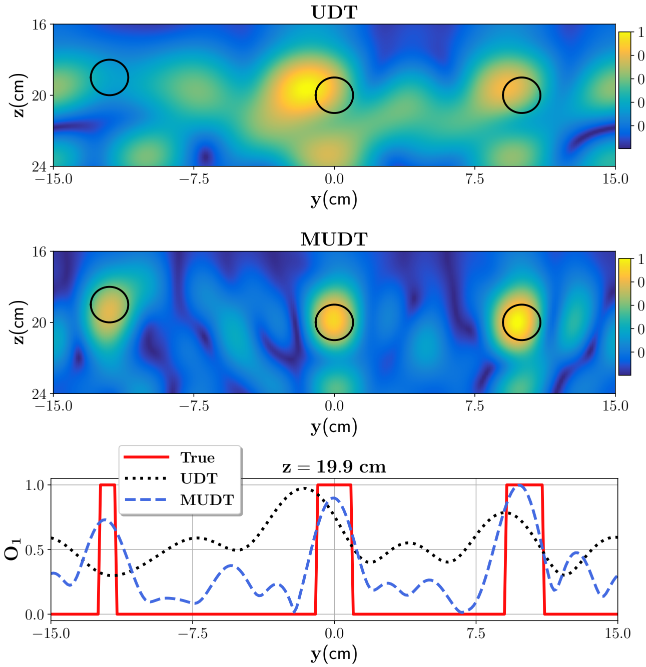

Fig. 4.6: Reconstruction of three targets with UDT (top) and MUDT (middle). The bottom figure shows the comparison of UDT and MUDT with the true case for the object function values located at -15 cm$\leq y \leq$ 15 cm for z=19.9 cm.

the average value of O^{Rec}, O^{True} is the true profile of the media, and $\langle O^{\text{True}} \rangle$ is the average value of the true profile.

$$\text{RC}_O = \frac{\displaystyle\int\!\!\int_{\Omega_{\text{foam}}} \overline{O^{\text{Rec}}}\;\overline{O^{\text{True}}} dydz}{\sqrt{\displaystyle\int\!\!\int_{\Omega_{\text{foam}}} (\overline{O^{\text{Rec}}})^2 dydz}\sqrt{\displaystyle\int\!\!\int_{\Omega_{\text{foam}}} (\overline{O^{\text{True}}})^2 dydz}}. \tag{4.2}$$

$\langle\cdot\rangle$ is the mean operator. For the RC, its values vary between 0 and 100 %. As it gets closer to 100 %, the reconstructed image is closer to the actual one. The RC and RMSE are calculated separately for the UDT and MUDT

Table 4.1: Comparison between UDT and MUDT algorithm.

Number of Targets	One		Two		Three	
Method	UDT	MUDT	UDT	MUDT	UDT	MUDT
RMSE (%)	35.45	18.7	41.62	22.97	43.45	27.55
RC (%)	35.2	56.27	35	57.25	14.83	51.49

imaging algorithms. As can be seen from Table 4.14, the performance of the MUDT is clearly better than for UDT. The performance of the UDT by increasing the number of targets varies and decreases significantly. However, the MUDT imaging algorithm almost represents a consistent and satisfactory performance.

4.1.3 Experimental results: three layered media

In the first experiment, a moisture wet-spot is inserted in the polymer foam. To create the wet-spot moisture target, a spherical foam of diameter of 2.5 ± 0.1 cm and with 36 % wet-basis moisture level ($\varepsilon_r \approx 1.87 - j0.12$) is chosen. An approximate location of the target inside the foam is centered at (x=0 cm, y=-3.5 cm, z=14.6 cm). Then, the background subtraction is applied to extract the scattered field inside the polymer foam. The effect of the background media is removed. It should be mentioned, in the experimental scenario, the array is placed at 12 cm from the top of the second layer to increase the SNR without losing the generality of the method. The reconstruction based on UDT is depicted in Fig. 4.7 (top). As supported by the theoretical studies and simulation, in this case, the location of the target is reconstructed, but, a strong aliasing effect is observed. However, MUDT correctly reconstructs the position and provides a negligible shadow image in Fig. 4.7 (bottom). Even though using the MUDT, in addition to eliminating the aliasing effect, the spatial resolution is also increased.

In the second experiment, two PTFE Teflon spheres with a radius of 1.2 cm and dielectric constant $\varepsilon_{r,\mathrm{Tef}} = 2.1$ are used as the test targets. Both are placed inside the foam with their centers located at (x=0 cm, y=-2 cm, z=15.8 cm) and, (x=0 cm, y=-8 cm, z=15.8 cm). Background subtraction is

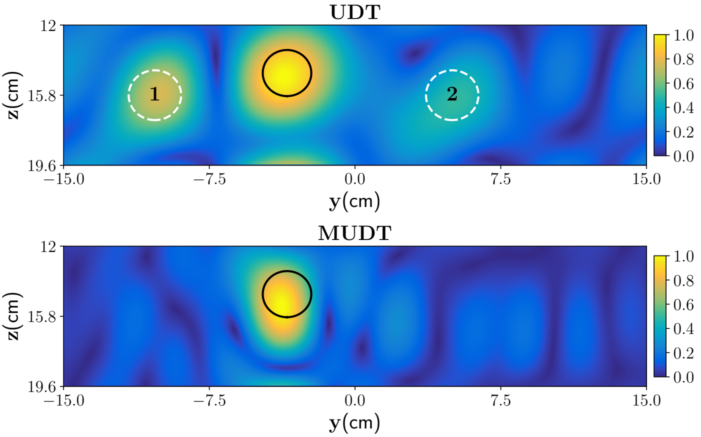

Fig. 4.7: Reconstruction of one dielectric target with UDT (top) and MUDT (bottom). Two aliasing effects are marked by regions 1 and 2.

Table 4.2: Comparison between UDT and MUDT algorithm.

Number of Targets	One		Two	
Method	UDT	MUDT	UDT	MUDT
RMSE (%)	32.71	19.83	44.9	28.91
RC (%)	34.91	50.6	3.86	56

applied to extract the scattering field due to the scatterer inside the polymer foam. The reconstruction based on UDT is depicted in Fig. 4.8 (top). The expected aliasing effect and a heavy distortion are observed, and UDT fails to reconstruct the targets in the imaging domain. However, MUDT correctly reconstructs the position and provides a negligible shadow image in Fig. 4.8 (bottom). As can be observed, using the MUDT, the estimated position, and shape of the targets are close to the true case, and different targets are resolved.

Separate calculations for the RC and RMSE are performed on both the UDT and MUDT imaging algorithms. Table 4.2 indicates that the MUDT outperforms the UDT, with a clear advantage in performance. The effectiveness of

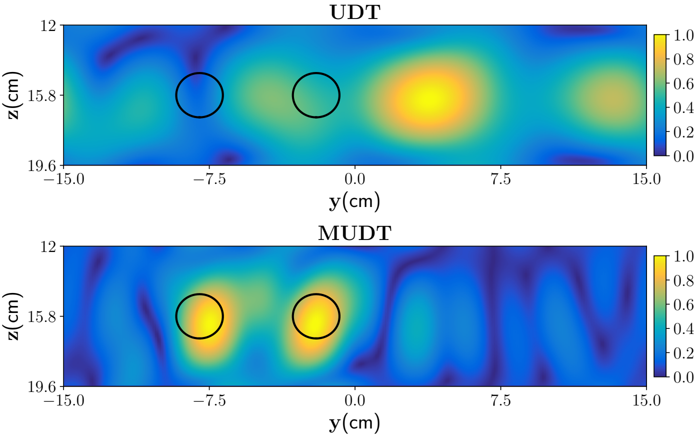

Fig. 4.8: Reconstruction of two dielectric targets with UDT (top) and MUDT (bottom). The true location of the targets is shown with a black circle.

the UDT varies and becomes notably compromised with an increasing number of targets. In contrast, the MUDT consistently demonstrates satisfactory performance in the imaging algorithm.

4.1.4 Numerical imaging results: four and five layered media

In some applications, the number of layers might be higher than four or five. Here, microwave imaging using the MUDT approach for four and five layers media and comparing the results with the UDT approach is investigated. Figure 4.9 shows a setup with four layers assuming relative dielectric constants of $\varepsilon_{r,2} = 1.16, \varepsilon_{r,3} = 2.1$. The dielectric layers have thicknesses of 8 cm, 1 cm along the z-axis respectively. The diameter of the two targets is 1 cm, and the center-to-center distance is 7.5 cm.

The imaging results based on UDT are presented in Fig. 4.10 (left). White dash lines are the locations of the interfaces, and black dash circles are the true locations of targets. As predicted in the last section, the UDT method will lead to a strong aliasing effect. In this case, in addition to an aliasing effect in layer 3, another aliasing effect in layer 4 can be observed. It should be noted in comparison to the three layers case when two targets had been located inside the second layer, an additional reflection from the bottom dielectric layer decreases the performance of the UDT method. As it has been assumed, there is no reflected electromagnetic field from the bottom layer. However, compared to Fig. 4.10 (right), the target location is accurately reconstructed using the MUDT algorithm. There is no aliasing effect in any dielectric layers as well as any distortion or displacement. However, as stated before, due to the multiple reflections between the targets and the bottom interface (layer 3 and layer 4), two artifacts in layer 4 can be observed.

In the next scenario, as shown in Fig. 4.11, a five layers layered media with relative dielectric constants $\varepsilon_{r,2} = 1.16$, $\varepsilon_{r,3} = 2.1$, $\varepsilon_{r,4} = 1$ is assumed. The dielectric layers have thicknesses of 8 cm, 2 cm, 3 cm along the z-axis respectively. The diameter of the two targets is 1 cm, and the center-to-center distance is 10 cm.

The imaging result based on UDT is presented in Fig. 4.12 (left). White dash lines are the locations of interfaces, and black dash circles are the true

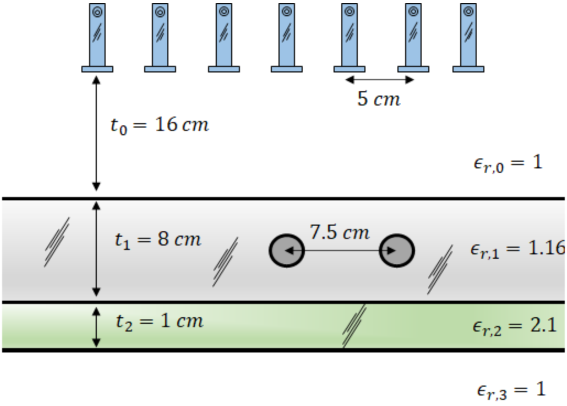

Fig. 4.9: Two dielectric targets with the center to center distance of 7.5 cm, and the dielectric constant of $\varepsilon_r = 2$ in four layered media. The thickness of layer 2 and layer 3 are 8 cm, and 1 cm, respectively. The distance of the antenna to layer 2 is 16 cm.

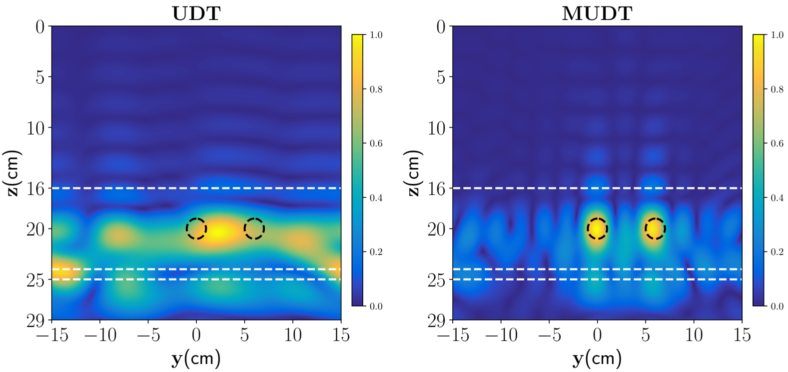

Fig. 4.10: Reconstruction of two dielectric targets with UDT (left) and MUDT (right) for the four layered media. The interfaces are marked with white dashed lines.

locations of targets. The UDT method will lead to an aliasing effect. One aliasing effect can be seen on the left, and the other aliasing effect is on the right side of Fig. 4.12. As can be seen from Fig. 4.12, the reconstructed image of the targets is stretched along the y-direction. In other words, the center of the two targets is 1 cm shifted to the left. As shown in Fig. 4.12 (right), there is no aliasing effect in any dielectric layers as well as any distortion or displacement. Moreover, both targets have not stretched, and only a slight shift to the left can be observed for the right target.

In the next scenario, as shown in Fig. 4.13, two dielectric targets are located at the interfaces. One dielectric target with a diameter of 1 cm is located at the interface 2 and the other dielectric target with a diameter of 1 cm is positioned at the interface 3. It implies that a part of the target is placed in one layer, and the remaining part is placed in the other layer. The relative dielectric constants are $\varepsilon_{r,2} = 1.16, \varepsilon_{r,3} = 2.1$, and the dielectric layers have thicknesses of 8 cm, 2 cm along z-axis respectively.

Fig. 4.14 (left) shows the imaging results obtained using UDT. The white dashed lines indicate the locations of interfaces, and the black dashed circles represent the true locations of targets. The reconstructed image using UDT reveals that the target placed at the 2^{th} interface is split into two different targets, one in layer 2 and another in layer 4. Additionally, the location

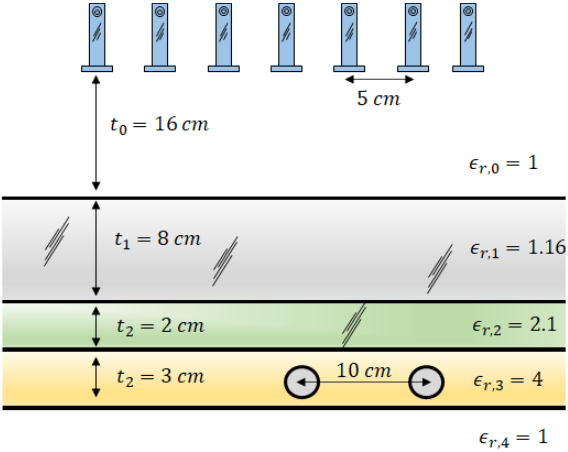

Fig. 4.11: Two dielectric targets with the center to center distance of 10 cm, and the dielectric constant of $\varepsilon_r = 2$ in five layered media. The thickness of layer 2, layer 3, and layer 4 are 8 cm, 2 cm, 3 cm respectively. The distance of the antenna to the second layer is 16 cm.

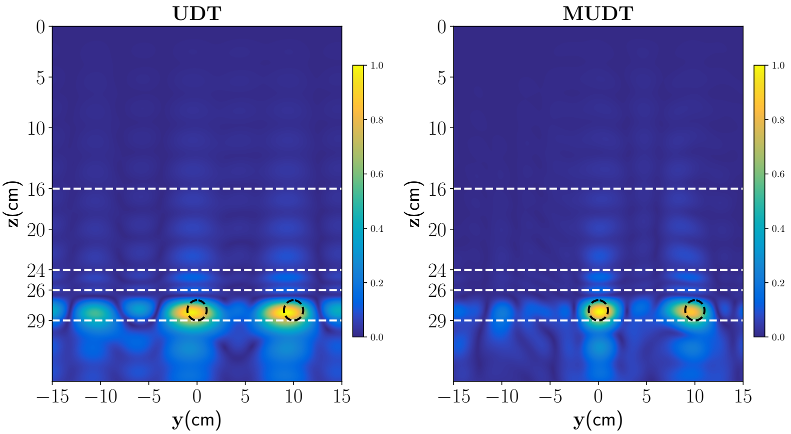

Fig. 4.12: Reconstruction of two dielectric targets with UDT (left) and MUDT (right) for the five layered media. The interfaces are marked with white dashed lines.

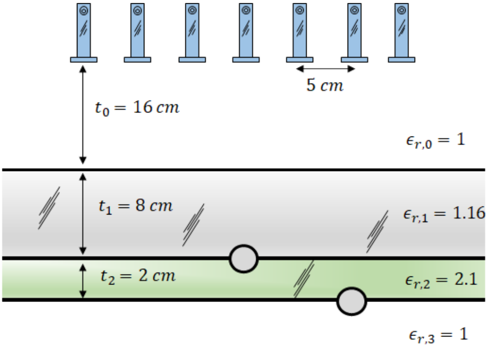

Fig. 4.13: Two dielectric targets with the dielectric constant of $\varepsilon_r = 2$ are positioned at the second and third interfaces. The thickness of the second and third layers are 8 cm, 2 cm, respectively. The distance of the antenna to the second layer is 16 cm.

Table 4.3: Comparison between UDT and MUDT algorithm.

Scenario	4 Layers		5 Layers		4 Layers in Boundary	
Method	UDT	MUDT	UDT	MUDT	UDT	MUDT
RMSE (%)	35.45	18.7	11.78	8.41	17.49	10.16
RC (%)	35.2	0.5627	37.45	49.15	26.78	44.56

of the other target at interface 3 is not accurately reconstructed, showing mainly a target in layer 3. A stretch in the shape of the targets is also visible. In contrast, Fig. 4.14 (right) shows that the MUDT algorithm accurately reconstructs the location of the target while maintaining a smooth and continuous reconstructed image. It is important to note that while UDT was developed to address the amplitude discontinuity at the interfaces of adjacent layers using DT. It cannot reconstruct the position of embedded targets at boundaries if there are inadequate antennas in a fixed aperture length. This issue is resolved by applying the MUDT algorithm.

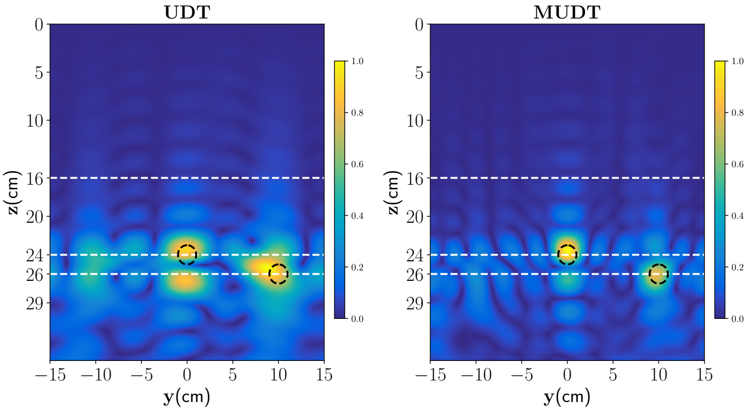

Fig. 4.14: Reconstruction of two dielectric targets with UDT (left) and MUDT (right) for the five layered media when targets are located at the interfaces of two adjacent layers. The interfaces are marked with white dashed lines.

4.1.5 Experimental results: four layered media

To show the performance of the UDT and MUDT imaging algorithms in layered media, a PTFE dielectric slab with a thickness of 1 cm is placed under the polymer foam. A PTFE dielectric slab with a diameter of 2.4 cm is positioned at (0 cm, 2 cm, 16 cm) and inside the layer 2.
Reconstructed images using UDT and MUDT are depicted in Fig. 4.15. In this case, UDT represents completely erroneous images as shown in Fig. 4.15 (Left). As can be seen in the reconstructed image, where two additional areas are visible, as indicated by white circle dash lines. Those areas are a consequence of the aliasing effect, which is expected due to the failure to meet the Nyquist criteria in the UDT algorithm. However, the MUDT algorithm addresses this issue, as shown in Fig. 4.15 (right), where the location of the dielectric target is accurately reconstructed, and an aliasing-free image is obtained. It is worth noting that the presence of the dielectric slab under layer 2 increases the aliasing effect compared to the three layer scenario without a dielectric slab (See Fig. 4.7). This is due to the scattered field of the dielectric slab, which negatively impacts the performance of

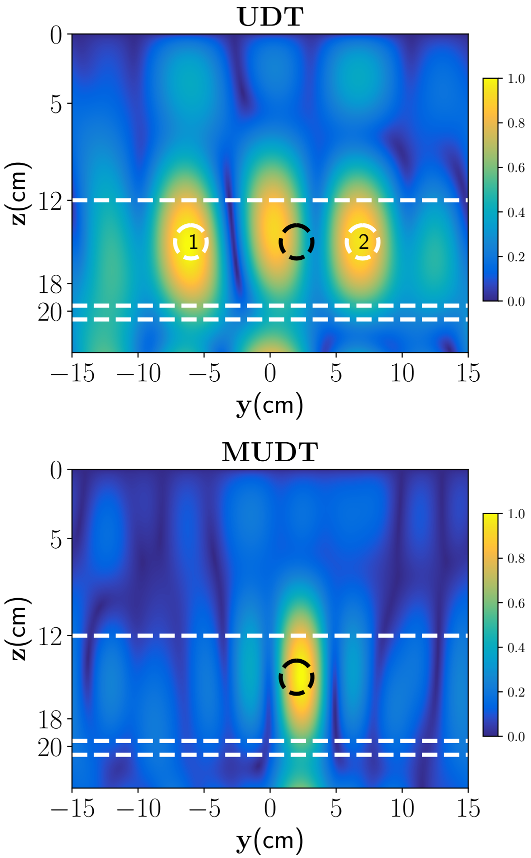

Fig. 4.15: Reconstruction of two dielectric targets with UDT (top) and MUDT (bottom) for the four layered media. The interfaces are marked with white dashed lines.

the UDT algorithm. Table 4.4 includes the RC and RMSE values, which reveal that the UDT is affected by a severe aliasing effect, resulting in low RC and higher RMSE values.

Table 4.4: Comparison between UDT and MUDT algorithm.

Scenario	4 Layers, Experiment	
Method	UDT	MUDT
RMSE (%)	39.4	20
RC (%)	6.41	41.95

4.2 Random Rough Surfaces

So far, the multilayered media with a planar surface is considered for target detection. However, it can be observed in many practical applications like GPR and TWRI that the multilayer media can also have some fluctuation on the surface. In order to investigate the performance of the MUDT when the surface contains some roughness, a media with a randomly rough surface at the top interface is considered and modeled according to [126]

$$z(y) = \sum_{m=-M}^{M} m^{-\beta} \mathcal{G}_m \cos\left(2\pi m y + U_m\right) \tag{4.3}$$

Here, m is the integer number representing the spatial frequency and β denotes the spectral exponent, $\mathcal{G}_m$ is sampled as $\mathcal{G}_m \sim \mathcal{N}(\mu, \sigma)$ with mean μ and standard deviation σ, and $U_m \sim \mathcal{U}(0, 2\pi)$ is sampled as $U_m \sim \mathcal{U}(0, 2\pi)$. The terms $\mathcal{N}$, $\mathcal{U}$ denote Gaussian and uniform distribution, respectively.

In Fig. 4.16, for one sample frequency, i.e., 8 GHz the real and imaginary parts of the electric field of FEM of COMSOL and asymptotic fields (calculated using SPA) are compared [91] for a three layer dielectric media with two different degrees of roughness. It's important to clarify that the term "asymptotic" denotes the electric field of a random rough surface medium, with the calculation not taking its roughness into account. Here, the asymptotic fields of the three layer media with the rough surface for the first interface are estimated using the SPA under the assumption of $\sigma = 0$ and $\beta = 0$. It is observed that under the amplitude of a moderate random rough surface, the scattered fields received by the antennas slightly change if compared to the normal scenarios when the root mean square height $= 0$. Hence, the average distance from each antenna to the top surface of

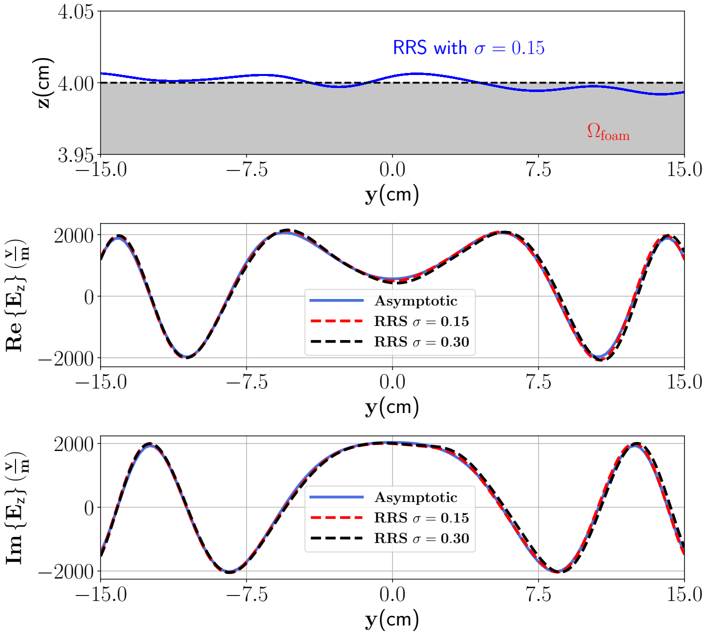

Fig. 4.16: Top figure shows the top surface of the foam with considered roughness and its mean height. Asymptotic real (middle) and imaginary (bottom) of the electric fields compared with the FEM results of a rough surface with an σ of 0.15 and 0.3.

the foam is considered, i.e, $h = \langle h_i \rangle$, $i = 1, 2, \cdots N$, where $\langle \cdot \rangle$ is the mean operator. Based on this, the Green's function of the multilayered media with a smooth interface might be approximated as Green's function of the multilayered media with a fluctuating interface.

To evaluate the performance of the MUDT, a target with a dielectric constant of $\varepsilon = (1.69 - j0.1)$ and radius of 1 cm at the position (0 cm, 0 cm) is considered inside the foam with a dielectric constant of $1.16 - j0.01$ and a moderately rough surface with the following parameters: $\mu = 0$, $\sigma = 0.15$, and $\beta = 0.8$. The reconstructed image using the MUDT algorithm is depicted in Fig. 4.17. As can be seen, the position of the target is visible. But, compared to the multilayer with a smooth surface, the shadow images are

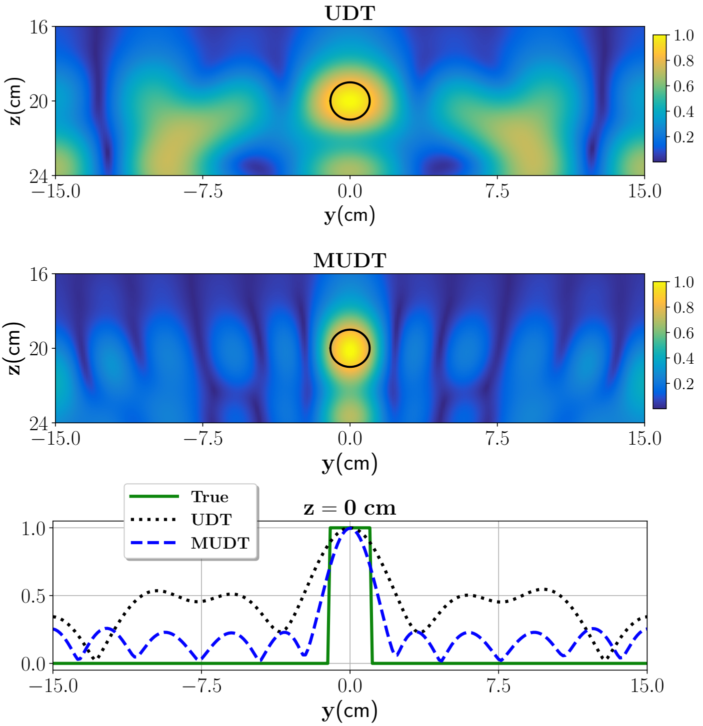

Fig. 4.17: Reconstruction of one wet-spot moisture case with UDT (top) and MUDT (middle) for the random rough surface with $\mu = 0$, $\sigma = 0.15$, and $\beta = 0.8$. The bottom figure shows the comparison of UDT and MUDT with the true case for the object function values located at -15 cm$\leq y \leq$15 cm for z=0 cm.

more prominent. This is due to the multiple scattering between the rough surface and the bottom of the layer that is not taken into account by Green's function. Furthermore, with increasing the roughness of the top interface, the electromagnetic fields inside the layer can not be fully estimated by the current asymptotic expression. It can lead to more strong shadow images in the reconstruction.

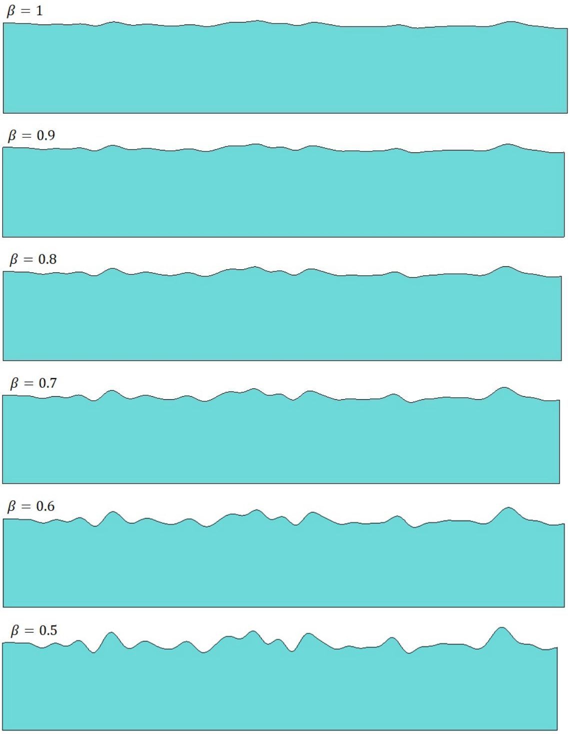

Fig. 4.18: The layered media with various degrees of roughness.

4.2.1 Effect of the roughness

In order to determine the impact of the roughness in the reconstructed image, the roughness has been gradually increased by changing the parameter β. By reducing this parameter, the roughness of the media will vary and increase. The surfaces with various degrees of roughness can be seen in Fig. 4.18. As can be observed, by decreasing the parameter β, more fluctuations around the interface exist. The fl_{max} is defined as the maximum fluctuations of the interface for further analyses. The value of fl_{max} as a ratio of the center wavelength for different beta is shown in Table 3.3.

Table 4.5: fl_{max} value as a ratio of center wavelength.

	$\beta = 1$	$\beta = 0.9$	$\beta = 0.8$	$\beta = 0.7$	$\beta = 0.6$	$\beta = 0.5$
$\frac{fl_{max}}{\lambda_c}$	0.1	0.13	0.2	0.27	0.37	0.5

Table 4.6: RMSE error values for for different fl_{max} in Fig. 4.19

	$\beta = 1$	$\beta = 0.9$	$\beta = 0.8$	$\beta = 0.7$	$\beta = 0.6$	$\beta = 0.5$
UDT	31.79	33	33.42	34.03	34.9	35.86
MUDT	17.02	17.48	17.61	17.83	18.14	18.5

Consider a random rough surface medium as shown in 4.18. The dielectric constant of the medium is 1.16, and the antenna array is positioned at 12 cm from the top interface. One dielectric target with a radius of 1 cm and a dielectric constant of 2.5 is located at the center of the medium, i.e, (0 cm, 0 cm). Reconstructed images using MUDT and UDT algorithms are depicted in the left and right columns of Fig. 4.19, respectively. From the left column, it can be understood by increasing the roughness of the medium, MUDT truly reconstructs the location of the target. However, in reconstructed images using UDT, a strong aliasing effect can be seen in all cases. Furthermore, another aliasing effect at the corners starts appearing when $fl_{max} = 0.13\lambda_c$ and becomes more seeable when the roughness increases. To demonstrate this effect, RMSE values and correlation values for both MUDT and UDT are provided in tables 4.6 and 4.7, respectively.

The RMSE value and the correlation parameter for the different scenarios are calculated and shown in Table 4.6 and 4.7, respectively. By increasing the aliasing effect, the RMSE values increase accordingly, and the correlation between the reconstructed image using UDT and the real scenario decreases gradually. These two parameters have the same behavior with the slower slope in the MUDT algorithms due to the slight increase of the shadow images. It can be concluded that when the dielectric constant of the media is small, the interface fluctuations do not lead to a significant effect on the reconstructed images by the MUDT algorithm.

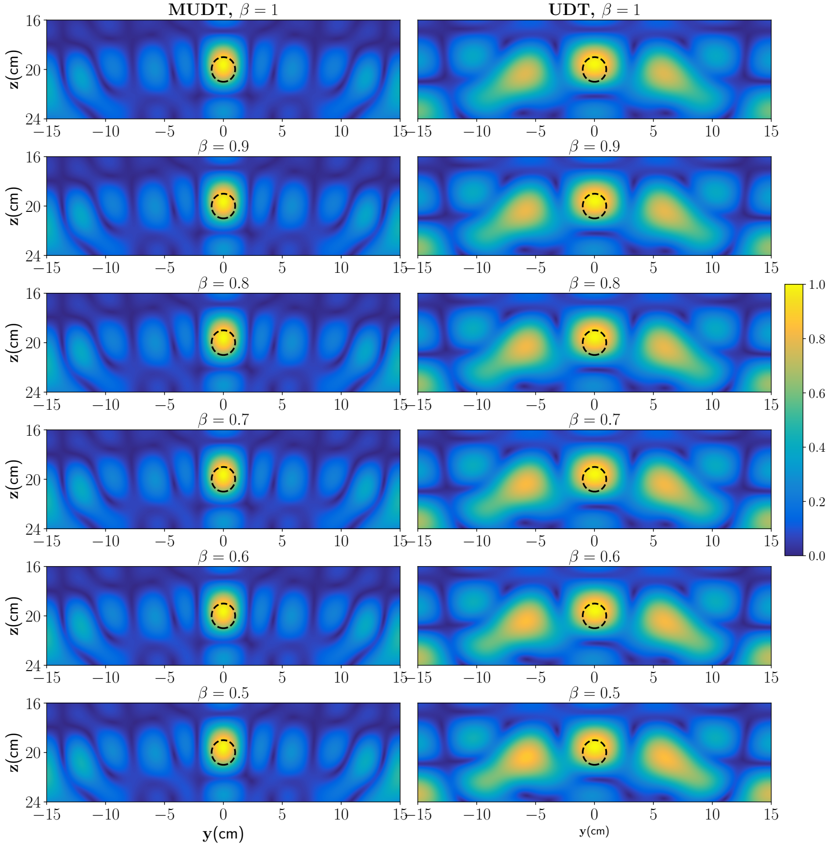

Fig. 4.19: Reconstruction of one dielectric target in a three layered media with various degrees of the roughness of the top interface with MUDT (left) and UDT (right). The dielectric constant of the background layer is $\varepsilon_{r,1} = 1.16$, and the dielectric constant of the target is $\varepsilon_r = 2$.

Table 4.7: RC values for for different fl_{max} in Fig. 4.19

	$\beta = 1$	$\beta = 0.9$	$\beta = 0.8$	$\beta = 0.7$	$\beta = 0.6$	$\beta = 0.5$
UDT	36.43	35.06	34.57	33.78	32.81	31.72
MUDT	59.35	58.4	58.16	57.75	57.02	56.31

Table 4.8: RMSE error values for compared analytical model and FEM in Fig. 4.20.

	$\beta = 1$	$\beta = 0.9$	$\beta = 0.8$	$\beta = 0.7$	$\beta = 0.6$	$\beta = 0.5$
UDT	33.19	34.5	33.69	33.5	33.18	34.86
MUDT	17.15	17.8	18.81	20.52	22.96	28.14

Table 4.9: RC values for for different fl_{max} in Fig. 4.20.

	$\beta = 1$	$\beta = 0.9$	$\beta = 0.8$	$\beta = 0.7$	$\beta = 0.6$	$\beta = 0.5$
UDT	30.88	29.61	25.59	20.32	12.32	6
MUDT	56	54.21	51.9	47.59	42.2	33.12

4.2.2 Increasing the dielectric constant of the media

In the next set of scenarios, the dielectric constant of the random rough surface dielectric layer has been increased to $\varepsilon = 2$. The other parameters are identical to the previous scenario.

Reconstructed images using the MUDT are presented in Fig. 4.20, left columns. The location of the targets in all scenarios is truly obtained. However, a light shadow image between the target and bottom interface is visible compared to the previous scenario. Next, by increasing the roughness, almost moderate shadow images initiate appearing, especially when the fluctuations are greater than $fl_{max} = 0.37\lambda_c$. However, reconstructed images utilizing the UDT algorithm are diminished compared to the previous scenario shown in Fig. 4.20. In this case, even when the $fl_{max} = 0.1\lambda_c$ (which means the interface almost has no fluctuation), the correlation is lower than the $fl_{max} = 0.5\lambda_c$ in Fig. 4.19. This implies that by increasing the dielectric constant of the background medium, the imaging algorithm becomes more sensitive to the fluctuation of the interface. With further increasing fluctuation, the reconstruction with the UDT fails to estimate the location of the target, and the results will be erroneous.

Analogous to the previous scenario, the RMS error, and RC of the reconstructed images are represented in Tables 4.8 and 4.9, respectively. As it can be perceived from table 4.8, by increasing the roughness, the RMS error increases as well. However, when fl_{max} exceeds $0.37\lambda_c$, the UDT fails,

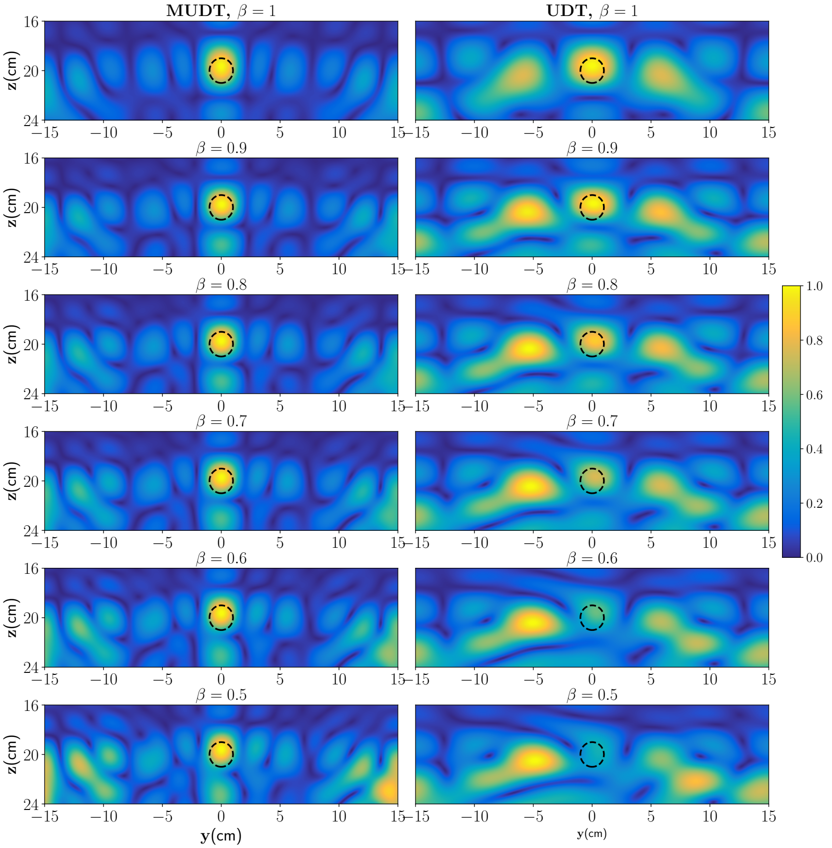

Fig. 4.20: Reconstruction of one dielectric target in three layered media with various degrees of the roughness of the top interface with MUDT (left) and UDT (right). The dielectric constant of the background layer is $\varepsilon_{r,1} = 2$, and the dielectric constant of the target is $\varepsilon_r = 1.7$.

and the RMS error is not showing any relevant number. The RC represents lower values for almost all cases compared to the previous scenario, as shown in table 4.9. For example, a medium with a dielectric constant of 1.16 and $fl_{max} = 0.5\lambda_c$ has a bigger RC than a medium with a dielectric constant of 2 and $fl_{max} = 0.1\lambda_c$ which clearly indicate the impact of the dielectric constant of the background medium to the reconstructed images under roughness condition.
It can be concluded if one interface possesses roughness and the other one is smooth, the MUDT algorithm is capable of finding the position of the target(s). However, it should be noted if the roughness increases, shadow images emerge and become dominant in UDT-reconstructed images, leading to erroneous reconstructed images.

4.2.3 Multilayer random rough-surface media

In the next set of scenarios, in addition to the top interface, the bottom interface is also a random rough surface. Reconstructed images using the MUDT are presented in Fig. 4.21, left columns. The location of the targets in all scenarios is truly obtained. However, compared to the previous scenario, a light shadow image between the target and bottom interface is visible. Next, by increasing the roughness, almost moderate shadow images appear, especially when the fluctuations are greater than $fl_{max} = 0.37\lambda_c$. However, reconstructed images utilizing the UDT algorithm are diminished compared to the previous scenario shown in Fig. 4.20. In this case, even when the $fl_{max} = 0.1\lambda_c$ (which means the interface almost has no fluctuation), the correlation is lower than the $fl_{max} = 0.5\lambda_c$ in Fig. 4.19. This implies by increasing the dielectric constant of the background medium, the imaging algorithm becomes more sensitive to the fluctuation of the interface. With further increasing fluctuation, the reconstruction with the UDT fails to estimate the location of the target, and the results will be erroneous.
The RMS error and RC of the reconstructed images are represented in Tables 4.10 and 4.11, respectively. As it can be perceived from Table 4.10, by increasing the roughness, RMS error increases as well. However, when fl_{max}

Table 4.10: RMSE error values for compared analytical model and FEM in Fig. 4.21.

	$\beta = 1$	$\beta = 0.9$	$\beta = 0.8$	$\beta = 0.7$	$\beta = 0.6$	$\beta = 0.5$
UDT	32.51	34.64	34.31	32.99	35.29	35.19
MUDT	17.6	18.32	18.91	20.24	23.02	28.36

Table 4.11: RC values for for different fl_{max} in Fig. 4.21.

	$\beta = 1$	$\beta = 0.9$	$\beta = 0.8$	$\beta = 0.7$	$\beta = 0.6$	$\beta = 0.5$
UDT	32.47	29.75	27.25	22.7	14.11	4.75
MUDT	54.73	53.17	51.65	48.41	41.76	31.91

exceeds $0.37\lambda_c$, the UDT fails, and the RMS error is not showing any relevant number. The RC represents lower values for almost all cases compared to the previous scenario, as shown in Table 4.11. It can be concluded if two interfaces possess roughness, the MUDT algorithm is capable of finding the position of the target(s). However, it should be noted as roughness increases, shadow images emerges and become dominant in UDT-reconstructed images, and leads to erroneous reconstructed images.

4.3 Random Media

Consider a background media where the dielectric constant distribution of the medium is not constant and has random values. In other words, target(s) are surrounded by inhomogeneities, and the dielectric constant of the layer can be expressed as $\varepsilon_r(\vec{r}) = \varepsilon_{\mathrm{r,n}} + \varepsilon_{\mathrm{r,f}}(\vec{r})$ where $\varepsilon_{\mathrm{r,f}}$ is the randomly fluctuating part of the dielectric constant and $\varepsilon_{\mathrm{r,n}}$ denotes the mean dielectric constant such that the ensemble average $\langle \varepsilon_r(\vec{r}) \rangle = \varepsilon_{\mathrm{r,n}}$, and $\vec{r} = y\hat{y} + z\hat{z}$ is the spatial position. It should be noted that $\hat{y}$ and $\hat{z}$ are unit vectors in Cartesian coordinates. Here, it's assumed the average dielectric constant of the polymer foam is known. It might be assumed that the fluctuating inhomogeneities

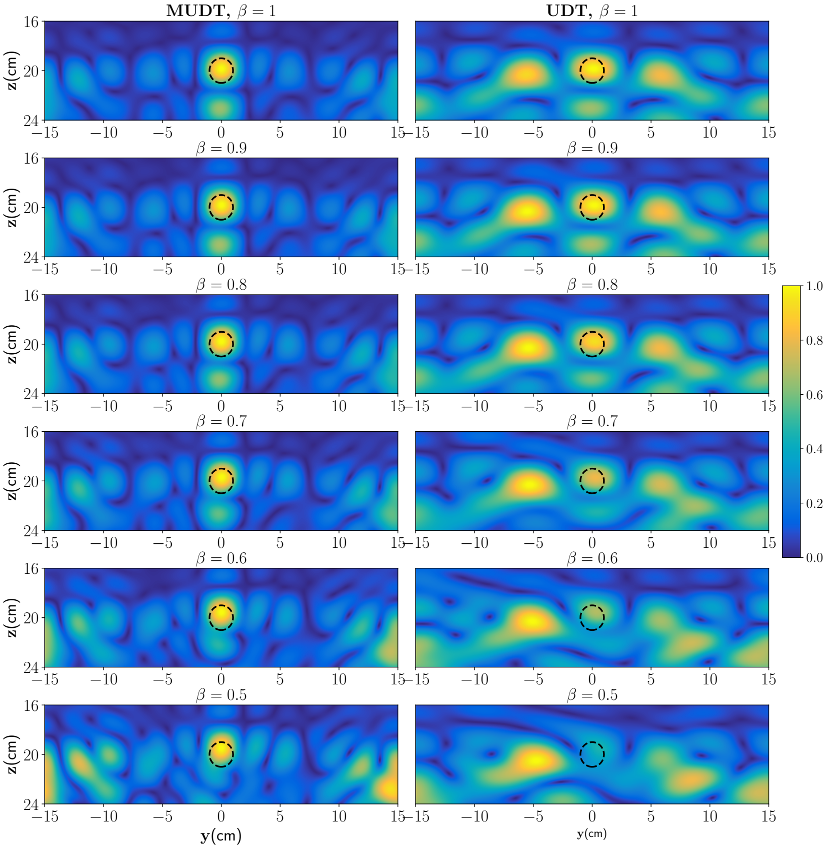

Fig. 4.21: Reconstruction of one dielectric target in a three layered media with various degrees of the roughness of the top and bottom interfaces with MUDT (left) and UDT (right). The dielectric constant of the background layer is $\varepsilon_{r,1} = 2$, and the dielectric constant of the target is $\varepsilon_r = 1.7$.

have a zero-mean Gaussian random variable with a Gaussian correlation function given by [89, 127]

$$C(\vec{r}_1, \vec{r}_2) = \exp\left(- \frac{||y_1 - y_2||^2}{l_y^2} - \frac{||z_1 - z_2||^2}{l_z^2} \right) \tag{4.4}$$

where l_y and l_z are the characteristic lengths, and $\vec{r}_1 = (y_1, z_1)$ and $\vec{r}_2 = (y_2, z_2)$. In this case, the deterministic form of the Green's function is not known. However, for the thin random medium, the Green's function can be expressed as follows [128]

$$\langle \bar{\bar{G}}(\vec{r}, \vec{r}_t) \rangle = \bar{\bar{G}}^{(0)}(\vec{r}, \vec{r}_t) + \Delta^2 \langle \bar{\bar{G}}^{(2)}(\vec{r}, \vec{r}_t) \rangle + \Delta^4 \langle \bar{\bar{G}}^{(4)}(\vec{r}, \vec{r}_t) \rangle + \cdots \tag{4.5}$$

where $\Delta = \mu\omega^2 \sqrt{\langle \varepsilon_{\mathrm{r,f}}(r) \rangle^2}$. Under the assumption where there is a weak correlation between the unknown inhomogeneities i.e., $C(\vec{r}_1, \vec{r}_2) \approx 0$ (the multiple reflections between the fluctuating parts is ignored), the Green's function can be approximated by only the first term, i.e., $\langle \bar{\bar{G}}(\vec{r}, \vec{r}_t) \rangle \approx \bar{\bar{G}}^{(0)}(\vec{r}, \vec{r}_t)$. A random media with the Gaussian distribution with characteristic length $l_x =$ 5 cm, $l_y =$ 2 cm, and $l_z =$ 3 cm is modeled in the CST Studio Suite using a 3D form of Eq. (4.4). In the random media model, only one dominant and well-resolved wet spot is present in the yz plane of the antennas, and the rest of the plane has weak fluctuations. The reconstructed images from the UDT and MUDT are shown in Fig. 4.22. As can be seen from this figure, in the reconstructed image using the UDT approach, there exists strong artifacts. The location of the targets is not accurately reconstructed and stretched as well. The reconstructed image using the MUDT approach shows a better reconstruction with fewer artifacts images. However, an aliasing effect can still be observed.

4.3.1 Experimental results

Three different experiments were conducted in this section to examine the random distribution of inhomogeneities within a polymer foam. Each experiment involved injected water with a random distribution into the

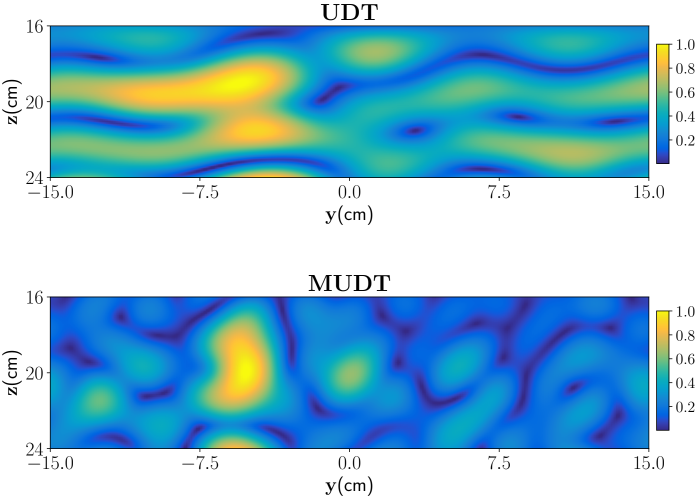

Fig. 4.22: Reconstruction of random media containing one dominant wet spot with UDT (top) and MUDT (bottom).

foam, with only a rough idea of its location. In the first experiment, water was injected at the center of the polymer foam and near the surface, and another water distribution was injected about 5 cm away from the center of the foam and at almost the same height. The reconstructed image of the first experiment is shown in Fig. 4.23 (top). As can be understood from this figure, the location of the injection is reconstructed. However, it is evident, that the injected water at the center is stronger than the one on the left (more amount of water was added). Also, since the permittivity of the water is high, a strong reflection at the bottom can be observed. This is due to the multiple reflections of the water and the bottom surface of the polymer foam. In the next experiment, another amount of water is injected into the polymer foam, but this time to the right-hand side and in the rough location of 7 cm. The reconstructed image of the second scenario is shown in Fig. 4.23 (middle). The presence of a target is clear in this image. However, the water in the middle is slightly deformed in the second experiment. This is due to the time of the measurement and the gravity. Since there was a delay

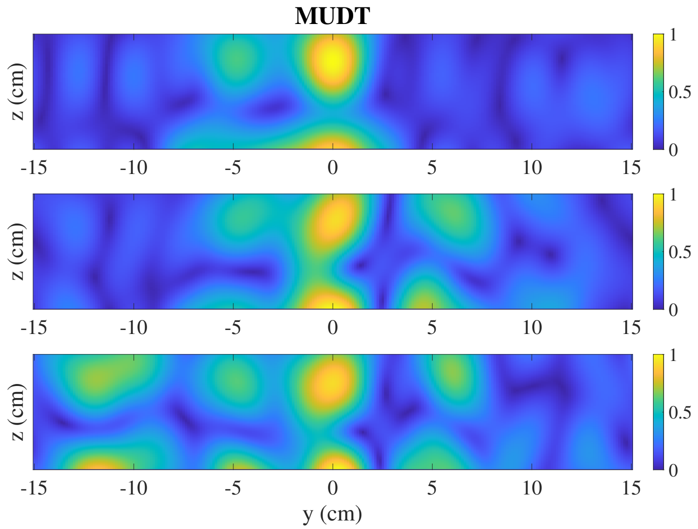

Fig. 4.23: Reconstruction of random media containing one dominant wet spot with UDT (top) and MUDT (bottom).

between the first and second experiments, part of the water is dragged down due to gravity. In the third experiment, another amount of water is added at the left side about 12 cm from the center, and close to the surface. The reconstructed image is depicted in Fig. 4.23 (bottom).

4.4 Shape Reconstruction

4.4.1 Numerical evaluation

So far, the spherical (sphere cross-section) target is considered inside the multilayered media. Consider a specific case where the target has a rectangular shape. It should be noted that a rectangular shape or any target with sharp corners will result in spatial-spectral components in the received (constructed) scattered field. So, it can be perceived more antennas will be needed to capture these spectral components for a successful reconstruction including corners or sharp changes. To demonstrate the impact of the shape of the target, the spectral representation of the received scattered field of the center antenna (4) (S_{44}) versus frequencies for different targets, including one sphere (radius of 1 cm), two spheres (radii of 1 cm), and one rectangular (width= 2 cm, length= 12 cm), is plotted in Fig. 4.24. As can be observed from Fig. 4.24, for one, and two spheres, the amplitude (variation) of the received electric field in the center antenna as compared to the rectangular targets is slow. However, for the rectangular shaped target, the variation becomes more severe, which means sharp changes in the spatial domain. Consider a rectangular target inside a three layered medium, as shown in Fig. 4.25. Two sets of antenna arrays are employed differently to illuminate the medium. In the first scenario, seven antennas with the center to center distance of 5 cm are interrogating the medium. And in the second scenario, fourteen antennas with the center to center distance of 2.5 cm are interrogating the medium. To implement the second scenario, the flange of the antennas has been removed to make them closer to each other. As can be understood from Fig. 4.26 (top), the target is split into two distinct sphere targets. However, employing more antennas that provides more sampling points can significantly increase the spatial resolution. As shown in Fig. 4.26 (bottom), the shape of the target is more convincingly reconstructed.

However, in some applications like microwave drying, the shape of the target is different and contains some smooth transitions. Those parts of the transition that are not electrically greater than the background will not

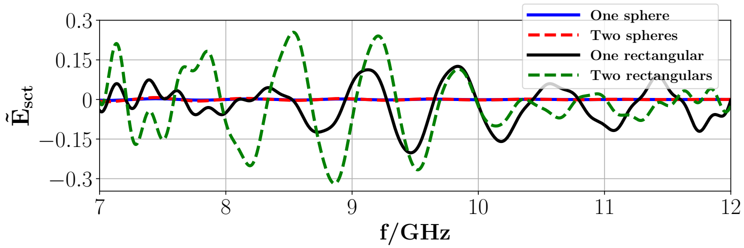

Fig. 4.24: Spatial Fourier transform of the received scattered field for the center antenna (antenna 4).

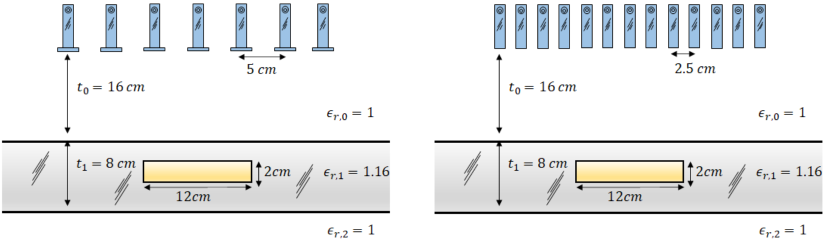

Fig. 4.25: (Left) Seven, and (Right) fourteen antennas are illuminating a three layered media. A rectangular dielectric target with the dielectric constant of $\varepsilon_r = 2$ is located in the background media.

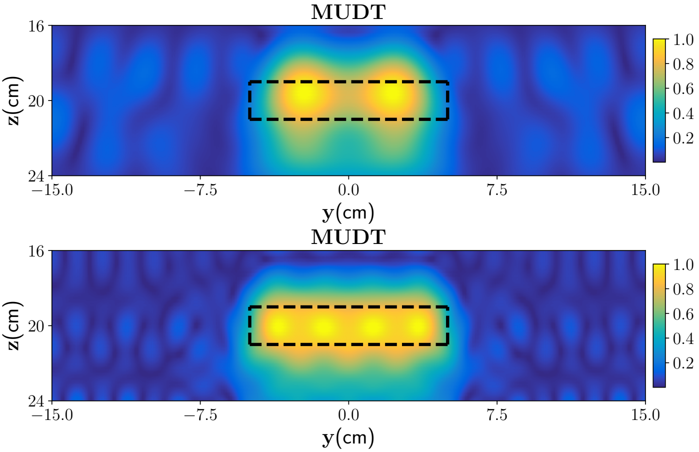

Fig. 4.26: Reconstructed image using MUDT algorithm with (top) 7 antennas, and (bottom) 14 antennas. Black dash lines show the true shape of the target. Black dash lines show the true shape of the target.

generate a scattered field, so those parts cannot be reconstructed or retrieved after the received signal is processed. On the other side, consider a dielectric distribution with a smooth transition where the dielectric value is electrically

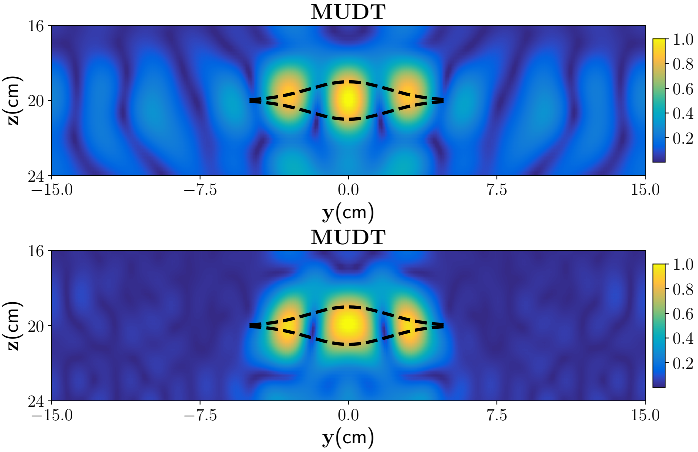

Fig. 4.27: Reconstructed image using MUDT algorithm with (top) 7 antennas, (bottom) 14 antennas for a Gaussian shape dielectric target.

greater than the background. The profile of the geometry of this smooth transition is modeled as follows

$$z(y) = \frac{\beta}{\sigma\sqrt{2\pi}} e^{-\frac{1}{2}(\frac{y-\mu}{\sigma})^2}. \tag{4.6}$$

where $\sigma = 20$, $\beta = 5$, and $\mu = 0$. Seven and fourteen antennas are employed to reconstruct the shape of the Gaussian dielectric target embedded in the three layered medium. The reconstructed images are represented in Fig. 4.27. As can be seen in this specific scenario, the MUDT is not capable of reconstructing the shape of the target even by increasing the number of antennas.

4.4.2 Experimental results

In order to demonstrate the effectiveness of the MUDT imaging algorithms for reconstructing shapes, a rectangular dielectric of PTFE Teflon with a length of 7 cm inserted into the polymer foam. The reconstructed

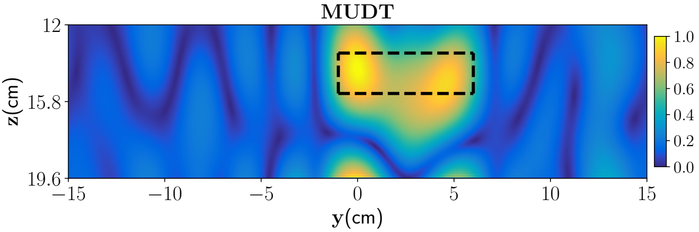

Fig. 4.28: Reconstructed image using MUDT algorithm with seven antennas. Black dashed lines show the true shape of the target.

images using MUDT are shown in Fig. 4.28, where seven open waveguide antennas with flanges are used for the image reconstruction. However, due to the antenna construction, it is not possible to remove the flanges and place them closer together to test the algorithm with more antennas in a fixed aperture length. Similar to Fig. 4.26 (top), the target is split into two distinct spherical targets.

4.5 High-Contrast Media

During the derivation of the MUDT (or UDT) algorithm, it is assumed that the contrast between two adjacent layers is small, so the reflected wave is ignored. In high-contrast scenarios where the two adjacent layers have a significant difference in dielectric constant, considering the reflected wave is inevitable. Here, it should be emphasized that in diffraction tomography-based algorithms, e.g., UDT [77], MUDT [93], incorporating the reflected part will render the integral undefined, as the closed-form of the object function cannot be evaluated by applying SPA. In other words, a stationary phase point in Eq. 2.19 cannot be found.

Consider a scenario where a PEC plate is located behind a dielectric layer and clung to that (layer 3). Due to the introduction of the PEC, a high variation in the contrast between the different layers exists. In this case, the reflected electric field from the PEC plate cannot be neglected. To display this effect, the total electric field or Green's function in case of a point source ($G^{(10)} =$

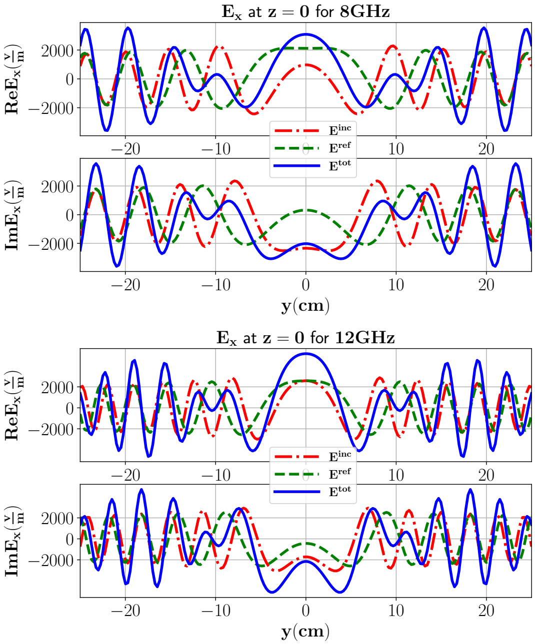

Fig. 4.29: The real and imaginary part of the total electric field inside a three layered medium with dimension 30 cm× 8 cm and $\varepsilon_{r,1} = 1.16$ for the dielectric layer at (top) 8 GHz and (bottom) 12 GHz. Layer 2 is PEC.

$G_T^{(10)} + G_R^{(10)}$) is compared to the transmitted electric field ($G^{(10)} \approx G_T^{(10)}$). The total and transmitted electric field responses are plotted at 8 GHz and 12 GHz based on the finite element method (FEM) of COMSOL and the analytical formulations computed in MATLAB R2018b. For the COMSOL simulation, the imaging domain consists of the dielectric with a domain size $y \in [-25, 25], z \in [16, 24]$ with relative dielectric constant $\varepsilon_{r,1} = 1.16 - j0.01$ backed by a PEC plate, and placed in the background domain Ω consisting of air.

As can be seen from Fig. 4.29, in this case (unlike the scenario without the PEC plate), the total electric field and the transmitted field do not match, and hence, $G^{(10)}$ cannot be approximated by the $G_T^{(10)}$. In this case, the Eq. (2.30) must be written as follow

$$E_n^{\mathrm{sct}}(\vec{r}_r, \vec{r}_t) = k^2 \int_{\Omega_n} G_{\mathrm{eb}}^{(n0)}(\vec{r}_r, \vec{r}') \cdot O_n(\vec{r}') G_{\mathrm{eb}}^{(n0)}(\vec{r}', \vec{r}_t)\, d\vec{r}'. \tag{4.7}$$

By substituting the $G^{(n0)} = G_T^{(n0)} + G_R^{(n0)}$ in the above expression it can be obtained

$$\begin{aligned} E_n^{\mathrm{sct}}(\vec{r}_r, \vec{r}_t) = k^2 \int_{\Omega_n} O_n(\vec{r}') \Big[\Big(G_T^{(n0)}(\vec{r}_r, \vec{r}', k_y) + G_R^{(n0)}(\vec{r}_r, \vec{r}', k_y) \Big) \cdot \\ \Big(G_T^{(n0)}(\vec{r}', \vec{r}_t, k_y') + G_R^{(n0)}(\vec{r}', \vec{r}_t, k_y') \Big) \Big] d\vec{r}'. \end{aligned} \tag{4.8}$$

By inserting the exact expression of the Green's function, i.e., Eq. (2.31), the spectral model of the received scattered electric field will be obtained. In this case, unlike Eq. (2.32), where the inner integral consists of any expression, the inner integral is composed of four different terms. The inner integral can be written in the same form as equation one. However, the SPA conditions cannot be met here, in other words, $\phi(h_0) \neq 0$. Consequently, in high-contrast media, a closed-form expression of the object function cannot be evaluated.

Consider three layers of media where the third layer is a PEC plate. A dielectric layer with a thickness of 8 cm is located at the top of the PEC plate, and the first layer is an infinite half-space where the array of the multistatic antenna is positioned. Two dielectric targets with radii of 1 cm, and center-to-center distance of 10 cm, are located inside the dielectric layer. The object function of low-contrast media, which is obtained in Eq. (2.45), is used here to reconstruct the image. The reconstructed image is shown in Fig. 4.30. The location of targets is shown with black dashed lines. It clearly illustrates the incorrect target detection in this case.

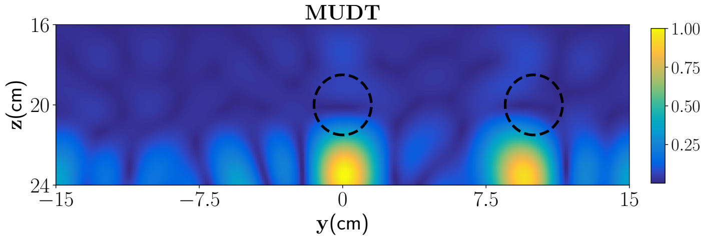

Fig. 4.30: Reconstructed image using the MUDT algorithm when the third layer is a PEC plate.

4.6 Time-Reversal Imaging of Layered Media

To apply the TRI, an exact or approximate dyadic Green's function (DGF) of the medium is required [129]. In [77, 79, 90, 92, 93, 130], only the transmission part of the Green's function is considered to locate the target in the multilayered media. An approximate expression of the DGF by incorporating both the transmission and reflection parts of the multilayered media is constructed. The closed-form representation of the DGF is obtained by applying stationary phase approximation (SPA). Here, it should be emphasized that in diffraction tomography-based algorithms, e. g., UDT [77], MUDT [93], incorporating the reflected part will render the integral undefined as the closed-form of the object function cannot be evaluated by applying SPA. Furthermore, a new single-frequency SF-TR-DORT will be introduced based on the behavior of eigenvalues of the TRO to foster high-speed DAQ.

4.6.1 Eigenvalue distribution in low contrast media

In the first scenario, the metal plate below the dielectric layer is not considered and the third layer is an infinite half-space. One dielectric target with $\varepsilon_r = 2$ in the second layer with a radius of 1.5 cm is considered, and located at the center of the dielectric layer, i.e., (0 cm, 20 cm) in yz plane. Figure 4.31 (top) represents the behavior of the first four eigenvalues. According to Fig. 4.31 (top), it is expected that one dominant wet spot in the dielectric layer and the remaining eigenvalues construct the noise space (background).

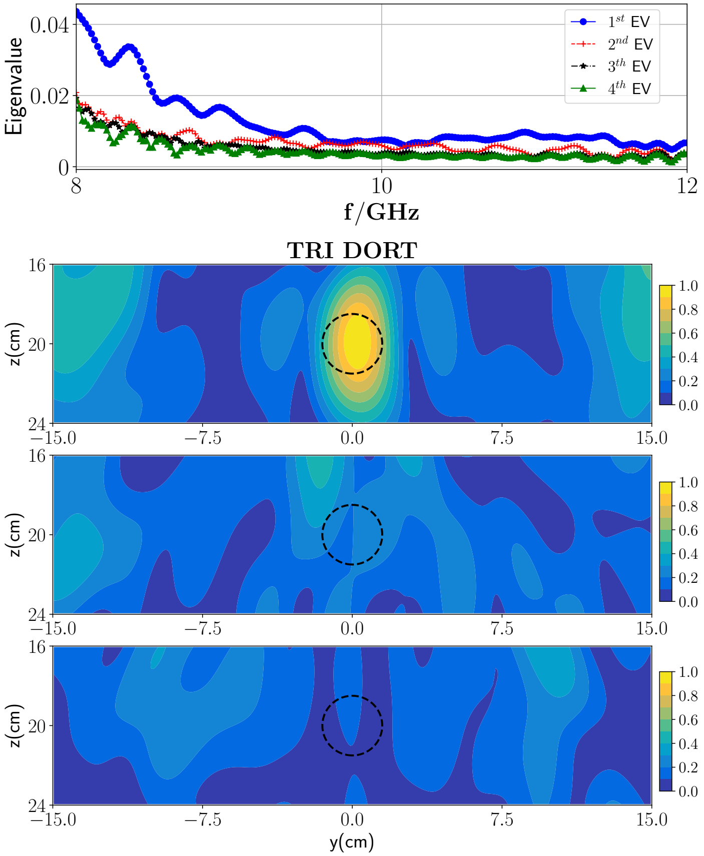

Fig. 4.31: (top) Magnitude of the first four eigenvalues versus the frequencies and, (second row) reconstruction of one wet-spot moisture case with TRI-DORT where the true location is marked by black dash lines, (third row) reconstruction using second eigenvalue and it's associated eigenvector, (fourth row) reconstruction using third eigenvalue and it's associated eigenvector.

Figure 4.31 (second row) shows the reconstructed image associated with the first strong eigenvalue and, employs the derived Green's function. As can be seen, using TRI-DORT, the image domain is decomposed into the dielectric target location and another part of the dielectric layer. Furthermore, reconstruction using non-dominant (second and third) eigenvalues is also provided. As can be seen from Fig. 4.31 (third and fourth row) and as mentioned earlier, these eigenvalues and associated eigenvectors represent the noise space. As each eigenvalue is associated with one dominant target inside the background layer, a separate image has to be shown for each of these dominant eigenvalues to illustrate the location of the target(s) inside the multilayered media.

In the next scenario, two dielectric targets with the dielectric constant of $\varepsilon_r = 2$ with a center-to-center distance 10 cm, and the same moisture level are considered in the dielectric layer. By applying the SVD to the stored scattering matrix in different frequencies, the eigenvalues can be plotted. Figure 4.32 (top) represents the behavior of the first four eigenvalues. As can be seen, two dominant eigenvalues can be observed and the remained eigenvalues belong to the null space. The corresponding TRI-DORT image associated with the first and second eigenvalues is plotted in Fig. 4.32 (second and third row). The imaging domain is decomposed into individual targets and the correct locations are obtained and selectively focused.

4.6.2 Eigenvalue distribution in high-contrast media

In this case, a metal plate (PEC) at the bottom of the polymer foam is considered i. e., the third layer shown in Fig. 4.33. Due to the introduction of the PEC, a high-contrast dielectric constant variation between the different layers exists. In this scenario, the reflected wave from the interface would not be negligible and should be considered in the formulation. As mentioned earlier, the Green's function is composed of two parts that are transmission and reflection.Both transmitted and reflected components of the EM field are considered in the modeling of Green's function, i.e, $G^{(10)} = G_T^{(10)} + G_R^{(10)}$. Figure 4.34 represents the comparison between the analytical model of Green's function and FEM. The figures are plotted in the same lines as Fig. 4.34. Moreover, to better represent the differences between the analytical model and FEM, the RMSE error is calculated, and the result is shown in Table 4.12.

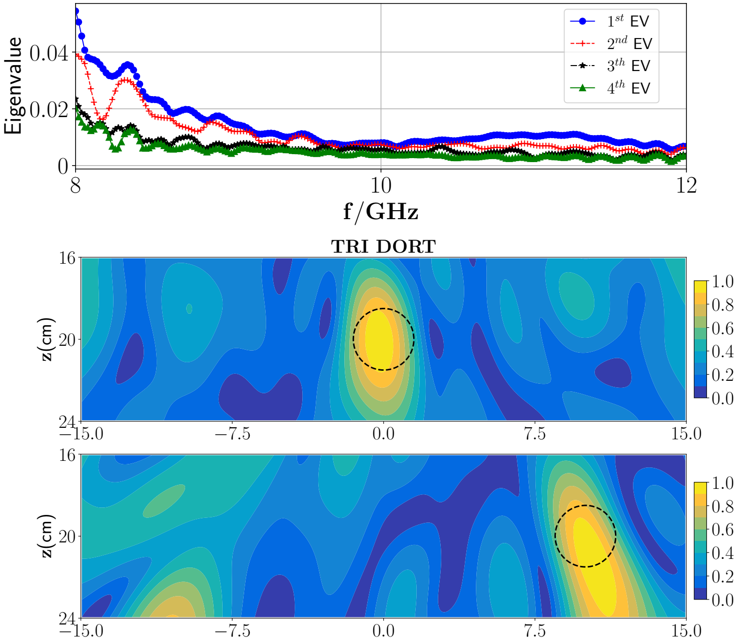

Fig. 4.32: (top) Magnitude of the first four eigenvalues versus the frequencies, (middle) reconstruction of the first wet-spot moisture case with TRI using first dominant eigenvalue, and (bottom) reconstruction of the second wet-spot moisture case with TRI-DORT using second dominant eigenvalue.

Table 4.12: NRMS value for compared analytical model and FEM in Fig. 4.34

	Re(E_x), 8 GHz	Im(E_x), 8 GHz	Re(E_x), 12 GHz	Im(E_x), 12 GHz
NRMS %	2.42	1.89	1.94	2.15

The presence of the two dielectric targets inside the layer 2 with the same specification as in the previous case is considered. Also, 3 % Gaussian noise with zero means is added to the data in this case to perform the numerical experiment. The first and second dominant eigenvalues are employed to focus on the first and second targets, respectively. Reconstruction images with updated $G^{(10)}$ are depicted in Fig. 4.35. The reconstructed images show

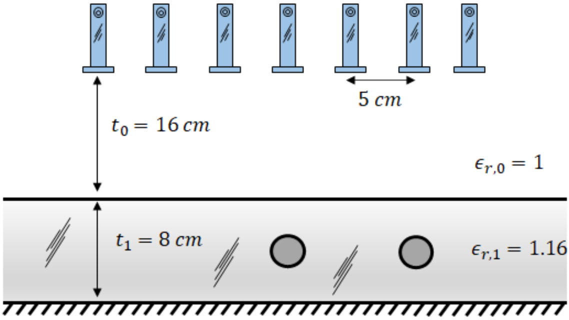

Fig. 4.33: Two dielectric targets with center to center distance of 10 cm, and the dielectric constant of $\varepsilon_r = 2$ in three layered medium. The thickness of the layer 2 is 8 cm. The layer 3 is PEC. The distance of the antenna to the layer 2 is 16 cm.

Table 4.13: Comparison between low and high contrast scenarios

Scenario	Low Contrast		High Contrast	
Method	λ_1	λ_2	λ_1	λ_2
RMSE (%)	28.84	34.79	30.54	35.36
RC (%)	57	43.5	48.17	44.55

that the two wet spots are properly detected. Upon comparison of the TRI reconstruction in Fig. 4.32 (without PEC) and Fig. 4.35 (with PEC), it can be seen that the presence of a PEC plate may provide a better reconstruction than with no PEC layer. It is due to the reflections from the PEC surface which augments in increasing the spatial resolution by providing some more views of the targets [131, 132]. It should be emphasized that the oscillations observed in the dominant eigenvalues are a result of the presence of the PEC plate beneath the multilayered media, causing the scattered field to oscillate, as illustrated in Fig. 3.5(bottom).

Furthermore, compared to the MUDT algorithm, in which, as mentioned earlier, only the transmission part is incorporated. The reconstruction using TRI clearly shows a better performance than MUDT. MUDT reconstruction as shown in Fig. 4.30 depicts the erroneous target detection in this case.

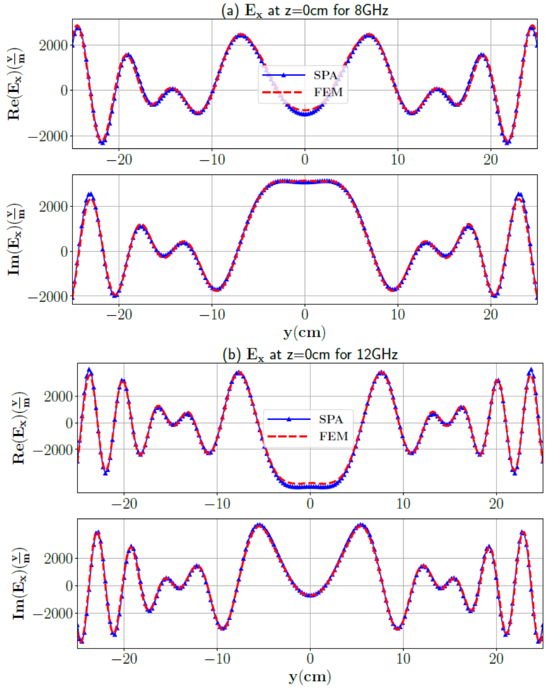

Fig. 4.34: The real and imaginary part of the total electric field inside a three layered medium with the dimension 30 cm × 8 cm and $\varepsilon_{r,1} = 1.16$ for the dielectric layer at (top) 8 GHz and (bottom) 12 GHz. Layer 3 is PEC.

4.6.3 Single frequency TRI

In practical applications, fast DAQ is a critical task. By decreasing the number of frequencies, the measurement time can be decreased. Single frequency TR multiple signal classification (SF-TRI-MUSIC) is proposed in [91, 133] to increase the resolution of the reconstructed image after reconstructing using ultra-wideband (UWB) TRI-MUSIC. Here, an SF-TR-DORT is proposed by observing the behavior of the eigenvalues. The reconstructed image is formed using different orthogonal eigenvectors and corresponding eigenvalues [134]. It allows a linear summation as represented in Eq. (2.64).

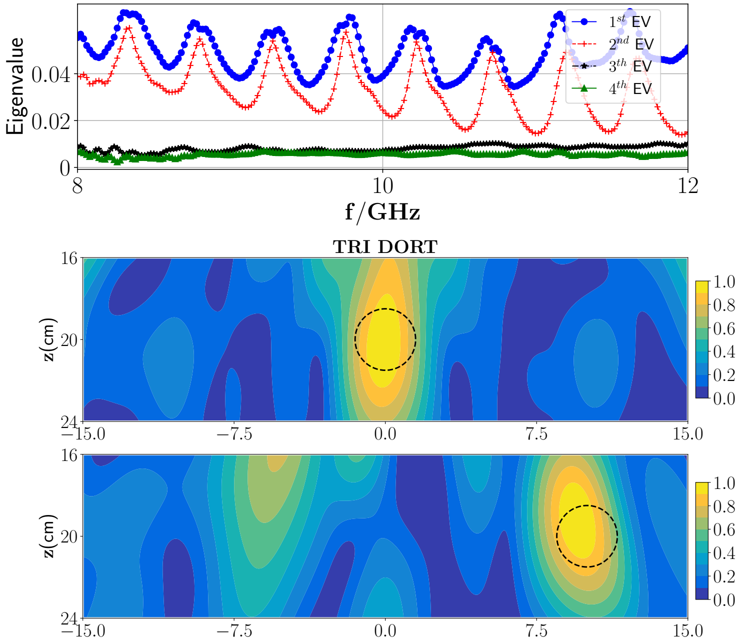

Fig. 4.35: (top) Magnitude of the first four eigenvalues versus the frequencies, (second row) reconstruction of the first wet-spot moisture case with TRI-DORT using first dominant eigenvalue and, (third row) reconstruction of the second wet-spot moisture case with TRI-DORT using second dominant eigenvalue when the layer 2 is PEC plate.

In the SF-TRI, this linear summation is approximated with one eigenvector and the associated eigenvalue, i.e, $\boldsymbol{D}_{p,SF} \approx \boldsymbol{D}_p \delta(\omega - \omega_{SF})$. To choose this frequency, the dominant eigenvalues are taken and compared with those that belong to the null space. Bigger differences mean the target domain is more distinguishable from the null space. As previously mentioned, the null space refers to eigenvalues that do not correspond to any targets within the media. The eigenvector associated with this eigenvalue ($v_{p,SF}$) forms a new excitation for calculating the $\boldsymbol{D}_{p,SF}$. So, instead of conventional TRI-DORT, a single frequency is chosen for the image reconstruction from Eq. 2.64 as

$$\boldsymbol{D}_{p,SF}(\boldsymbol{r}) = \lambda_{SF} v_{p,SF} g_{br}(\boldsymbol{r}, \omega_{SF}) \tag{4.9}$$

Table 4.14: Comparison between UDT and MUDT algorithm.

Scenario	f=8 GHz	f=9 GHz	f=10 GHz	f=11 GHz
RMSE (%)	30.56	37.3	43.58	42.39
RC (%)	49.87	40.64	31.96	36.18

From Fig. 4.32 (top), it can be seen that for the low frequencies, the difference between the dominant eigenvalue and those belonging to the null space is higher than at higher frequencies. The differences of the first eigenvalue and second eigenvalue at 4 different frequencies are as follows: $\Delta f_{8\text{GHz}} \times 10^3 = 6.7$, $\Delta f_{9\text{GHz}} \times 10^3 = 2.5$, $\Delta f_{10\text{GHz}} \times 10^3 = 2.0$, $\Delta f_{11\text{GHz}} \times 10^3 = 2.7$ as shown in Table 4. It can be expected that at 8 GHz there exists fewer shadow images and higher resolution than at other frequencies. Figure 4.36 shows the reconstruction using SF-TR-DORT for one single target in the media in four different frequencies. As can be seen, the location of the wet spot is visible in the domain. However, the spatial resolution slightly decreased by using a single-frequency approach.

It can be perceived from Fig. 4.36, since the eigenvectors are orthogonal for the different frequencies, by decreasing the number of frequencies, less information from the media under investigation is available, which leads to a decrease in spatial resolution compared to the multiple-frequencies reconstructed image. Also, the presence of multiple wet spots can plague the performance of the TRI algorithm for which the best-case strategy is to use the multi-frequency TRI algorithm. To reduce the DAQ time (DAQ) time for measurements of multiple frequencies, a specific band in the X-band can also be targeted. A pragmatic study in this direction is given in [135].

4.6.4 Experimental results

The experimental setup is already shown and discussed in Fig. 3.1 section 3.1. In the first experiment, as a low-contrast layered media, one PTFE Teflon sphere (radius 1.5 cm) is placed inside the foam with the center position of (0 cm, -0.7 cm, 20 cm). In this case, only the transmission part of Green's function ($G^{(10)} \approx G_T^{(10)}$) for image reconstruction can be applied.

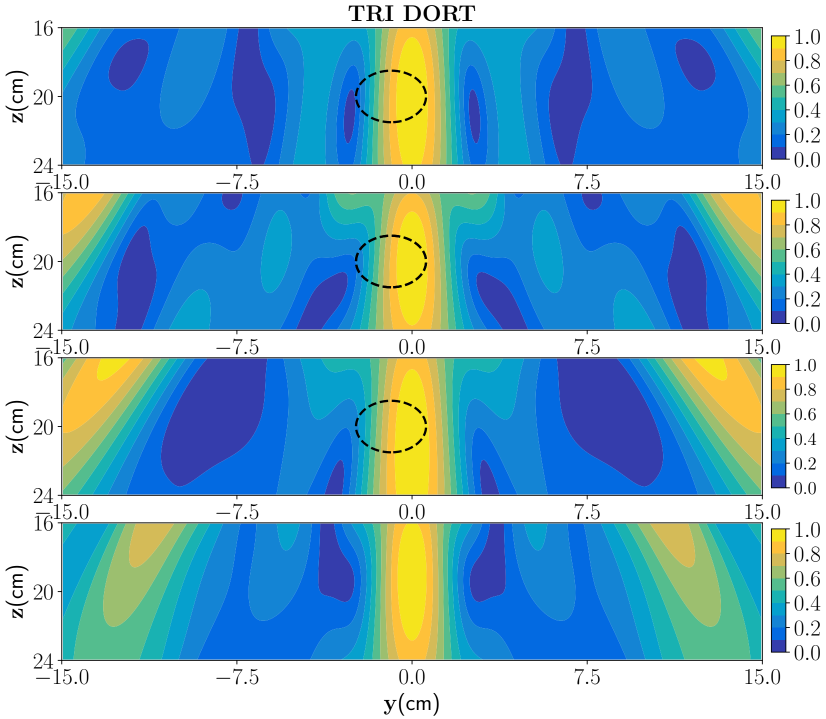

Fig. 4.36: Reconstruction using SF-TR-DORT at four frequencies (8 GHz, 9 GHz, 10 GHz, 11 GHz).

Furthermore, since the measurement response from the background media is known, it can be suppressed from the total response using the background subtraction procedure. In essence, the detection problem is studied here in terms of residual measurement which is obtained by subtracting the measurement response from the dielectric layer with the target from the measurement response without the target. Later, an antenna de-embedding is performed to convert the received S-parameters to the electric field. As can be seen from the depicted eigenvalues in Fig. 4.37 (top), there is one dominant eigenvalue, and the reconstructed image associated with this is shown in Fig. 4.37 (middle). As can be seen from this figure, the location of

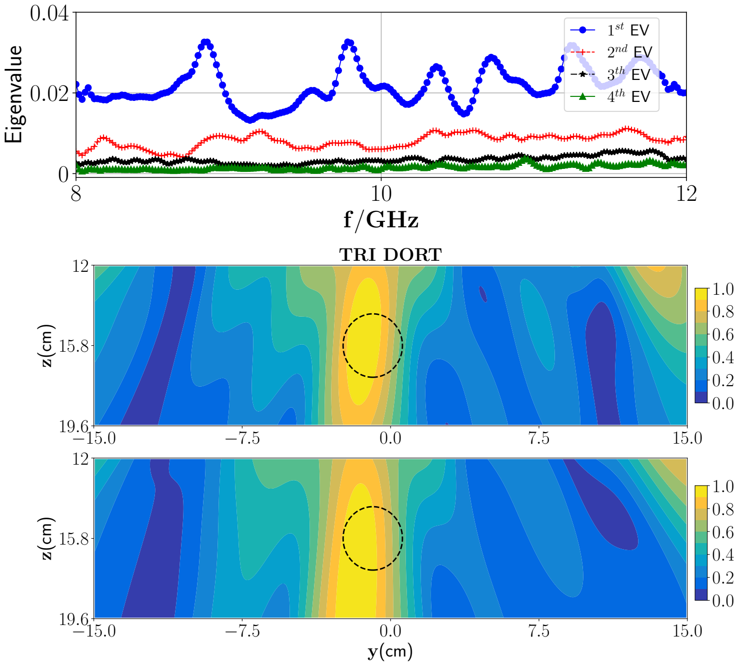

Fig. 4.37: (top) Magnitude of the first four eigenvalues versus the frequencies, and (middle) TRI-DORT reconstruction image of one PTFE Teflon and, (bottom) SF-TR-DORT at 8.07 GHz.

the target can be reconstructed. To apply the proposed SF-TRI-DORT, the f_{SF} is chosen based on the maximum difference between the first dominant eigenvalue and those belonging to the null space, which is f_{SF}= 8.07 GHz. Fig. 4.37 (bottom) demonstrates the SF-TRI-DORT. The position of the target is truly obtained, however, the spatial resolution is decreased.

In the second experiment, a PEC plate is inserted below the polymer foam. The PEC plate is used as a high-contrast layered media. A moisture-wet spot is inserted in the polymer foam. To create the wet-spot moisture target, a spherical foam of diameter 2.5 ± 0.1 cm and with 36 % wet-basis moisture level ($\varepsilon_r \approx 1.87 - j0.12$) is chosen. An approximate location of the target inside the foam is centered at (-35 cm, 1.2 cm, 20 cm). In this case, the

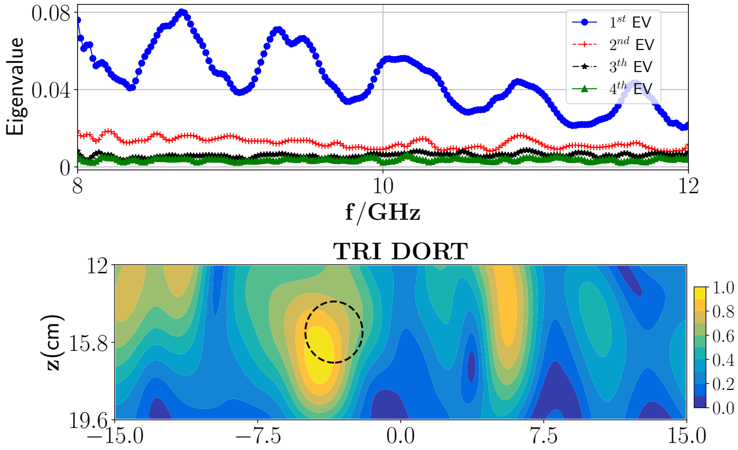

Fig. 4.38: (top) Magnitude of the first four eigenvalues versus the frequencies, and (bottom) TRI-DORT reconstruction image of one moisture wet-spot when the second layer is PEC plate.

transmission and the reflection parts of the Green's function ($G^{(10)} = G_T^{(10)} + G_R^{(10)}$) are applied for image reconstruction. The same steps are repeated as in the previous experiment to extract the MDM matrix from the measurement data. The eigenvalue behavior of the MDM matrix is shown in Fig. 4.38 (top) from which it can be observed that there is one dominant eigenvalue that indicates the presence of one wet spot in the media. The reconstructed TRI-DORT image associated with the first dominant eigenvalue is shown in Fig. 4.38 (bottom) which depicts that the estimated position of the target is correctly obtained with good spatial resolution.

There are a few design remarks for MWT that are worth noting. While TR imaging can address the issue of high-contrast media, it requires the full scattering matrix. On the other hand, MUDT only needs bi-static data to reconstruct images, making it preferable if the contrast between layers is not high. TRI can be extended to a single frequency while this is not the case for diffraction tomography-based algorithms. The spatial resolution provided by MUDT is also larger than that of TR imaging. Both methods are compatible with a limited view angle (more practical), meaning they do not require surrounding the media for successful image reconstruction. This can result in a lower number of antennas for the MWT system and less acquisition time.

5 Reconstruction of the Dielectric Constant

5.1 Singular Value Decomposition Based Approach for Dielectric Reconstruction

5.1.1 Dielectric constant estimation

In this part, the dielectric constant of the reconstructed targets is obtained from the qualitative imaging algorithms using the singular value decomposition (SVD) and minimization approach [64]. The reconstructed images of both MUDT and TRI can be used to achieve this. Starting from Eq. (2.30) and expressing it in the following matrix form for each frequency point

$$E_{\mathrm{sct}} = [\mathcal{L}_{\mathrm{o}}] \left[(\hat{\varepsilon}_r - \varepsilon_{r,n})\right], \tag{5.1}$$

where E_{sct} is of size $N \times 1$, $\mathcal{L}_o$ is the linear operator with size $N \times M$, and $(\hat{\varepsilon}_r - \varepsilon_{r,n})$ is the object function of size $M \times 1$. The term N denotes the total number of transmitter and receiver pairs and the term M denotes the total number of pixels in the imaging domain. The linear operator $\mathcal{L}_{\mathrm{o}}$ is given as

$$\mathcal{L}_{\mathrm{o}} = k^2 \int_{\Omega_n} \mathbf{g}_{T,r}^{(n0)}(r') \mathbf{g}_{T,t}^{(n0)^{\mathsf{T}}}(r')\, dr'. \tag{5.2}$$

The term $\mathbf{g}_{T,r}(r')$ and $\mathbf{g}_{T,t}(r')$ are the steering vectors of the transmission part of the background Green's function, expressed by

$$\mathbf{g}_T^{(n0)} = \left[G_{\mathrm{eb,T}}^{(n0)}(\vec{r}, \vec{r}_1), G_{\mathrm{eb,T}}^{(n0)}(\vec{r}, \vec{r}_2), \cdots, G_{\mathrm{eb,T}}^{(n0)}(\vec{r}, \vec{r}_N)\right]^{\mathsf{T}}, \tag{5.3}$$

where $(\cdot)^{\mathsf{T}}$ stands for the transpose operator. To calculate the dielectric constant, information from MUDT with thresholding operation and support domain of the targets is used before the next step. The thresholding operation on MUDT is performed to separate the dry part domain and wet-spot domain. The choice of the thresholding value is heuristic and is made to separate the background from the targets. The threshold operation, $\wp$, on the object function in (2.45) is performed as

$$O_n = \begin{cases} \varepsilon_{r,n} \; \forall \; O_n(y,z) \,|_{\wp<0.5} & \in \Omega_\mathrm{d} \\ \varepsilon_{r,g} \; \forall \; O_n(y,z) \,|_{\wp>0.5} & \in \Omega_\mathrm{h}. \end{cases} \tag{5.4}$$

The domain Ω_h will be assigned to the background dielectric constant ($\varepsilon_{r,n}$), and the remaining domain will be assigned to the unknown dielectric constant ($\varepsilon_{r,g}$). Using SVD, the scattering matrix can be decomposed into the eigenvectors and eigenvalue matrices, i.e., $\mathrm{SVD}(E_\mathrm{sct}^{(n)}) = U\Sigma V^\top$ where U is a complex unitary matrix, Σ is a rectangular diagonal matrix with non-negative real numbers on the diagonal, and V is a complex unitary matrix. The column of U and V form a set of orthogonal vectors or eigenvectors and Σ consists of eigenvalues. The number of non-zero eigenvalues represents the number of targets in the media and, the p^th target associates with the p^th eigenvalue of the matrix Σ [63, 64]. In order to obtain the dielectric constant of the p^th target in the media, the associated eigenvalue from the theory and measurement will be compared for different guessed values of the dielectric constant. The following minimization function is used

$$\widehat{\varepsilon} = \min_{\varepsilon_{r,g}} \sum_{f} \left\| \frac{{\sigma_p}^\mathrm{Meas}}{{\sigma_p}^\mathrm{Meas}\Big|_{\varepsilon_{r,c}}} - \frac{{\sigma_p}^\mathrm{Th}\Big|_{\varepsilon_{r,g}}}{{\sigma_p}^\mathrm{Th}\Big|_{\varepsilon_{r,c}}} \right\|^2 , \tag{5.5}$$

where ${\sigma_p}^\mathrm{Th}\Big|_{\varepsilon_{r,g}}$ denote the p^{th} eigenvalue from the theoretical calculation. The term ${\sigma_p}^\mathrm{Th}\Big|_{\varepsilon_{r,c}}$ denotes the p^{th} eigenvalue when the calibration target with given relative dielectric constant ($\varepsilon_{r,c}$) is used in the media. On the other hand, ${\sigma_p}^\mathrm{Meas}$ is the p^{th} eigenvalue of the measurement and, ${\sigma_p}^\mathrm{Meas}\Big|_{\varepsilon_{r,c}}$ is the p^{th} eigenvalue of the measured data once the calibration target is embedded into the media. In the latter case, the relative dielectric constant is ε_c. It should be noted, $\hat{\varepsilon}$ becomes minimum when the guess value of the dielectric constant is close to the true value. A Poly(methyl methacrylate) (PMMA) target with the dielectric constant $\varepsilon_{r,c} = 3.2$ is chosen for the calibration in (5.5). The above-mentioned steps are summarized in the following Pseudocode.

```
Calculate $O_n(y, z)$ using Eq. (2.45);
Apply threshold using Eq. (5.4);
Calculate $G_T^{(n0)}$ using Eq. (2.20);
$f \leftarrow range$;
$\varepsilon_{r,b} \leftarrow$ background media;
$\varepsilon_{r,c} \leftarrow$ calibration material;
$\varepsilon_{r,g} \leftarrow range$;
for $i \leftarrow 1 to\ length(\varepsilon_g)$ do
    $\hat{\varepsilon} \leftarrow 0$;
    for $f \leftarrow 1 to\ length(f)$ do
        Calculate $E^{sct}$ using Eq. (5.1);
        $[U^{\mathrm{Th}} \quad \Sigma^{\mathrm{Th}} \quad V^{\mathrm{Th}}] = \mathrm{SVD}(E_{\mathrm{sct}}^{(n)})$;
        $\sigma_p^{\mathrm{Th}} = \Sigma^{\mathrm{Th}}(p, p)$;
        $[U^{\mathrm{Th},c} \quad \Sigma^{\mathrm{Th},c} \quad V^{\mathrm{Th},c}] = \mathrm{SVD}(E_{\mathrm{sct}}^{(n)})$;
        $\sigma_p^{\mathrm{Th},c} = \Sigma^{\mathrm{Th},c}(p, p)$;
        $[U^{\mathrm{Meas}} \quad \Sigma^{\mathrm{Meas}} \quad V^{\mathrm{Meas}}] = \mathrm{SVD}(E_{\mathrm{sct}}^{\mathrm{Meas}})$;
        $\sigma_p^{\mathrm{Meas}} = \Sigma^{\mathrm{Meas}}(p, p)$;
        $[U^{\mathrm{Meas},c} \quad \Sigma^{\mathrm{Meas},c} \quad V^{\mathrm{Meas},c}] = \mathrm{SVD}(E_{\mathrm{sct}}^{\mathrm{Meas}})$;
        $\sigma_p^{\mathrm{Meas},c} = \Sigma^{\mathrm{Meas},c}(p, p)$;
        $\widehat{\varepsilon} = \widehat{\varepsilon} + \sum_f \left\| \frac{\sigma_p{}^{\mathrm{Meas}}}{\sigma_p{}^{\mathrm{Meas},c}} - \frac{\sigma_p{}^{\mathrm{Th}}}{\sigma_p{}^{\mathrm{Th},c}} \right\|^2$;
    end
    $\varepsilon = \min(\hat{\varepsilon})$;
end
```

Algorithm 1: Pseudocode for calculating the dielectric constant of the targets.

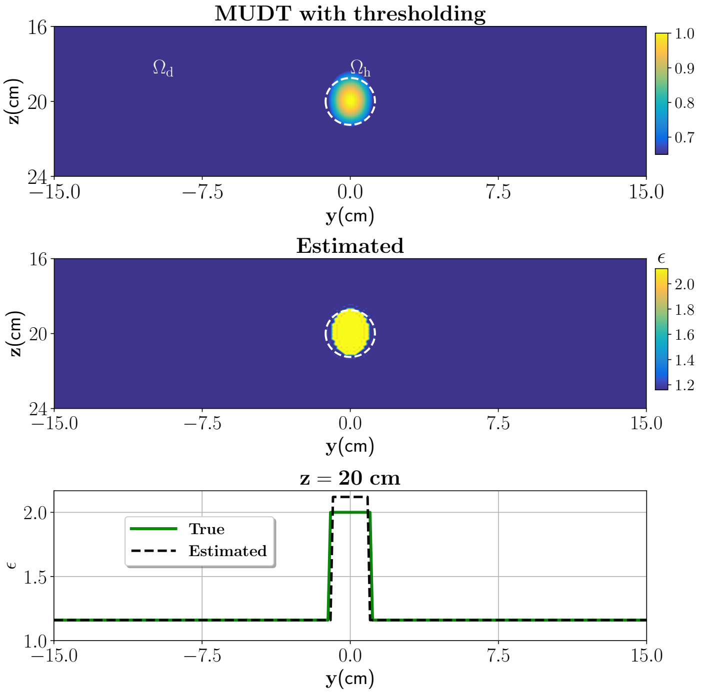

Fig. 5.1: MUDT reconstruction of one dielectric target with thresholding. The corresponding estimated values are shown in the center. The 1D plots at the bottom show the comparison of the estimated value with the respective true case.

5.1.2 Numerical evaluation

As a first example, the case where one target is located inside a three-layer media is evaluated. The location of the target was previously obtained using the MUDT in Fig. 4.3 (middle). After the thresholding operation, the background and the target parts are separated and assigned to dielectric values of $\varepsilon_{r,1}$ and unknown $\varepsilon_{r,g}$, respectively. Since only one target is visible in the reconstruction, it is evident that only one dominant singular value will exist in the measured scattering matrix. To solve the minimization problem in (5.5), the guess values are chosen based on the dielectric characteriza-

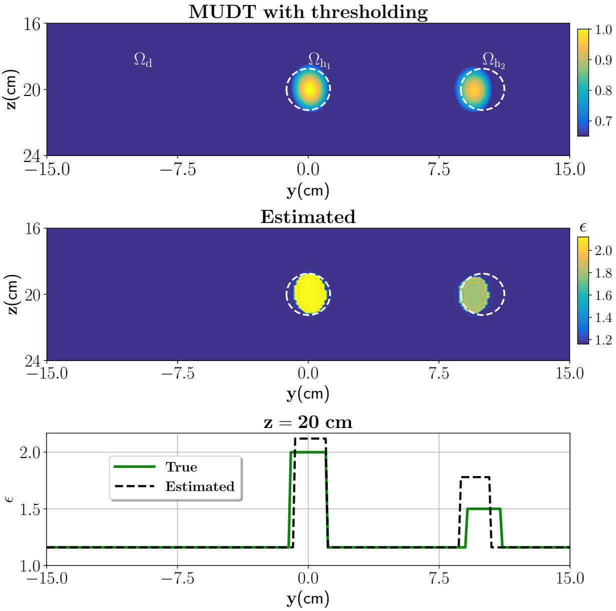

Fig. 5.2: MUDT reconstruction for two dielectric targets with thresholding. Its corresponding estimated dielectric constant values are shown in the middle. The 1D plots at the bottom show the comparison of the estimated values with the respective true cases.

tion. The MUDT reconstruction with thresholding operation and estimated dielectric value of the target are shown in Fig. 5.1 (top and middle). The similarity of the estimate to the true value, $\varepsilon = 2$, is shown in the 1-D plot of Fig. 5.1 (bottom).

In the next scenario, two targets with different dielectric constants inside the three-layered medium is investigated. The domain of the targets Ω_{h_1}, Ω_{h_2} were previously obtained using the MUDT in Fig. 4.5. As mentioned earlier, the location of the targets is visible and, after applying the thresholding, the second layer domain is separated into the background part and two targets. In this case, there exist two dominant eigenvalues which correspond to two target domains. Since the center target is dominant out of two, the largest eigenvalue is assigned to it and, the second largest

Table 5.1: Results of error analysis for different diameters.

d (cm)	2	3	4	5	6
ε_r	2.07	2.39	2.45	2.51	2.78
SE (%)	3.38	16.32	18.37	20.32	28.06

Table 5.2: Results of error analysis for different SNR.

SNR (in dB)	zero noise	30	20	15	12
ε_r	2.07	2.22	2.41	2.46	2.95
SE (%)	3.38	9.91	17.01	18.69	32.2

eigenvalue is for the second target. The minimization problem is solved separately and in parallel to obtain the dielectric constant of the targets. The MUDT reconstruction with thresholding operation and estimated dielectric value of the dielectric constants are shown in Fig. 5.2 (top and middle). The similarity of the estimate to the true values of the targets, $\varepsilon_{r,1} = 2$ and $\varepsilon_{r,2} = 1.5$, is shown in the 1-D plot of the Fig. 5.2 (bottom).

5.1.3 Sensitivity analysis

If the diameter (d) of the target size is increased, the estimated error of the dielectric constant increases due to the proposed method being based on the Born approximation. This means that the conditions for replacing the total field with the incident one inside the irregularities cannot be sufficiently met by increasing the diameter. Table 5.1 illustrates this by showing the estimated dielectric constant and its RMSE error for one wet-spot region. Furthermore, for a fixed diameter of one wet-spot case, the estimation error will also increase with a decrease in the signal-to-noise ratio (SNR), as shown in Table 5.2.

Table 5.3: Results of error analysis for different target scenarios.

True ε_r	1.35	1.52	1.83	2.13
True M(%)	17	25	36	46
Estimated ε_r	1.6	1.7	1.87	1.97
Estimated M(%)	27	30.5	37.5	41

5.1.4 Experimental results

In the first experiment, two PTFE Teflon spheres with a radius of 1.2 cm and dielectric constant $\varepsilon_{\text{tef}} = 2.1$ are used as the test targets. They are placed inside the foam with their centers located at (0 cm, -2 cm, 15.8 cm) and, (0 cm, -8 cm, 15.8 cm). Similar steps are followed as described in Section 5.1.2 to obtain the dielectric constant of the targets. The estimated dielectric constant of the targets is shown in Fig. 5.3. The similarity of the estimate to the true value, $\varepsilon_r = 2.1$, is shown in the 1-D plot of Fig. 5.3 (bottom).

In the second experiment, a moisture target is inserted in the polymer foam. To create the moisture target, a spherical foam of diameter 2.5 ± 0.1 cm and with 36% wet-basis moisture level ($\varepsilon \approx 1.87 - j0.12$) is chosen. An approximate location of the target inside the foam is centered at (0 cm, -3.5 cm, 14.6 cm). The reconstruction image based on MUDT is depicted in Fig. 5.4 (a). For better comparison in the reconstruction, cuts along the y-axis of Fig. 5.4 (b) are plotted. The estimated dielectric constant value of wet-spot obtained using the SVD approach and its comparison to the true case is shown in Fig. 5.4 (c) and (d), respectively.

Based on the table 5.3 and reconstructed values for the different target scenarios, an average of ±5.5 % error in the target percentage can be considered for the proposed algorithm. This error corresponds to the ±0.16 in the reconstructed dielectric constant.

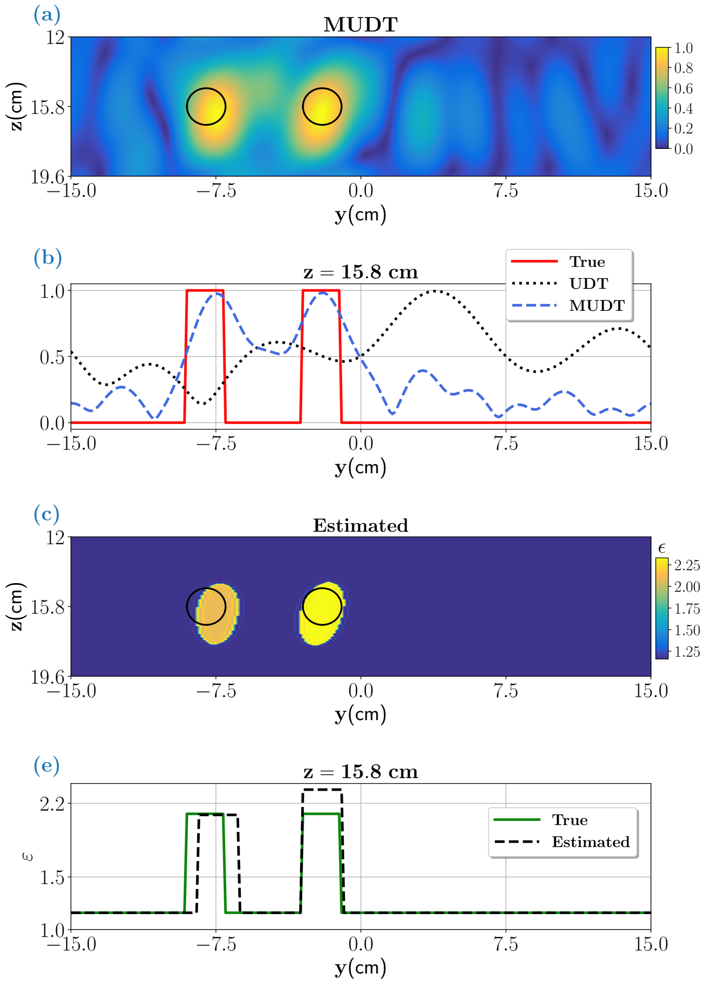

Fig. 5.3: Reconstruction of two dielectric targets in the foam is shown in (a), and (b) show a comparison of the UDT and MUDT approach with the true case for the object function values located at -15 cm $\leq$ y $\leq$ 15 cm for z =0 cm. The estimated dielectric values of the reconstructed targets using the SVD approach are shown in (c) and its comparison against the true case at z =1.35 cm as a 1D plot is depicted in (d).

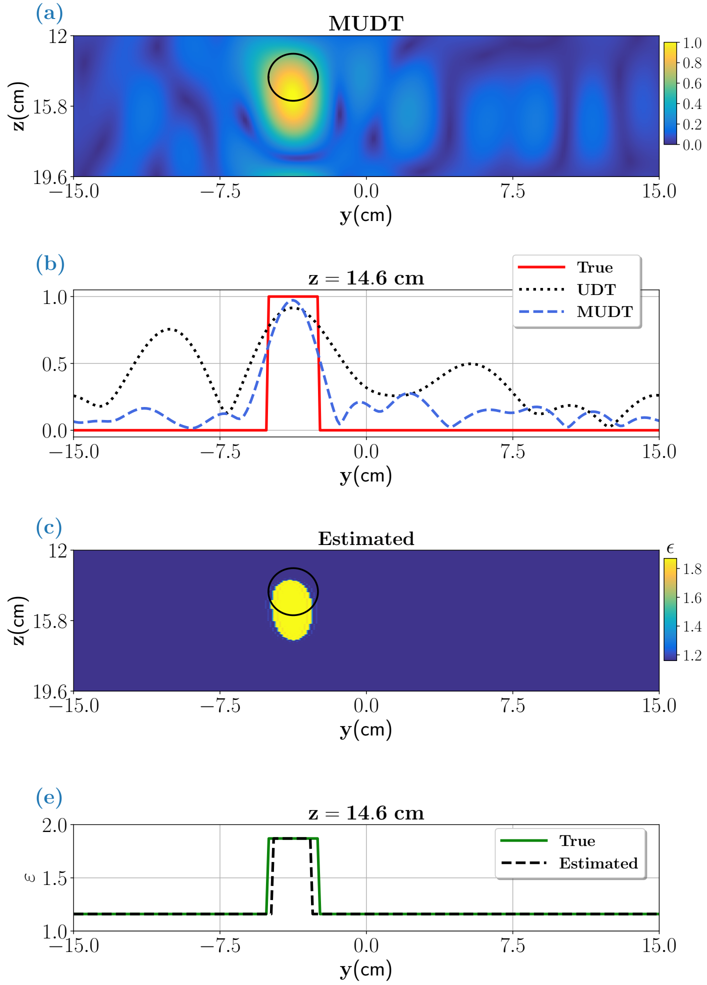

Fig. 5.4: Reconstruction of one dielectric target in the foam is shown in (a), and (b) show a comparison of the UDT and MUDT approach with the true case for the object function values located at -15 cm $\leq$ y $\leq$ 15 cm for z =1.35 cm. The estimated dielectric values of the reconstructed targets using the SVD approach are shown in (c) and its comparison against the true case at z =1.35 cm as a 1D plot is depicted in (d).

5.2 MUDT-Bayesian Inversion Framework for Dielectric and Shape Reconstruction

In the last sections, it has been seen using the MUDT, the location of an object inside the imaging domain is determined by the linear relationship between the object function and the received signal in the spectral domain. And in comparison to UDT [77, 78], the MUDT approach i) eliminates the need for mechanical scanning of the sensor, ii) provides aliasing-free images by following the Nyquist sampling criteria, and can resolve multiple targets with significant improvement in the spatial resolution.

In this section, the Bayesian Inversion Framework, coupled with the MUDT is used to determine the shape of the target and the dielectric constant. To accomplish the idea, the retrieved information from MUDT is segmented into regions of background and approximate target(s) and used to form prior covariance structure in a qualitative Bayesian inversion framework operating with single frequency data. The prior model is also known as structural prior information [136–138]. Figure 5.5 represents the idea of the proposed method in a nutshell. In the smoothness priors, generally, it is assumed that the coupling between the neighboring entries is the same everywhere [139]. It is not uncommon, however, to have spatial structural information about the unknown; this information can be encoded into the prior by accounting for the fact that the solution may jump across structure boundaries while being smooth within each structure. Knowledge about the structure may come from different sources [140–143] carrying complementary information about the structure of the scatterers or their location inside the imaging domain.

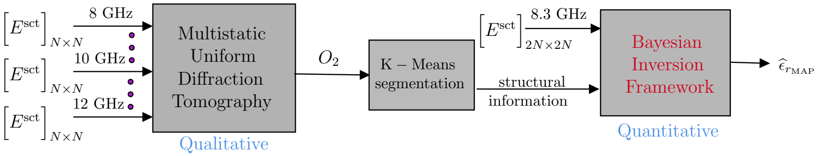

Fig. 5.5: General framework of the proposed method [144].

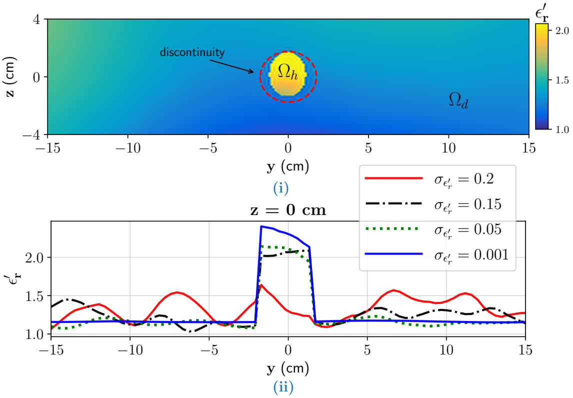

Fig. 5.6: (i) A sample realization from the structural-prior model derived using MUDT. (ii) Effect of values of $\sigma_{\varepsilon'_r} \in \Omega_d$ in the sample realization.

An illustration of MUDT reconstruction is shown in Fig. 5.6 (i) where the domains enclosed by the boundary curves are represented by Ω_{h_i}, where $i = 1, 2, 3$, indicates the expected target area and the domain represented by Ω_d indicates the background, respectively. To extract the system of coordinates (y, z) belonging to background and targets, the image from MUDT is segmented using K-means segmentation algorithm [145] as shown in Fig. 5.6 (ii). Note that the Formulation of the Bayesian Inversion Framework is shown in Appendix A. Further, to encode this structural information in the existing smoothness prior model, a varying degree of smoothness is applied in different regions i. e. in the background part and inside targets. Overall, the objective is to relax the smoothing constraints in the background areas along the tangential and normal directions. To achieve the different degrees of smoothness, CL components and standard deviation terms are chosen separately for background and target regions. Therefore, the prior covariance matrix is modified as

$$C_{ij} = \begin{cases} C_{ij}(c_y, c_z)\,\forall\, i, j \in \Omega_h \\ C_{ij}(c_y, c_z)\,\forall\, i, j \in \Omega_d, \end{cases} \tag{5.6}$$

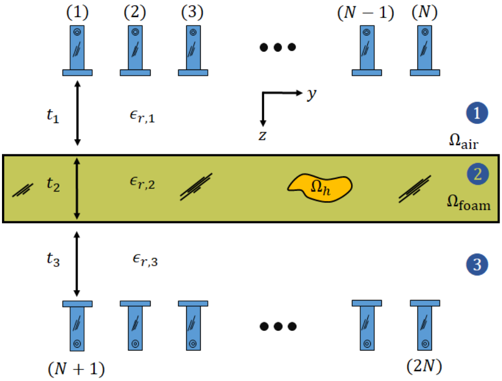

Fig. 5.7: Schematic of the free-space MWT setup used in this study. ©2022 IEEE.

where Ω_h and Ω_d represent approximated wet-spot and dry part regions, respectively. Large CL along with a small amplitude (standard deviation) in the dry part will constrain the estimate to have a constant neighborhood structure in the domain. This is equivalent to assuming that pixel elements are more correlated in the dry regions. Note that in the above expression though the CL components have the same representation while implementation they are given different values. The 2D configuration of the multistatic microwave tomography system studied in this work is illustrated in Fig. 5.7 with antenna array located on top and bottom of the foam, respectively. The free space is represented as layer 1 and layer 3 and the foam is represented as layer 2 with random embedded irregularities denoted by Ω_h. In free space, the relative dielectric constant is denoted as $\varepsilon_{r,1}$ whereas the relative dielectric constant of the foam is set to $\varepsilon_{r,2}$, and the dielectric constant of the irregularity is set to $\varepsilon_{r,i}$. The distance of the top and bottom antenna to the top and bottom of the polymer foam is $t_1 = t_3$, and layer 2 has thickness t_2. Implementation details of the Bayesian Inversion Framework are discussed in [13, 146] and only the main results are shown here.

5.2.1 Numerical evaluation

Sample realization from the structural a' priori model using (20), when one wet spot is assumed to be detected from the MUDT reconstruction, is shown in Fig. 5.6 (i). For the drawn sample, in the dry part domain (Ω_d), CL of c_y=30 cm, and c_z=8 cm and $\sigma_{\varepsilon_r'} = 0.15$ are assumed and for the wet-spot, a CL c_y=3 cm, and c_z=3 cm and $\sigma_{\varepsilon_r'} = 0.5$ are assumed with a mean value of $\eta_{\varepsilon_r'} = 1.16$. As can be clearly seen, in the dry part the smoothness is varying slowly due to the large CL, and in the approximate wet-spots region the variation is approximately constant. Also, the data on the cross-section line z =10 cm is plotted for different variance terms and constant correlation lengths in the dry part and as shown in Fig. 5.6 (ii). It can be seen that a smaller variance provides a more realistic coupling between the neighboring entries in the Ω_{foam}. The above strategy to generate the structure a priori can be extended to N numbers of scatterers (wet spots) in the domain. The first scenario is to obtain the location and level of one dominant wet spot in the polymer foam. Assume a spherical wet spot with a radius of $0.67\lambda_c$ located at the center of the polymer foam, i. e., (12.5 cm, 0 cm, 0 cm) with 35 % moisture level ($\varepsilon_r \approx 1.7 - j0.068$) and surrounded by the dry part. Fig. 5.8 (top) shows the reconstructed image using the MUDT imaging algorithm. As can be perceived from this figure, the location of the wet spot is correctly obtained with the normalized value of the object function. The red dashed line represents the true domain of the object. For better comparison, cuts along the y-axis of the true distribution and reconstructed distribution, i. e., $\frac{O_2(y,z)}{\max(O_2(y,z))}$ are plotted in Fig. 5.8 (second row).

To calculate the MAP estimate, information from MUDT with K-means segmentation is used in the structural smoothness, prior model. In the structure a priori, the CL is set to c_y =30 cm, and c_z =8 cm for the dry part (with very low STD values set for $\sigma_{\varepsilon_r'}$, and $\sigma_{\varepsilon_r''}$) and for the supported domain of wet-spot, CL of c_y =3 cm, and c_z =3 cm (with STD values set for $\sigma_{\varepsilon_r'} = 1$, and $\sigma_{\varepsilon_r''} = 0.075$) are chosen. The sigma values in the wet-spots regions are selected based on the dielectric characterization data and $\pm 3\sigma$ can account for 99 % of the dielectric values in the prior from the set mean

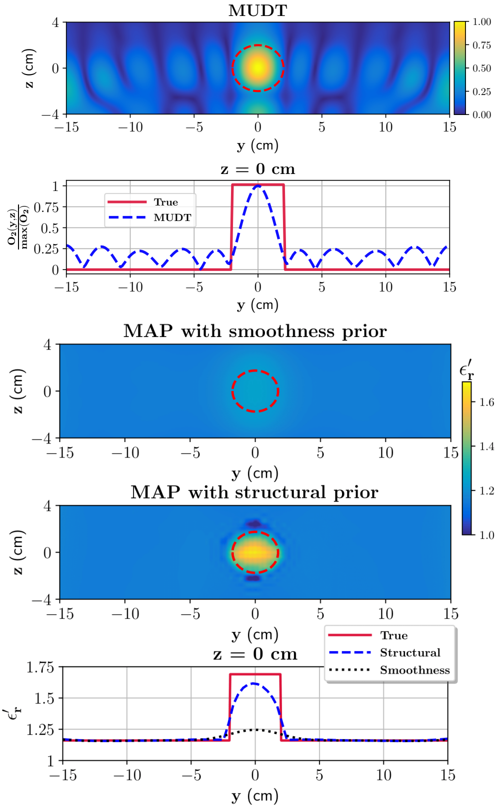

Fig. 5.8: MUDT reconstruction in the top figure for one wet spot. The bottom figure shows the comparison of MUDT with the true case for the pixel values located at data line z =0 cm.

value of $\eta_{\varepsilon_r} = 1.16 - j0.01$. The aforementioned STD values in both the prior models are used in the remaining cases as well.

Also, the MAP estimates with a smoothness prior model are evaluated with a CL of c_y =8 cm, and c_z =4 cm. In the smoothness prior, $\sigma_{\varepsilon_r'} = 1$, $\sigma_{\varepsilon_r''} = 0.075$ and $\eta_{\varepsilon_r} = 1.16 - j0.01$ are set. The MAP estimates with a smoothness prior model and structural prior model are shown in Fig. 5.8

(third and fourth rows). With the smoothness prior, the location of the wet spot is somewhat enlarged and the real part of its dielectric value is underestimated. With the structural smoothness prior, the MAP estimate for the real part of the dielectric constant is very close to the true case, and also the wet spot is recovered within the correct domain. Further, for easier quantitative comparison, pixel values at data line $z = 0$ cm are compared against the true case and shown in the last figure of Fig. 5.8 (bottom). The structural prior follows the discontinuities and aligns closer to the real value than the smoothness prior case. The RC and RMSE values for this case are given in the third row of Table 5.4 which depicts the accuracy of the structural prior over the smoothness prior. Note that in both MAP estimates, the imaginary part is overestimated or underestimated and hence not shown. Note that (i) small characteristics lengths in the moisture regions (say < 2 cm) may lead to possible false solutions and thus be avoided, (ii) improvement in the image reconstruction is envisaged to be linked to the structural information that is the information of the discontinuities in the solution. Therefore, efforts to study the performance of the MAP solution with respect to different characteristic lengths in the moisture regions are subdued.

Piece-wise homogeneous moisture distribution

In this scenario, a rectangular distribution for the wet spot is considered with a moisture content of 30 % ($\varepsilon_r \approx 1.58 - j0.06$) and dimension $2.6\lambda_c \times 1.3\lambda_c \times 6.5\lambda_c$ located at the center of the foam. The reconstructed image using MUDT is shown in Fig. 5.9 (top). As can be seen from this figure, the exact boundary of the distribution is not reconstructed. Although, the K-means segmentation has resulted in covering a slightly bigger domain. The MAP estimates are calculated based on the parameter set in the previous case. The results are shown in Fig. 5.9 (second row). The corners/discontinuities are difficult to estimate with the smoothness prior and more so the estimation shows an irregularity with stretched boundaries and an incorrect amount of moisture. As can be seen, the structural prior detect the irregularity and locate it more accurately than the smoothness prior. Overall, its performance is more accurate as evident from the line graph in the last figure of Fig. 5.9

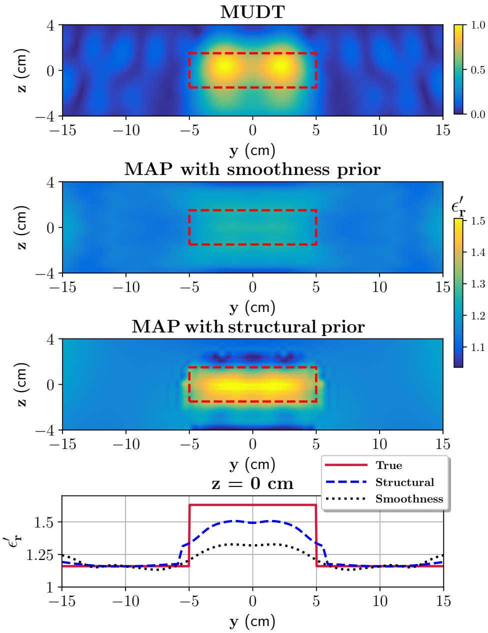

Fig. 5.9: MUDT and MAP estimates for the rectangular (left) and two wet spots with different moisture (right) cases. For both cases, the bottom figure shows the comparison of MAP with structural and smoothness prior model with the true case for the pixel values located at data line z =0 cm.

(bottom) and the RC and RMSE values for this case as provided in the fourth row of Table 5.4. Note that even though the CL in the structural prior is set to the previous case, which does not match the actual changes, the result is still better.

Wet-spots with different moisture

In the drying process, i) non-uniform microwave heating during the drying process or ii) non-uniform impregnation, may produce wet spots with different moisture levels. Hence, in a more pragmatic case, two spherical wet spots with different moisture levels and with radii of $0.67\lambda_c$ are assumed.

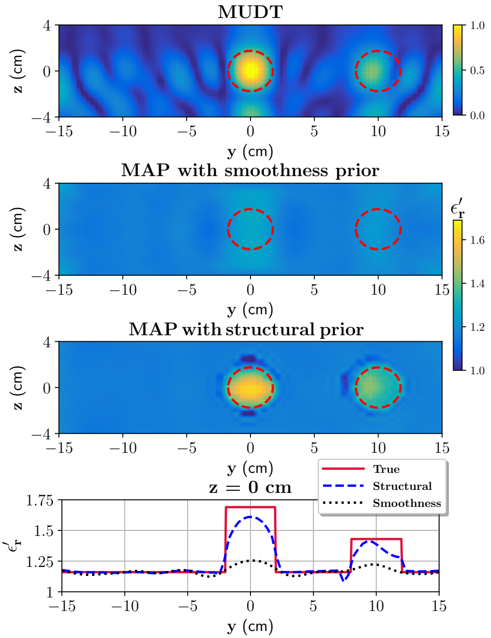

Fig. 5.10: MUDT and MAP estimates for the rectangular (left) and two wet spots with different moisture (right) cases. For both cases, the bottom figure shows the comparison of MAP with structural and smoothness prior model with the true case for the pixel values located at data line z =0 cm.

The location of the first wet spot is (12.5 cm, 0 cm, 0 cm) with 35 % ($\varepsilon_r \approx 1.87 - j0.12$) moisture level and the second wet-spot is centered at (12.5 cm, 10 cm, 0 cm) with 25 % moisture level ($\varepsilon_r \approx 1.48 - j0.056$).

The dominant wet spot is clearly detected by the MUDT, however, the weaker wet spot is also visible but not as strong as the other one, as represented by the red dashed circle at top of the Fig. 5.10 (top). Following K-means segmentation (not shown here), for the two moisture regions (Ω_{h_1} (middle wet-spot), Ω_{h_2} (right wet-spot)) the CL are set to c_y =3 cm, and c_z =3 cm. With the smoothness model, it is clear that it can indicate the stronger and weaker wet spots but with underestimated real part of the

Table 5.4: RMSE and RC parameter.

Prior	**smoothness**		**structural**	
Error metric	**RMSE**	**RC**	**RMSE**	**RC**
Case1: one wet-spot	6.33	0.73	4.23	0.88
Case2: rectangular wet-spot	9.03	0.59	5.57	0.91
Case3: wet-spots (different moisture)	7.40	0.59	4.41	0.90

dielectric value and over-shaped domain. However, with the structural prior, the MAP estimate for the real part of the dielectric constant is very close to the true case for the weaker wet spot and quite close to the stronger wet spot. Also, both wet spots are recovered within the correct domain. Further, to assess the closeness of the estimate from two prior models, pixel values at data line z =0 cm is compared against the true case and shown in the last figure of Fig. 5.10 (second, third, and fourth rows). Again, the reconstruction accuracy is better with the combined approach. The corresponding RC and RMSE values are provided in the last row of Table 5.4.

5.2.2 Experimental Results

To create the one moisture irregularity, a spherically shaped foam of diameter 2.5 ± 0.1 cm and with 45 % wet-basis moisture level ($\varepsilon_r \approx 2.0 - j0.092$) is chosen and placed inside the foam (see number Tag 2 in Fig. 3.11) through the incision. An approximate location of the irregularity inside the foam is centered at (0 cm, -9 cm, 1.55 cm). The image obtained using MUDT is shown in Fig. 5.11 (i). As can be seen, the location of the wet spots is correctly estimated but with a slightly elongated domain for the wet spot. More so, the dry and moisture areas are clearly discernible. From the MUDT image, the structural information is extracted using K-means segmentation (not shown here) and utilized to form the structural prior model in which the CL of c_y=25 cm, and c_z=7 cm for the dry part and for the supported domain of wet-spot, CL of c_y=3 cm, and c_z=3 cm are chosen. Also, the MAP

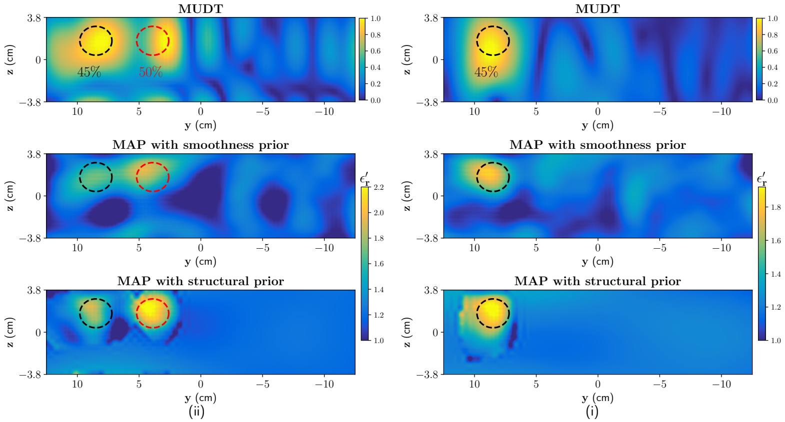

Fig. 5.11: MUDT and MAP estimates for cases (i) one wet-spot with 45 % moisture and (ii) two wet-spots with 45 % moisture and 50 % moisture, respectively. The dashed circles indicate the true positions of the wet spots.

estimates are evaluated with a smoothness prior model only with a CL of c_y=8 cm, and c_z=4 cm. The MAP estimates are shown in the middle and last row of Fig. 5.11 (i). Although the wet spot is somewhat correctly located in both priors, it is the structural prior that has estimated the moisture levels (represented here in terms of the real part of the dielectric constant) more accurately than the smoothness prior to solution. In addition, false artifacts are also visible in the MAP solution with a smoothness prior. Improvement in the image quality with structural prior can be speculated to be due to the suppression of smooth variations in the background (i. e. the dry part). In the second experiment, two wet spots with moisture percentage of 50 % ($\varepsilon_r \approx 2.2 - j0.1$) and 45 % ($\varepsilon_r \approx 1.98 - j0.076$) are positioned inside the polymer foam. The location of the wet spot with 50 % is centered at (0 cm, -3.6 cm, 1.55 cm) and the location of the wet spot with 45 % is the same as in the previous case. The MUDT image for this case is shown in Fig. 5.11 (ii). The wet spot on the left is located correctly but a shift is seen for the second irregularity. In the K-mean segmentation, the two regions got merged as the two irregularities are close and share the same neighborhood; it then results in forming a nearly ellipsoid region which is then used in the structural prior.

To evaluate the MAP estimate the characteristics and length parameters are kept the same as in the previous case. From the MAP estimates in Fig. 5.11 (ii), even though the structural information from segmentation indicated a wider domain, the two wet spots are retrieved more accurately than with the smoothness prior.

Moisture in cubic inclusions

In this case, two cubic shape pieces are cut out from the foam and infused with moisture levels of 55 % ($\varepsilon_r \approx 2.2 - j0.1$) and 60 % ($\varepsilon_r \approx 2.4 - j0.16$) in its full volume, respectively. After moisture infusion, the respective pieces are placed on the cut-out location. It shall benoted, it is assumed the gravity and time, doesn't change the moisture level and it's uniformity. The geometry is shown in Fig. 5.12 (left). The MUDT image for this case is shown in Fig. 5.12 (right) in which the inclusion on the left is indicating

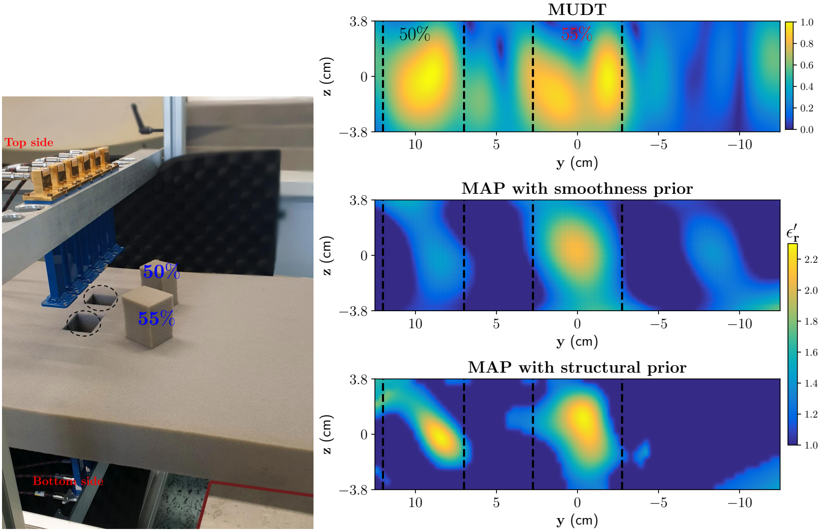

Fig. 5.12: Left: two cubic moisture case: moisture levels of 50 % and 55 % are impregnated in the incised foam, respectively. Right: MUDT and MAP estimates for the two cubic cases. The dashed lines indicate the true positions of the inclusions.

the presence of moisture, though not in full volume, and inclusion in the middle indicates the presence of multiple wet spots. Thus, the localization information from MUDT is seen to be slightly decreased in this case may be due to the limited view and limited independent data. In the structural prior, the same CL in both the moisture regions is set. From the MAP estimates in Fig. 5.12 (right), although the structural information from segmentation was somewhat inaccurate as it includes multiple wet spots in the middle inclusion, a clear presentation of higher moisture is still indicated, though not in full volume, in the MAP solution with a structural prior model in comparison to the smoothness based solution that can only locate moisture presence in the middle inclusion. The false solution in the smoothness prior model can be speculated to be due to over-regularisation or smoothing effect. Overall, incorporating a structural prior model has improved the accuracy of estimated moisture location and its dielectric properties. It's also noticed that even with the change in CL to larger values the results show no significant change.

6 Conclusion

In this work, the application of microwave tomography (MWT) toward new emerging applications in industries like microwave drying is demonstrated. The imaging modalities are applied to estimate the location and dielectric constant of the targets in the multilayered media. To reconstruct the image, the Multistatic Uniform Diffraction Tomography (MUDT) approach and the Time Reversal Imaging (TRI) are derived and applied. A singular value decomposition (SVD) based approach, as an extension of the above-mentioned imaging technique, is developed to retrieve the dielectric constant of the targets. Both techniques are examined under the limited view of multi-static case conditions with numerical and experimental data received from the developed MWT system. Experimental imaging results show a sufficient performance of the developed imaging modalities to locate and estimate the targets inside the multilayered media.

For the fast image reconstruction of the MWT, the Green's function of the multilayered media is obtained in the spectral-frequency domain. Using the stationary phase approximation (SPA), it is reduced to a new closed-form model. To obtain the Green's function of the multilayered media, the boundary condition for one arbitrary oblique plane wave is applied at the different layers, and the transmission and reflection coefficients are derived. By applying an integration to the coefficients with the various spectral weights, Green's function, which is the response to the point source, is derived.

A novel 2-D MUDT imaging algorithm is presented for a fixed-array-based MWT setup to image the location of the target(s) in a multilayer media. Its computationally efficient formulation is derived by assuming the imaging domain as planar multilayered media and using first-order Born approximation with proper DGF expression and SPA solution. The proposed algorithm is an extended version of the UDT algorithm and formulated to support multiple-input multiple-output antenna data. In the former method, raster scanning or single-input single-output data should be available which is time-consuming and does not fit the real-time application and dielectric constant that shall be retrieved. Numerical examples with 3-D multistatic scattering data for the considered sparse target(s) scenarios in the multilayer media demonstrate that MUDT provides a significant improvement over UDT in the reconstruction of aliasing-free and distortion-less images, and in resolving multiple-scatterers in the multilayered media. The better performance of the MUDT than the UDT approach is due to the Nyquist sampling rate criteria being satisfactorily met in this case. By increasing the number of targets in the background layer, displacement and distortion are observed in the UDT approach. However, in the MUDT approach, the scattered fields are more discernible rather the monostatic array. So, the antenna array would be able to recognize each target separately. It is observed MUDT decreases the RMSE error by about 17 % compared to the UDT. Moreover, the introduced RC value is increased by 0.2 with MUDT for one or two target cases and by 0.3 for three target cases.

Also, the proposed approach offers efficient performance in locating the scatterer(s) domain for special cases like when the top surface of the media is assumed random rough and for the case when the imaging domain is a random inhomogeneous media. For the non-ideal multilayered media, the Green's function of the medium with the smooth surface is applied to estimate the roughness of the medium with one or more rough surfaces. To evaluate the performance of the MUDT approach under the roughness condition, three layered medium with a roughness for the top interface is considered. It is observed by increasing the roughness of the top interface, that the MUDT approach is still capable of localizing the target inside the dielectric layer. However, a strong aliasing effect is observed when the UDT approach is employed. By increasing the roughness to the $f_{max} = 0.5$, the NRMS of the UDT approach increased by about 4 %, and the RMSE of the MUDT approach increased by about 1.5 %. Moreover, the dielectric constant of the dielectric layer is increased to survey the effect of the roughness. The MUDT approach successfully reconstructed the images by increasing the f_{max}. However, when the $f_{max} = 0.27$, the UDT failed to localize the target location, and MUDT contained an aliasing effect. In this regard, the RMSE value for the MUDT approach increased from 17.16 for $f_{max} = 0.1$ to 28.36

for $f_{max} = 0.5$. It can be concluded that increasing the dielectric constant of the background multilayered under roughness conditions, descend the performance of the MUDT approach.
If background media is not deterministic and contains some fluctuation in the dielectric constant, the MUDT is still capable of detecting the target location. In this regard, a Gaussian distribution is modeled in CST software to model the random medium. The reconstructed image using MUDT showed the true location of the target, in addition to an aliasing effect, coming from uncertainty in Green's function modeling and skipping the correlation between the inhomogeneous. Considering the correlation in Green's function modeling will lead to a more exact reconstructed image. But it is more difficult to formulate the problem. It is also shown that the MUDT approach partially reconstructs the shape of the targets with a sharp variation. Sharp variation means more spectral components. As a result, by increasing the number of antennas, more spectral components are captured by the antennas, leading to a more exact reconstruction of the shapes and especially edges. However, it is demonstrated that the MUDT is not capable of reconstructing the exact shape of the objects with a smooth variation. Increasing the contrast between layers leads to erroneous images provided by the MUDT approach. This is due to neglecting the reflection part of Green's function during the derivation of the object function. A closed-form object function cannot be achieved, by considering the reflected part. It could be concluded that the proposed MUDT imaging algorithm i) is compatible with a low number of antennas to achieve fast data collection and hence reduce the overall cost of the system, ii) provides good spatial resolution, iii) eliminates the need for quantitative imaging algorithm (due to ill-posedness of the problem). The aforementioned points make the proposed combined imaging algorithm suitable for real-time processes.

Next, the TR imaging algorithm is investigated to overcome the problem of high-contrast multilayered media. For testing and validating the proposed algorithm, first, the focus is on a specific static case where it is applied to obtain the location of the moisture in the polymer foam. To formulate the problem, a closed-form Green's function of the multilayered media is obtained using the SPA method and used in the TRI function. The developed TRI is applied to both low and high-contrast media specifically when a low dielectric layer is situated above a PEC layer. Also, the media with a moderately rough surface is investigated as a non-ideal condition. Furthermore, a single frequency SF-TRI is proposed to enable high-speed DAQ from a limited number of antennas; a challenge in many industrial applications of MWT. The frequency for SF-TRI operation is chosen by selecting the frequency where the maximum difference between the dominant eigenvalue and those belonging to the null space exists. The proposed TRI and SF-TRI approach is tested in numerical studies and as well tested on the developed experimental MWT prototype. The results are obtained in less than a second time and show the efficiency of the proposed TRI and SF-TRI algorithm in accurately locating the considered targets under low-contrast and high-contrast media conditions. However, a slight decrease in spatial resolution is noticeable in the SF-TRI method in comparison to the TRI.

A fast optimization algorithm based on the SVD approach is developed by investigating the eigenvalues and eigenvectors of the scattering matrix to obtain the dielectric constant of the localized targets. Simulation and experimental scenarios were performed to examine the capability of the proposed method. It is observed, it can deliver a satisfactory reconstructed value for the dielectric constant of the detected targets. However, by increasing the diameter of the targets in the ROI, the associated error may increase. It is because the proposed method is based on the Born approximation. Different experiments with several values for the dielectric constant of a target inside a multilayered media are performed to investigate the accuracy of the proposed method. An average of $\pm 5.5\,\%$ error in the target percentage can be considered for the proposed algorithm. This error corresponds to the ± 0.16 in the reconstructed dielectric constant.

Appendix A

A.1 Green's function

Consider a plane wave illuminating the interface from above along the propagation direction as follows

$$\hat{k}_i = \frac{1}{k_0}\left(k_{y0}\hat{y} + k_{z0}\hat{z}\right) \tag{A.1}$$

Since there is no variation along $\hat{x}$, therefore, $\frac{\partial}{\partial x}$ of all components are zero. Also, the dependency on z in the n^{th} layer is of $e^{\pm jk_{zn}z}$. For TM to the x (TM_x) waves it can be written

$$\left[\frac{\partial^2}{\partial y^2} + (k_n^2 - k_{zn}^2)\right]H_{zn} = 0, \tag{A.2}$$

where $k_n = \frac{\omega}{c_0}\sqrt{\epsilon_{r,n}}$ and c_0 is the speed of light. Other field components are given by

$$H_{yn} = \frac{1}{k_n^2 - k_{zn}^2}\frac{\partial^2 H_{zn}}{\partial y \partial z}, \tag{A.3}$$

$$E_{xn} = \frac{-j\omega\mu}{k_n^2 - k_{zn}^2}\frac{\partial H_{zn}}{\partial y}. \tag{A.4}$$

Here the incident TE wave is expressed as follows

$$H_z^i = H_0 e^{-jk_{z0}z} e^{-jk_{y0}y}, \tag{A.5}$$

The phase-matching condition demands that the y-dependency of all fields be identical to that of the incident wave. The total field in the layer n is expressed as

$$H_{zn} = \left(\mathcal{A}_n e^{jk_{zn}z} + \mathcal{B}_n e^{-jk_{zn}z}\right)e^{-jk_{y0}y} \tag{A.6}$$

where $\mathcal{A}_n$ and $\mathcal{B}_n$ are the reflection and transmission coefficients of the wave components. Note that $\mathcal{B}_0 = H_0, \mathcal{A}_0 = R^{TM} H_0$, where R^{TM} is the total magnetic field reflection coefficient for TM waves. Since the $(N+1)^{th}$ region is semi-infinite (see Fig. 2.1) and there is no upward traveling wave $\mathcal{A}_{N+1} = 0$ and $\mathcal{B}_{N+1} = T^{TM} H_0$ where T^{TM} is the total transmission coefficient. Now, H_{yn} and E_{xn} should be computed from (A.4) and (A.5), it can be written

$$H_{yn} = \frac{-jk_{y0}}{k_n^2 - k_{zn}^2} jk_{zn}\Big(\mathcal{A}_n e^{jk_{zn}z} - \mathcal{B}_n e^{-jk_{zn}z}\Big), \tag{A.7}$$

$$E_{xn} = \frac{j\omega\mu}{k_n^2 - k_{zn}^2} jk_{y0}\Big(\mathcal{A}_n e^{jk_{zn}}z + \mathcal{B}_n e^{-jk_{zn}z}\Big), \tag{A.8}$$

Enforcing the continuity of tangential electric (A.7) and magnetic (A.8) fields at the interface between the n^{th} and $(n+1)^{\text{th}}$ region gives

$$\begin{aligned} k_{zn}\Big(\mathcal{A}_n e^{-jk_{zn}d_n} - \mathcal{B}_n e^{jk_{zn}d_n}\Big) &= \\ & k_{z(n+1)}\Big(\mathcal{A}_{n+1} e^{-jk_{z(n+1)}d_n} - \mathcal{B}_{n+1} e^{jk_{z(n+1)}d_n}\Big), \end{aligned} \tag{A.9}$$

$$\begin{aligned} k_n\Big(\mathcal{A}_n e^{-jk_{zn}d_n} + \mathcal{B}_n e^{jk_{zn}d_n}\Big) &= \\ & k_{(n+1)}\Big(\mathcal{A}_{n+1} e^{-jk_{z(n+1)}d_n} + \mathcal{B}_{n+1} e^{jk_{z(n+1)}d_n}\Big) \end{aligned} \tag{A.10}$$

There are $N + 2$ regions. Therefore, the number of unknowns are $2N + 2$ ($\mathcal{B}_0$ and $\mathcal{A}_{N+1}$ are known). There are $N + 1$ boundaries and hence $2N + 2$ equations. A simple procedure to solve for unknowns is

- Find R^{TM} by re-cursing relating $\frac{\mathcal{A}_{n+1}}{\mathcal{B}_{n+1}}$ to $\frac{\mathcal{A}_n}{\mathcal{B}_n}$ (Note that $\frac{\mathcal{A}_{N+1}}{\mathcal{B}_{N+1}} = 0$).
- Once $\mathcal{A}_0$ is found relate $\mathcal{A}_{n+1}$ and $\mathcal{B}_{n+1}$ to $\mathcal{A}_n$ and $\mathcal{B}_n$ to find all coefficients.

Using equations (A.9) and (A.10) gives

$$\begin{aligned} \mathcal{A}_n e^{-jk_{zn}d_n} &= \frac{1}{2}\Big[\frac{\mu_{n+1}}{\mu_n} + \frac{k_{z(n+1)}}{k_{zn}}\Big]\times \\ & \Big[\mathcal{A}_{n+1} e^{-jk_{z(n+1)}d_n} + R^{TM}_{n(n+1)} \mathcal{B}_{n+1} e^{jk_{z(n+1)}d_n}\Big] \end{aligned} \tag{A.11}$$

$$\mathcal{B}_n e^{jk_{zn}d_n} = \frac{1}{2}\Big[\frac{\mu_{n+1}}{\mu_n} + \frac{k_{z(n+1)}}{k_{zn}}\Big]\times \\ \Big[R^{TM}_{n(n+1)}\mathcal{A}_{n+1}e^{-jk_{z(n+1)}d_n} + \mathcal{B}_{n+1}e^{jk_{z(n+1)}d_n}\Big] \tag{A.12}$$

where

$$R^{TM}_{n(n+1)} = \frac{\epsilon_{n+1}k_{zn} - \epsilon_n k_{z(n+1)}}{\epsilon_{n+1}k_{zn} + \epsilon_n k_{z(n+1)}} \tag{A.13}$$

is the Fresnel reflection coefficient for a TM_x polarized wave. Taking the relation of $\frac{\mathcal{A}_n}{\mathcal{B}_n}$ provides

$$\frac{\mathcal{A}_n}{\mathcal{B}_n}e^{-2jk_{zn}d_n} = \frac{\Big[\frac{\mathcal{A}_{n+1}}{\mathcal{B}_{n+1}}e^{-2jk_{z(n+1)}d_{n+1}}\Big]e^{2jk_{z(n+1)}(d_{n+1}-d_n)} + r^{TM}_{n(n+1)}}{\Big[\frac{\mathcal{A}_{n+1}}{\mathcal{B}_{n+1}}e^{-2jk_{z(n+1)}d_{n+1}}\Big]e^{2jk_{z(n+1)}(d_{n+1}-d_n)}r^{TM}_{n(n+1)} + 1} \tag{A.14}$$

This is the recursive formula to find $\frac{\mathcal{A}_0}{\mathcal{B}_0}$ starting from $\frac{\mathcal{A}_{N+1}}{\mathcal{B}_{N+1}=0}$ $(\frac{\mathcal{A}_0}{\mathcal{B}_0} = R^{TM})$. In order to solve for T^{TM}, (A.9) and (A.10) are used to relate $\mathcal{A}_{n+1}$ and $\mathcal{B}_{n+1}$ to $\mathcal{A}_n$ and $\mathcal{B}_n$. The relation between transmission and reflection coefficients of the Green's function in layer n in TM_x case can be expressed as

$$\begin{bmatrix} \mathcal{A}_{n+1}e^{+jk_{z(n+1)}d_{(n+1)}} \\ \mathcal{B}_{n+1}e^{-jk_{z(n+1)}d_{(n+1)}} \end{bmatrix} = \bar{\bar{V}}^{TM}_{n(n+1)} \begin{bmatrix} \mathcal{A}_n e^{+jk_{zn}d_n} \\ \mathcal{B}_n e^{-jk_{zn}d_n} \end{bmatrix} \tag{A.15}$$

where

$$\bar{\bar{V}}^{TM}_{n(n+1)} = \frac{1}{2}(1 + \frac{k_{zn}}{k_{z(n+1)}})\times \\ \begin{bmatrix} e^{+jk_{z(n+1)}\Delta d_n} & -R^{TM}_{n(n+1)}e^{+jk_{z(n+1)}\Delta d_n} \\ -R^{TM}_{n(n+1)}e^{-jk_{z(n+1)}\Delta d_n} & e^{-jk_{z(n+1)}\Delta d_n} \end{bmatrix} \tag{A.16}$$

A.2 Quantitative Bayesian Inversion Framework

Consider an inverse problem of identifying an unknown parameter $\varepsilon_r \in \mathbb{C}$ given noisy measurement data $E^{\mathrm{sct}} \in \mathbb{C}$ according to the observation model

$$E^{\mathrm{sct}} = \mathcal{F}(\varepsilon_r) + \xi, \tag{A.17}$$

where $\mathscr{F}\colon \varepsilon_r \to E^{\mathrm{sct}}$ is the forward model as represented by (1), that maps ε_r to the measurement, and ξ denotes the additive measurement noise component. The unknown parameter and noise terms are considered mutually independent. Note that the measurement data and unknown parameters are complex quantities, therefore in the present study, the real and imaginary parts are treated as real variables for the optimization problem.

In the Bayesian framework the unknown parameters are treated as random variables, and information about them is expressed in terms of probability densities. The inverse problem is then expressed as given the measured scattering data, the task is to find the conditional probability density $\pi(\varepsilon_r \mid E^{\mathrm{sct}})$ for the unknown parameter ε_r. The conditional probability density is constructed using Bayes' theorem as

$$\pi(\varepsilon_r \mid E^{\mathrm{sct}}) = \frac{\pi(E^{\mathrm{sct}} \mid \varepsilon_r)\pi(\varepsilon_r)}{\pi(E^{\mathrm{sct}})} \propto \pi(E^{\mathrm{sct}} \mid \varepsilon_r)\pi(\varepsilon_r), \tag{A.18}$$

where $\pi(\varepsilon_r \mid E^{\mathrm{sct}})$ is the posterior density, $\pi(E^{\mathrm{sct}} \mid \varepsilon_r)$ is the likelihood density which represents the distribution of the measured data if ε_r is known, and $\pi(\varepsilon_r)$ is the prior density which contains the prior information available for unknown ε_r. The denominator is the marginal density of the measured data and plays the role of normalization constant. It is often ignored since it requires integration over all possible ε_r.

The likelihood density, if the noise is assumed to be additive Gaussian with zero means with the covariance matrix Γ_ξ, can be written as [13]

$$\pi(E^{\mathrm{sct}} \mid \varepsilon_r) \propto \exp\Big\{-\frac{1}{2}\big(E^{\mathrm{sct}} - \mathscr{F}(\varepsilon_r)\big)^{\top}\Gamma_\xi^{-1} \\ \big(E^{\mathrm{sct}} - \mathscr{F}(\varepsilon_r)\big)\Big\}. \tag{A.19}$$

Furthermore, it can be written in the normal form as

$$\pi(E^{\mathrm{sct}} \mid \varepsilon_r) \propto \exp\left\{-\frac{1}{2}\left\|L_\xi(E^{\mathrm{sct}} - \mathscr{F}(\varepsilon_r))\right\|^2\right\}, \tag{A.20}$$

where L_ξ is the Cholesky factor of the inverse of the noise covariance matrix and $(\cdot)^{\top}$ denotes the transpose operator. As per prior information, it is first assumed that the moisture variation is smooth inside the foam. This indicates that unknowns have a natural neighborhood structure i.e two adjacent values should differ from each other only moderately. Such an assumption can be encoded using a Gaussian prior model [147] with mean η_{ε_r} and covariance Γ_{ε_r} as

$$\begin{aligned}\pi_{\text{smooth}}(\varepsilon_r) &\propto \exp\left\{-\frac{1}{2}(\varepsilon_r - \eta_{\varepsilon_r})^{\mathrm{T}}\Gamma_{\varepsilon_r}^{-1}(\varepsilon_r - \eta_{\varepsilon_r})\right\} \\ &= \exp\left\{-\frac{1}{2}\left\|L_{\varepsilon_r}(\varepsilon_r - \eta_{\varepsilon_r})\right\|^2\right\}. \end{aligned} \tag{A.21}$$

Here, L_{ε_r} is a Cholesky factor of the inverse of the prior covariance matrix Γ_{ε_r}. The prior covariance matrix encodes the spatial smoothness knowledge of the unknowns. The posterior density in (A.18) contains the complete solution of the inverse problem in the Bayesian framework and can be expressed by point estimates. One of the most common point estimates is the *maximum a posteriori* (MAP). The MAP estimate can be computed from the posterior as

$$\widehat{\varepsilon}_{r_{\text{MAP}}} = \arg\max_{\varepsilon_r} \pi(\varepsilon_r \mid E^{\text{sct}}). \tag{A.22}$$

This problem is equivalent to the minimization problem [147], [148],[149]

$$\widehat{\varepsilon}_{r_{\text{MAP}}} = \arg\min_{\varepsilon_r} \{||L_\xi(E^{\text{scat}} - \mathscr{F}(\varepsilon_r))||^2 + ||L_{\varepsilon_r}(\varepsilon_r - \eta_{\varepsilon_r})||^2\}, \tag{A.23}$$

which is a regularized non-linear least square (LS) problem. This minimization problem can be formally solved using a gradient-based optimization method. In the Newton-type method the minimum point is found iteratively by linearizing the forward model, resulting in a linear LS solution in each iteration as

$$\varepsilon_{r_{\ell+1}} = \varepsilon_{r_\ell} + \alpha_\ell A^{-1}B, \tag{A.24}$$

with,

$$A = (J_\ell^T \Gamma_\xi^{-1} J_\ell + \Gamma_{\varepsilon_r}^{-1}), \tag{A.25a}$$

$$B = \left(J_\ell^T \Gamma_\xi^{-1}(E^{\text{sct}} - \mathscr{F}(\varepsilon_{r_\ell})) - \Gamma_{\varepsilon_r}^{-1}(\varepsilon_{r_\ell} - \eta_{\varepsilon_r})\right), \tag{A.25b}$$

where α_ℓ is the step length parameter, index ℓ is the iteration number. The term J is a Jacobian matrix (its derivation can be found in [150]) which is decomposed into real and imaginary parts as

$$J = \begin{bmatrix} J_{\mathbb{R}} & J_{\mathbb{I}} \\ -J_{\mathbb{I}} & J_{\mathbb{R}} \end{bmatrix}_{2S\times 2N_n} \tag{A.26}$$

where S is the total number of measurements and N_n is the total number of unknowns in the cross-section of the foam domain.

Noise model

Let us denote the noise standard deviation (STD) of the real and imaginary parts of the complex-valued scattered field data to be $\sigma_{\mathbb{R}}$ and $\sigma_{\mathbb{I}}$, respectively. Under the assumption that noise between measurement points is independent and not correlated, the noise covariance is then given as

$$\Gamma_\xi = \begin{bmatrix} \sigma_{\mathbb{R}}^2 \odot \mathrm{I}_S & 0_S \\ 0_S & \sigma_{\mathbb{I}}^2 \odot \mathrm{I}_S \end{bmatrix}, \tag{A.27}$$

where I_S is an $S\times S$ identity matrix and 0_S is an $S\times S$ zero matrix and $\odot$ is the Hadamard operator. In the case of real measurements, the noise covariance can be estimated by performing repeated measurements [151].

Smoothness Prior

In this case, the moisture field variation in the entire foam is assumed to be smooth. Here, such a random field [152] is generated using a multivariate Gaussian distribution with anisotropic covariance structure C [153] which can account for the inhomogeneities in the unknown in terms of the characteristic length parameter. In practice, the characteristic length affects the moisture distribution in y, and z-directions. The elements of the covariance C can be calculated as

$$C_{ij} = \exp\left(-\frac{\left\| y_i - y_j \right\|^2}{c_y^2} - \frac{\left\| z_i - z_j \right\|^2}{c_z^2} \right), \tag{A.28}$$

where $i, j = 1, \dots, N_n$ and c_y, c_z are the characteristic lengths (CL) components . If real and imaginary parts of the dielectric constant are assumed uncorrelated, the prior covariance matrix can be written as

$$\Gamma_{\varepsilon_r} = \begin{pmatrix} \Gamma_{\varepsilon_r'} & 0 \\ 0 & \Gamma_{\varepsilon_r''} \end{pmatrix} = \begin{bmatrix} \sigma^2_{\varepsilon_r'} C & 0_{N_n} \\ 0_{N_n} & \sigma^2_{\varepsilon_r''} C \end{bmatrix}_{2N_n \times 2N_n}, \tag{A.29}$$

where 0_{N_n} is an $N_n \times N_n$ zero matrix, and $\sigma_{\varepsilon_r'}$, and $\sigma_{\varepsilon_r''}$ are the standard deviations for the real and imaginary parts of dielectric constant, respectively. Note here that the standard deviation terms control the amplitude of real and imaginary parts of the dielectric constant in the prior covariance matrix. These values can be determined using the dielectric characterization of the foam which is described in detail in [13, 124]. The moisture field variation in terms of the real part of the dielectric constant can be expressed as [123, 154]

$$\varepsilon_r' = \eta_{\varepsilon_r'} 1 + \sigma_{\varepsilon_r'} L Z, \tag{A.30}$$

where 1 is an all-ones vector, L is the lower triangular matrix of the Cholesky factorization of the covariance C, and Z is a standard normal random vector. Similarly, the imaginary part can also be expressed.

List of Figures

Bibliography

[1] M.Pastorino. *Microwave Imaging*. John Wiley & Sons, 2010.

[2] N. K. Nikolova. *Introduction to Microwave Imaging*. EuMA High Frequency Technologies Series. Cambridge University Press, 2017. DOI: 10.1017/9781316084267.

[3] R. Amineh, N. Nikolova, and M. Ravan. *Real-Time Three-Dimensional Imaging of Dielectric Bodies Using Microwave/Millimeter Wave Holography*. IEEE Press Series on RF and Microwave Technology. Wiley, 2019. ISBN: 9781119538844.

[4] M. Ostadrahimi. "Near-Field Microwave Tomography Systems and the Use of a Scatterer Probe Technique". PhD thesis. University of Manitoba, 2011.

[5] M. Amin. *Through-the-Wall Radar Imaging*. CRC Press, 2017. ISBN: 9781439814772.

[6] M. E. Yavuz. "Time reversal based signal processing techniques for ultrawideband electromagnetic sensing in random media". PhD thesis. Ohio State University, 2008.

[7] M. T. Ghasr, M. J. Horst, M. R. Dvorsky, and R. Zoughi. "Wideband Microwave Camera for Real-Time 3-D Imaging". In: *IEEE Transactions on Antennas and Propagation* 65.1 (2017), pp. 258–268. DOI: 10.1109/TAP.2016.2630598.

[8] D. Sheen, D. McMakin, and T. Hall. "Three-dimensional millimeter-wave imaging for concealed weapon detection". In: *IEEE Transactions on Microwave Theory and Techniques* 49.9 (2001), pp. 1581–1592. DOI: 10.1109/22.942570.

[9] S. S. Ahmed, A. Genghammer, A. Schiessl, and L.-P. Schmidt. "Fully Electronic *E*-Band Personnel Imager of 2 m ^{2} Aperture Based on

a Multistatic Architecture". In: *IEEE Transactions on Microwave Theory and Techniques* 61.1 (2013), pp. 651–657. DOI: 10.1109/TMTT.2012.2228221.

[10] E. C. Fear et al. "Microwave Breast Imaging With a Monostatic Radar-Based System: A Study of Application to Patients". In: *IEEE Transactions on Microwave Theory and Techniques* 61.5 (2013), pp. 2119–2128. DOI: 10.1109/TMTT.2013.2255884.

[11] M. Richards, J. Scheer, J. Scheer, and W. Holm. *Principles of Modern Radar: Basic Principles, Volume 1*. Electromagnetics and Radar. Institution of Engineering and Technology, 2010. ISBN: 9781891121524.

[12] K. Ren and R. J. Burkholder. "A 3-D Novel Fast Back-Projection Imaging Algorithm for Stratified Media Based on Near-Field Monostatic and Bistatic SAR". In: *IEEE Transactions on Antennas and Propagation* 69.4 (2021), pp. 2326–2335. DOI: 10.1109/TAP.2020.3026920.

[13] R. Yadav, A. Omrani, G. Link, M. Vauhkonen, and T. Lähivaara. "Correlated Sample-Based Prior in Bayesian Inversion Framework for Microwave Tomography". In: *IEEE Transactions on Antennas and Propagation* 70.7 (2022), pp. 5860–5872. DOI: 10.1109/TAP.2022.3145433.

[14] M. Dehmollaian and K. Sarabandi. "Refocusing Through Building Walls Using Synthetic Aperture Radar". In: *IEEE Transactions on Geoscience and Remote Sensing* 46.6 (2008), pp. 1589–1599. DOI: 10.1109/TGRS.2008.916212.

[15] F. M. Saraskanroud and I. Jeffrey. "A Comparison of Time-Domain and Frequency-Domain Microwave Imaging of Experimental Targets". In: *IEEE Transactions on Computational Imaging* 7 (2021), pp. 611–623. DOI: 10.1109/TCI.2021.3089464.

[16] W. Chew and Y. Wang. "Reconstruction of two-dimensional permittivity distribution using the distorted Born iterative method". In: *IEEE Transactions on Medical Imaging* 9.2 (1990), pp. 218–225. DOI: 10.1109/42.56334.

[17] S. Caorsi, G. Gragnani, and M. Pastorino. “Two-dimensional microwave imaging by a numerical inverse scattering solution”. In: *IEEE Transactions on Microwave Theory and Techniques* 38.8 (1990), pp. 981–980. DOI: 10.1109/22.57321.

[18] A. Franchois and C. Pichot. “Microwave imaging-complex permittivity reconstruction with a Levenberg-Marquardt method”. In: *IEEE Transactions on Antennas and Propagation* 45.2 (1997), pp. 203–215. DOI: 10.1109/8.560338.

[19] X. Zeng, A. Fhager, M. Persson, P. Linner, and H. Zirath. “Accuracy Evaluation of Ultrawideband Time Domain Systems for Microwave Imaging”. In: *IEEE Transactions on Antennas and Propagation* 59.11 (2011), pp. 4279–4285. DOI: 10.1109/TAP.2011.2164174.

[20] X. Zeng, A. Fhager, P. Linner, M. Persson, and H. Zirath. “Experimental Investigation of the Accuracy of an Ultrawideband Time-Domain Microwave-Tomographic System”. In: *IEEE Transactions on Instrumentation and Measurement* 60.12 (2011), pp. 3939–3949. DOI: 10.1109/TIM.2011.2141250.

[21] A. S. M. Alqadami, K. S. Bialkowski, A. T. Mobashsher, and A. M. Abbosh. “Wearable Electromagnetic Head Imaging System Using Flexible Wideband Antenna Array Based on Polymer Technology for Brain Stroke Diagnosis”. In: *IEEE Transactions on Biomedical Circuits and Systems* 13.1 (2019), pp. 124–134. DOI: 10.1109/TBCAS.2018.2878057.

[22] X. Li and S. Hagness. “A confocal microwave imaging algorithm for breast cancer detection”. In: *IEEE Microwave and Wireless Components Letters* 11.3 (2001), pp. 130–132. DOI: 10.1109/7260.915627.

[23] P. M. Meaney et al. “Clinical Microwave Tomographic Imaging of the Calcaneus: A First-in-Human Case Study of Two Subjects”. In: *IEEE Transactions on Biomedical Engineering* 59.12 (2012), pp. 3304–3313. DOI: 10.1109/TBME.2012.2209202.

[24] S. Takahashi, K. Suzuki, T. Hanabusa, and S. Kidera. “Microwave Subsurface Imaging Method by Incorporating Radar and Tomographic Approaches”. In: *IEEE Transactions on Antennas and Propagation* 70.11 (2022), pp. 11009–11023. DOI: 10.1109/TAP.2022.3188358.

[25] W. Zhang and A. Hoorfar. “MIMO Ground Penetrating Radar Imaging Through Multilayered Subsurface Using Total Variation Minimization”. In: *IEEE Transactions on Geoscience and Remote Sensing* 57.4 (2019), pp. 2107–2115. DOI: 10.1109/TGRS.2018.2871463.

[26] M. García Fernández et al. “Synthetic Aperture Radar Imaging System for Landmine Detection Using a Ground Penetrating Radar on Board a Unmanned Aerial Vehicle”. In: *IEEE Access* 6 (2018), pp. 45100–45112. DOI: 10.1109/ACCESS.2018.2863572.

[27] V. Khorashadi-Zadeh and M. Dehmollaian. “Through a Cinder Block Wall Refocusing Using SAR Back Projection Method”. In: *IEEE Transactions on Antennas and Propagation* 67.2 (2019), pp. 1212–1222. DOI: 10.1109/TAP.2018.2882599.

[28] Y.-S. Yoon and M. G. Amin. “High-Resolution Through-the-Wall Radar Imaging Using Beamspace MUSIC”. In: *IEEE Transactions on Antennas and Propagation* 56.6 (2008), pp. 1763–1774. DOI: 10.1109/TAP.2008.923336.

[29] C. Zhang, Y. Kuga, and A. Ishimaru. “Hard-Wall Radar Imaging: Localization of Objects Shadowed by Metallic Walls With MIMO Radar”. In: *IEEE Transactions on Antennas and Propagation* 66.8 (2018), pp. 4240–4251. DOI: 10.1109/TAP.2018.2835569.

[30] G. N. Jawad and M. F. Akbar. “IFFT-Based Microwave Non-Destructive Testing for Delamination Detection and Thickness Estimation”. In: *IEEE Access* 9 (2021), pp. 98561–98572. DOI: 10.1109/ACCESS.2021.3095105.

[31] T. Merkle et al. “Broadband 240-GHz Radar for Non-Destructive Testing of Composite Materials”. In: *IEEE Journal of Solid-State Circuits* 54.9 (2019), pp. 2388–2401. DOI: 10.1109/JSSC.2019.2921154.

[32] B. Yektakhah and K. Sarabandi. “A Method for Detection of Flat Walls in Through-the-Wall SAR Imaging”. In: *IEEE Geoscience and Remote Sensing Letters* 18.12 (2021), pp. 2102–2106. DOI: 10.1109/LGRS.2020.3014582.

[33] H. Abedi and B. Zakeri. “Through-the-Multilayered Wall Imaging Using Passive Synthetic Aperture Radar”. In: *IEEE Transactions on Geoscience and Remote Sensing* 57.7 (2019), pp. 4181–4191. DOI: 10.1109/TGRS.2018.2890027.

[34] F. H. C. Tivive and A. Bouzerdoum. “Toward Moving Target Detection in Through-the-Wall Radar Imaging”. In: *IEEE Transactions on Geoscience and Remote Sensing* 59.3 (2021), pp. 2028–2040. DOI: 10.1109/TGRS.2020.3005199.

[35] Z. Zheng, D. Zhang, X. Liang, X. Liu, and G. Fang. “Through-Wall Human Pose Reconstruction Based on Cross-Modal Learning and Self-Supervised Learning”. In: *IEEE Geoscience and Remote Sensing Letters* 19 (2022), pp. 1–5. DOI: 10.1109/LGRS.2022.3215729.

[36] R. Persico. *Introduction to ground penetrating radar: inverse scattering and data processing*. John Wiley & Sons, 2014.

[37] X. Zhou, Q. Chen, B. Jiang, and H. Chen. “An Underground Pipeline Mapping Method Based on Fusion of Multisource Data”. In: *IEEE Transactions on Geoscience and Remote Sensing* 60 (2022), pp. 1–11. DOI: 10.1109/TGRS.2022.3200153.

[38] X. Xu, E. Miller, and C. Rappaport. “Minimum entropy regularization in frequency-wavenumber migration to localize subsurface objects”. In: *IEEE Transactions on Geoscience and Remote Sensing* 41.8 (2003), pp. 1804–1812. DOI: 10.1109/TGRS.2003.813497.

[39] W. Zhao et al. “Advances in GPR data acquisition and analysis for archaeology”. In: *Geophysical Journal International* 202.1 (2015), pp. 62–71. DOI: 10.1093/gji/ggv121.

[40] B. J. Mohammed, A. M. Abbosh, S. Mustafa, and D. Ireland. “Microwave System for Head Imaging”. In: *IEEE Transactions on Instrumentation and Measurement* 63.1 (2014), pp. 117–123. DOI: 10.1109/TIM.2013.2277562.

[41] M. Pinheiro, P. Prats, R. Scheiber, M. Nannini, and A. Reigber. “Tomographic 3D reconstruction from airborne circular SAR”. In: *2009 IEEE International Geoscience and Remote Sensing Symposium*. Vol. 3. 2009, pp. III–21–III–24. DOI: 10.1109/IGARSS.2009.5418239.

[42] M. Jäger, M. Pinheiro, O. Ponce, A. Reigber, and R. Scheiber. “A Survey of novel airborne SAR signal processing techniques and applications for DLR’s F-SAR sensor”. In: *2015 16th International Radar Symposium (IRS)*. 2015, pp. 236–241. DOI: 10.1109/IRS.2015.7226358.

[43] G. Vasile et al. “High-Resolution SAR Interferometry: Estimation of Local Frequencies in the Context of Alpine Glaciers”. In: *IEEE Transactions on Geoscience and Remote Sensing* 46.4 (2008), pp. 1079–1090. DOI: 10.1109/TGRS.2007.912713.

[44] H. Been Lim, N. Thi Tuyet Nhung, E.-P. Li, and N. Duc Thang. “Confocal Microwave Imaging for Breast Cancer Detection: Delay-Multiply-and-Sum Image Reconstruction Algorithm”. In: *IEEE Transactions on Biomedical Engineering* 55.6 (2008), pp. 1697–1704. DOI: 10.1109/TBME.2008.919716.

[45] T. M. Grzegorczyk, P. M. Meaney, P. A. Kaufman, R. M. diFlorio Alexander, and K. D. Paulsen. “Fast 3-D Tomographic Microwave Imaging for Breast Cancer Detection”. In: *IEEE Transactions on Medical Imaging* 31.8 (2012), pp. 1584–1592. DOI: 10.1109/TMI.2012.2197218.

[46] P. M. Meaney et al. “3D Microwave bone imaging”. In: *2012 6th European Conference on Antennas and Propagation (EUCAP)*. 2012, pp. 1770–1771. DOI: 10.1109/EuCAP.2012.6206024.

[47] A. E. Stancombe, K. S. Bialkowski, and A. M. Abbosh. “Portable Microwave Head Imaging System Using Software-Defined Radio

and Switching Network”. In: *IEEE Journal of Electromagnetics, RF and Microwaves in Medicine and Biology* 3.4 (2019), pp. 284–291. DOI: 10.1109/JERM.2019.2901360.

[48] G. Roussy, A. Bennani, and J. Thiebaut. “Temperature runaway of microwave irradiated materials”. In: *Journal of Applied Physics* 62.4 (1987), pp. 1167–1170. DOI: 10.1063/1.339666.

[49] Z. Li, G. Raghavan, and V. Orsat. “Temperature and power control in microwave drying”. In: *Journal of Food Engineering* 97.4 (2010), pp. 478–483. ISSN: 0260-8774. DOI: https://doi.org/10.1016/j.jfoodeng.2009.11.004.

[50] A. Martynenko and A. Buck. *Intelligent Control in Drying*. Boca Raton (Fla.): CRC press, 2019.

[51] M. Mehdizadeh. *Microwave/RF Applicators and Probes*. Second Edition. Boston: William Andrew Publishing, 2015. ISBN: 978-0-323-32256-0. DOI: https://doi.org/10.1016/B978-0-323-32256-0.00001-4.

[52] Y. Sun. “Adaptive and Intelligent Temperature Control of Microwave Heating Systems with Multiple Sources”. PhD thesis. KIT Scientific Publishing, Karlsruhe, 2016.

[53] G. Link and V. Ramopoulos. “Simple analytical approach for industrial microwave applicator design”. In: *Chemical Engineering and Processing - Process Intensification* 125 (2018), pp. 334–342.

[54] D. L. Colton, R. Kress, and R. Kress. *Inverse acoustic and electromagnetic scattering theory*. Vol. 93. Springer, 1998.

[55] W. Chew and Y. Wang. “Reconstruction of two-dimensional permittivity distribution using the distorted Born iterative method”. In: *IEEE Transactions on Medical Imaging* 9.2 (1990), pp. 218–225. DOI: 10.1109/42.56334.

[56] X. Chen. “Application of signal-subspace and optimization methods in reconstructing extended scatterers”. In: *J. Opt. Soc. Am. A* 26.4 (2009), pp. 1022–1026. DOI: 10.1364/JOSAA.26.001022.

[57] P. M. van den Berg and R. E. Kleinman. “A contrast source inversion method”. In: *Inverse Problems* 13.6 (1997), p. 1607. DOI: 10.1088/0266-5611/13/6/013.

[58] I. Cumming and F. Wong. *Digital Processing of Synthetic Aperture Radar Data: Algorithms and Implementation*. Artech House remote sensing library v. 1. Artech House, 2005. ISBN: 9781580530583.

[59] M. Dehmollaian, M. Thiel, and K. Sarabandi. “Through-the-Wall Imaging Using Differential SAR”. In: *IEEE Transactions on Geoscience and Remote Sensing* 47.5 (2009), pp. 1289–1296. DOI: 10.1109/TGRS.2008.2010052.

[60] M. Fink. “Time reversal of ultrasonic fields. I. Basic principles”. In: *IEEE Transactions on Ultrasonics, Ferroelectrics, and Frequency Control* 39.5 (1992), pp. 555–566. DOI: 10.1109/58.156174.

[61] J. Ebrahimi-Zadeh, M. Dehmollaian, and K. Mohammadpour-Aghdam. “Electromagnetic Time-Reversal Imaging of Pinholes in Pipes”. In: *IEEE Transactions on Antennas and Propagation* 64.4 (2016), pp. 1356–1363. DOI: 10.1109/TAP.2016.2526043.

[62] M. Yavuz and F. Teixeira. “Full time-domain DORT for ultrawideband electromagnetic fields in dispersive, random inhomogeneous media”. In: *IEEE Transactions on Antennas and Propagation* 54.8 (2006), pp. 2305–2315. DOI: 10.1109/TAP.2006.879196.

[63] M. E. Yavuz and F. L. Teixeira. “Space–Frequency Ultrawideband Time-Reversal Imaging”. In: *IEEE Transactions on Geoscience and Remote Sensing* 46.4 (2008), pp. 1115–1124. DOI: 10.1109/TGRS.2008.915755.

[64] A. Omrani, M. Moghadasi, and M. Dehmollaian. “Localisation and permittivity extraction of an embedded cylinder using decomposition of the time reversal operator”. In: *IET Microwaves, Antennas & Propagation* (2020).

[65] W. Zhang and A. Hoorfar. "Three-Dimensional Real-Time Through-the-Wall Radar Imaging With Diffraction Tomographic Algorithm". In: *IEEE Transactions on Geoscience and Remote Sensing* 51.7 (2013), pp. 4155–4163. DOI: 10.1109/TGRS.2012.2227059.

[66] J. Bolomey et al. "Microwave Diffraction Tomography for Biomedical Applications". In: *IEEE Transactions on Microwave Theory and Techniques* 30.11 (1982), pp. 1998–2000. DOI: 10.1109/TMTT.1982.1131357.

[67] T.-H. Chu and K.-Y. Lee. "Wide-band microwave diffraction tomography under Born approximation". In: *IEEE Transactions on Antennas and Propagation* 37.4 (1989), pp. 515–519. DOI: 10.1109/8.24174.

[68] T. Hansen and P. Johansen. "Inversion scheme for ground penetrating radar that takes into account the planar air-soil interface". In: *IEEE Transactions on Geoscience and Remote Sensing* 38.1 (2000), pp. 496–506. DOI: 10.1109/36.823944.

[69] K. Belkebir, R. Kleinman, and C. Pichot. "Microwave imaging-Location and shape reconstruction from multifrequency scattering data". In: *IEEE Transactions on Microwave Theory and Techniques* 45.4 (1997), pp. 469–476. DOI: 10.1109/22.566625.

[70] J. Justice, A. Vassiliou, and D. Nguyen. "Geophysical diffraction tomography". In: *Signal Processing* 15.3 (1988). Multidimensional Sugnal Processing, pp. 227–235. ISSN: 0165-1684. DOI: https://doi.org/10.1016/0165-1684(88)90013-8.

[71] A. J. Devaney. "Geophysical Diffraction Tomography". In: *IEEE Transactions on Geoscience and Remote Sensing* GE-22.1 (1984), pp. 3–13. DOI: 10.1109/TGRS.1984.350573.

[72] E. Wolf. "Three-dimensional structure determination of semi transparent objects from holographic data". In: *Optics Communications* 1.4 (1969), pp. 153–156. ISSN: 0030-4018. DOI: https://doi.org/10.1016/0030-4018(69)90052-2.

[73] E. Wolf. “Determination of the Amplitude and the Phase of Scattered Fields by Holography$*$”. In: *J. Opt. Soc. Am.* 60.1 (1970), pp. 18–20. DOI: 10.1364/JOSA.60.000018.

[74] C. Pichot, L. Jofre, G. Peronnet, and J. Bolomey. “Active microwave imaging of inhomogeneous bodies”. In: *IEEE Transactions on Antennas and Propagation* 33.4 (1985), pp. 416–425. DOI: 10.1109/TAP.1985.1143603.

[75] W Tabbara et al. “Diffraction tomography: contribution to the analysis of some applications in microwaves and ultrasonics”. In: *Inverse Problems* 4.2 (1988), p. 305. DOI: 10.1088/0266-5611/4/2/001.

[76] P. Meincke. “Linear GPR inversion for lossy soil and a planar air-soil interface”. In: *IEEE Transactions on Geoscience and Remote Sensing* 39.12 (2001), pp. 2713–2721. DOI: 10.1109/36.975005.

[77] K. Ren and R. J. Burkholder. “A Uniform Diffraction Tomographic Imaging Algorithm for Near-Field Microwave Scanning Through Stratified Media”. In: *IEEE Transactions on Antennas and Propagation* 64.12 (2016), pp. 5198–5207. DOI: 10.1109/TAP.2016.2617358.

[78] S. Sadeghi, K. Mohammadpour-Aghdam, R. Faraji-Dana, and R. J. Burkholder. “A DORT-Uniform Diffraction Tomography Algorithm for Through-the-Wall Imaging”. In: *IEEE Transactions on Antennas and Propagation* 68.4 (2020), pp. 3176–3183. DOI: 10.1109/TAP.2019.2952002.

[79] S. Sadeghi, K. Mohammadpour-Aghdam, K. Ren, R. Faraji-Dana, and R. J. Burkholder. “A Pole-Extraction Algorithm for Wall Characterization in Through-the-Wall Imaging Systems”. In: *IEEE Transactions on Antennas and Propagation* 67.11 (2019), pp. 7106–7113. DOI: 10.1109/TAP.2019.2927870.

[80] F. Wu, J.-L. Thomas, and M. Fink. “Time reversal of ultrasonic fields. Il. Experimental results”. In: *IEEE Transactions on Ultrasonics, Ferroelectrics, and Frequency Control* 39.5 (1992), pp. 567–578. DOI: 10.1109/58.156175.

[81] D. Cassereau and M. Fink. “Time-reversal of ultrasonic fields. III. Theory of the closed time-reversal cavity”. In: *IEEE Transactions on Ultrasonics, Ferroelectrics, and Frequency Control* 39.5 (1992), pp. 579–592. DOI: 10.1109/58.156176.

[82] M. E. Yavuz and F. L. Teixeira. “Space–Frequency Ultrawideband Time-Reversal Imaging”. In: *IEEE Transactions on Geoscience and Remote Sensing* 46.4 (2008), pp. 1115–1124. DOI: 10.1109/TGRS.2008.915755.

[83] A. E. Fouda, F. L. Teixeira, and M. E. Yavuz. “Imaging and tracking of targets in clutter using differential time-reversal”. In: *Proceedings of the 5th European Conference on Antennas and Propagation (EUCAP).* 2011, pp. 569–573.

[84] C. Prada, F. Wu, and M. Fink. “The iterative time reversal mirror: A solution to self-focusing in the pulse echo mode”. In: *The Journal of the Acoustical Society of America* 90.2 (1991), pp. 1119–1129. DOI: 10.1121/1.402301.

[85] C. Prada and M. Fink. “Eigenmodes of the time reversal operator: A solution to selective focusing in multiple-target media”. In: *Wave Motion* 20.2 (1994), pp. 151–163. ISSN: 0165-2125. DOI: https://doi.org/10.1016/0165-2125(94)90039-6.

[86] J. Stang, M. Haynes, P. Carson, and M. Moghaddam. “A Preclinical System Prototype for Focused Microwave Thermal Therapy of the Breast”. In: *IEEE Transactions on Biomedical Engineering* 59.9 (2012), pp. 2431–2438. DOI: 10.1109/TBME.2012.2199492.

[87] J.-L. Thomas, F. Wu, and M. Fink. “Time Reversal Focusing Applied to Lithotripsy”. In: *Ultrasonic Imaging* 18.2 (1996), pp. 106–121. ISSN: 0161-7346. DOI: https://doi.org/10.1006/uimg.1996.0006.

[88] P. L. Bas, K. V. D. Abeele, S. D. Santos, T. Goursolle, and O. Matar. “Experimental Analysis for Nonlinear Time Reversal Imaging of Damaged Materials”. In: (2006).

[89] M. E. Yavuz and F. L. Teixeira. “On the Sensitivity of Time-Reversal Imaging Techniques to Model Perturbations”. In: *IEEE Transactions on Antennas and Propagation* 56.3 (2008), pp. 834–843. DOI: 10.1109/TAP.2008.916933.

[90] S. M. Moghadasi and M. Dehmollaian. “Buried-Object Time-Reversal Imaging Using UWB Near-Ground Scattered Fields”. In: *IEEE Transactions on Geoscience and Remote Sensing* 52.11 (2014), pp. 7317–7326. DOI: 10.1109/TGRS.2014.2311131.

[91] S. M. Moghadasi, M. Dehmollaian, and J. Rashed-Mohassel. “Time Reversal Imaging of Deeply Buried Targets Under Moderately Rough Surfaces Using Approximate Transmitted Fields”. In: *IEEE Transactions on Geoscience and Remote Sensing* 53.7 (2015), pp. 3897–3905. DOI: 10.1109/TGRS.2014.2387280.

[92] S. Sadeghi, K. Mohammadpour-Aghdam, R. Faraji-Dana, and R. J. Burkholder. “A Novel Algorithm for Wall Characterization in Through the wall Imaging based on Spectral Analysis”. In: *2018 18th International Symposium on Antenna Technology and Applied Electromagnetics (ANTEM)*. 2018, pp. 1–2. DOI: 10.1109/ANTEM.2018.8572991.

[93] A. Omrani, G. Link, and J. Jelonnek. “A Multistatic Uniform Diffraction Tomographic Algorithm for Real-Time Moisture Detection”. In: *2020 IEEE Asia-Pacific Microwave Conference (APMC)*. 2020, pp. 437–439. DOI: 10.1109/APMC47863.2020.9331603.

[94] W. C. Chew. *Waves and Fields in Inhomogenous Media*. IEEE Press, 1995.

[95] C. T. Tai. *Dyadic Green’s functions in electromagnetic theory*. IEEE Press, 1994.

[96] J. A. Stratton. *Electromagnetic theory*. Vol. 33. John Wiley & Sons, 2007.

[97] P. Zhang, X. Zhang, and G. Fang. “Comparison of the Imaging Resolutions of Time Reversal and Back-Projection Algorithms in EM

Inverse Scattering". In: *IEEE Geoscience and Remote Sensing Letters* 10.2 (2013), pp. 357–361. DOI: 10.1109/LGRS.2012.2206012.

[98] R. F. Harrington. *Field Computation by Moment Methods*. Wiley-IEEE Press, 1993. ISBN: 0780310144.

[99] K. Sarabandi. "Electromagnetic Scattering from Vegetation Canopies." PhD thesis. University of Michigan, Jan. 1989.

[100] "Scattering and Emission by Layered Media". In: *Scattering of Electromagnetic Waves: Theories and Applications*. John Wiley Sons, Ltd, 2000. Chap. 5, pp. 199–229. ISBN: 9780471224280. DOI: https://doi.org/10.1002/0471224286.ch5.

[101] V. Khorashadi-Zadeh, A. Omrani, and M. Dehmollaian. "Scattered Fields of a 2-D Rectangular Room Composed of Cinder Block Walls Using Floquet–Fourier Series Expansion". In: *IEEE Transactions on Antennas and Propagation* 67.1 (2019), pp. 390–399. DOI: 10.1109/TAP.2018.2880029.

[102] R. A. H. Norman Bleistein. *Asymptotic Expansions of Integrals*. Holt, Rinehart and Winston, 1975.

[103] C. M. Bender and S. A. Orszag. "Asymptotic Expansion of Integrals". In: *Advanced Mathematical Methods for Scientists and Engineers I: Asymptotic Methods and Perturbation Theory*. New York, NY: Springer New York, 1999, pp. 247–316.

[104] K. Ren and R. J. Burkholder. "A Uniform Diffraction Tomographic Imaging Algorithm for Near-Field Microwave Scanning Through Stratified Media". In: *IEEE Transactions on Antennas and Propagation* 64.12 (2016), pp. 5198–5207.

[105] M. Kazemi, Z. Kavehvash, and M. Shabany. "K-Space Analysis of Aliasing in Millimeter-Wave Imaging Systems". In: *IEEE Transactions on Microwave Theory and Techniques* 69.3 (2021), pp. 1965–1973. DOI: 10.1109/TMTT.2021.3053238.

[106] M. Kazemi, Z. Kavehvash, and M. Shabany. “K-Space Aware Multi-Static Millimeter-Wave Imaging”. In: *IEEE Transactions on Image Processing* 28.7 (2019), pp. 3613–3623. DOI: 10.1109/TIP.2019.2900588.

[107] Y. Álvarez, Y. Rodriguez-Vaqueiro, B. Gonzalez-Valdes, F. Las-Heras, and A. García-Pino. “Fourier-Based Imaging for Subsampled Multistatic Arrays”. In: *IEEE Transactions on Antennas and Propagation* 64.6 (2016), pp. 2557–2562. DOI: 10.1109/TAP.2016.2550035.

[108] G. Lockwood, P.-C. Li, M. O’Donnell, and F. Foster. “Optimizing the radiation pattern of sparse periodic linear arrays”. In: *IEEE Transactions on Ultrasonics, Ferroelectrics, and Frequency Control* 43.1 (1996), pp. 7–14. DOI: 10.1109/58.484457.

[109] S. M. Gehlbach and R. E. Alvarez. “Digital Ultrasound Imaging Techniques Using Vector Sampling and Raster Line Reconstruction”. In: *Ultrasonic Imaging* 3.1 (1981). PMID: 7195096, pp. 83–107. DOI: 10.1177/016173468100300104.

[110] S. S. Ahmed et al. “Advanced Microwave Imaging”. In: *IEEE Microwave Magazine* 13.6 (2012), pp. 26–43. DOI: 10.1109/MMM.2012.2205772.

[111] W. Chew and Y. Wang. “Reconstruction of two-dimensional permittivity distribution using the distorted Born iterative method”. In: *IEEE Transactions on Medical Imaging* 9.2 (1990), pp. 218–225. DOI: 10.1109/42.56334.

[112] B. J. Mohammed, A. M. Abbosh, S. Mustafa, and D. Ireland. “Microwave System for Head Imaging”. In: *IEEE Transactions on Instrumentation and Measurement* 63.1 (2014), pp. 117–123. DOI: 10.1109/TIM.2013.2277562.

[113] M. Bialkowski, D. Ireland, Y. Wang, and A. Abbosh. “Ultra-wideband array antenna system for breast imaging”. In: *2010 Asia-Pacific Microwave Conference*. 2010, pp. 267–270.

[114] M. Klemm, I. J. Craddock, J. A. Leendertz, A. Preece, and R. Benjamin. “Radar-Based Breast Cancer Detection Using a Hemispherical Antenna Array—Experimental Results”. In: *IEEE Transactions on Antennas and Propagation* 57.6 (2009), pp. 1692–1704. DOI: 10.1109/TAP.2009.2019856.

[115] C. Gilmore et al. “A Wideband Microwave Tomography System With a Novel Frequency Selection Procedure”. In: *IEEE Transactions on Biomedical Engineering* 57.4 (2010), pp. 894–904. DOI: 10.1109/TBME.2009.2036372.

[116] M. T. Ghasr, D. Simms, and R. Zoughi. “Multimodal Solution for a Waveguide Radiating Into Multilayered Structures—Dielectric Property and Thickness Evaluation”. In: *IEEE Transactions on Instrumentation and Measurement* 58.5 (2009), pp. 1505–1513. DOI: 10.1109/TIM.2008.2009133.

[117] C.-W. Chang, K.-M. Chen, and J. Qian. “Nondestructive determination of electromagnetic parameters of dielectric materials at X-band frequencies using a waveguide probe system”. In: *IEEE Transactions on Instrumentation and Measurement* 46.5 (1997), pp. 1084–1092. DOI: 10.1109/19.676717.

[118] P. Mojabi, M. Ostadrahimi, L. Shafai, and J. LoVetri. “Microwave tomography techniques and algorithms: A review”. In: *2012 15 International Symposium on Antenna Technology and Applied Electromagnetics*. 2012, pp. 1–4. DOI: 10.1109/ANTEM.2012.6262367.

[119] L. Zhang et al. “Learning-Based Quantitative Microwave Imaging With a Hybrid Input Scheme”. In: *IEEE Sensors Journal* 20.24 (2020), pp. 15007–15013. DOI: 10.1109/JSEN.2020.3012177.

[120] A. Massa, D. Marcantonio, X. Chen, M. Li, and M. Salucci. “DNNs as Applied to Electromagnetics, Antennas, and Propagation—A Review”. In: *IEEE Antennas and Wireless Propagation Letters* 18.11 (2019), pp. 2225–2229. DOI: 10.1109/LAWP.2019.2916369.

[121] L.-Y. Xiao et al. “Super-Resolution 3-D Microwave Imaging of Objects With High Contrasts by a Semijoin Extreme Learning Machine”. In: *IEEE Transactions on Microwave Theory and Techniques* (2021), pp. 1–1. DOI: 10.1109/TMTT.2021.3100421.

[122] T. Lähivaara, R. Yadav, G. Link, and M. Vauhkonen. “Estimation of Moisture Content Distribution in Porous Foam Using Microwave Tomography With Neural Networks”. In: *IEEE Transactions on Computational Imaging* 6 (2020), pp. 1351–1361.

[123] R. Yadav, A. Omrani, G. Link, M. Vauhkonen, and T. Lähivaara. “Microwave Tomography Using Neural Networks for Its Application in an Industrial Microwave Drying System”. In: *Sensors* 21.20 (2021). ISSN: 1424-8220. DOI: 10.3390/s21206919.

[124] S. Soldatov et al. “Microwave cavity perturbation technique for high-temperature dielectric measurements”. In: *2013 IEEE MTT-S International Microwave Symposium Digest (MTT)*. 2013, pp. 1–4. DOI: 10.1109/MWSYM.2013.6697793.

[125] A. Omrani, R. Yadav, G. Link, and J. Jelonnek. “A Multistatic Uniform Diffraction Tomography Algorithm for Microwave Imaging in Multilayered Media for Microwave Drying”. In: *IEEE Transactions on Antennas and Propagation* 70.10 (2022), pp. 9583–9595. DOI: 10.1109/TAP.2022.3177495.

[126] H.-O. Peitgen and D. Saupe, eds. *The Science of Fractal Images*. Berlin, Heidelberg: Springer-Verlag, 1988. ISBN: 0387966080.

[127] C. Moss, F. Teixeira, Y. Yang, and J. A. Kong. “Finite-difference time-domain simulation of scattering from objects in continuous random media”. In: *IEEE Transactions on Geoscience and Remote Sensing* 40.1 (2002), pp. 178–186. DOI: 10.1109/36.981359.

[128] L. Tsang and J. A. Kong. *Scattering of Electromagnetic Waves: Advanced Topics*. John Wiley & Sons, Ltd, 2001. ISBN: 9780471224273.

[129] D. Liu et al. “Electromagnetic time-reversal imaging of a target in a cluttered environment”. In: *IEEE Transactions on Antennas and Propagation* 53.9 (2005), pp. 3058–3066. DOI: 10.1109/TAP.2005.854563.

[130] S. M. Moghadasi, M. Dehmollaian, and J. Rashed-Mohassel. “Time Reversal Imaging of Deeply Buried Targets Under Moderately Rough Surfaces Using Approximate Transmitted Fields”. In: *IEEE Transactions on Geoscience and Remote Sensing* 53.7 (2015), pp. 3897–3905.

[131] A. J. Devaney and M. Dennison. “Inverse scattering in inhomogeneous background media”. In: 19.4 (2003), pp. 855–870. DOI: 10.1088/0266-5611/19/4/305.

[132] S. Kim et al. “Spatial resolution of time-reversal arrays in shallow water”. In: *The Journal of the Acoustical Society of America* 110.2 (2001), pp. 820–829. DOI: 10.1121/1.1382619.

[133] M. E. Yavuz and F. L. Teixeira. “Ultrawideband Microwave Sensing and Imaging Using Time-Reversal Techniques: A Review”. In: *Remote Sensing* 1.3 (2009), pp. 466–495. ISSN: 2072-4292. DOI: 10.3390/rs1030466.

[134] R. C. Janalizadeh and B. Zakeri. “A Source-Type Best Approximation Method for Imaging Applications”. In: *IEEE Antennas and Wireless Propagation Letters* 15 (2016), pp. 1707–1710. DOI: 10.1109/LAWP.2016.2527828.

[135] D. Liu, S. Vasudevan, J. Krolik, G. Bal, and L. Carin. “Electromagnetic Time-Reversal Source Localization in Changing Media: Experiment and Analysis”. In: *IEEE Transactions on Antennas and Propagation* 55.2 (2007), pp. 344–354. DOI: 10.1109/TAP.2006.889807.

[136] A. Borsic, W. Lionheart, and C. McLeod. “Generation of anisotropic-smoothness regularization filters for EIT”. In: *IEEE Transactions on Medical Imaging* 21.6 (2002), pp. 579–587. DOI: 10.1109/TMI.2002.800611.

[137] J. Kaipio, V. Kolehmainen, M. Vauhkonen, and E. Somersalo. “Inverse problems with structural prior information”. In: *Inverse Problems* 15.3 (1999), p. 713.

[138] A. Omrani et al. “A combined microwave imaging algorithm for localization and moisture level estimation in multilayered media”. In: *2021 15th European Conference on Antennas and Propagation (EuCAP)*. 2021, pp. 1–5. DOI: 10.23919/EuCAP48036.2020.9135296.

[139] D. Calvetti and E. Somersalo. “Inverse problems: From regularization to Bayesian inference”. In: *WIREs Computational Statistics* 10.3 (2018), e1427. DOI: https://doi.org/10.1002/wics.1427.

[140] P. Meaney et al. “Integration of microwave tomography with magnetic resonance for improved breast imaging”. In: *Medical physics* 40 (10 2013), p. 103101. DOI: 10.1118/1.4820361.

[141] N. Bayat and P. Mojabi. “Incorporating Spatial Priors in Microwave Imaging via Multiplicative Regularization”. In: *IEEE Transactions on Antennas and Propagation* 68.2 (2020), pp. 1107–1118. DOI: 10.1109/TAP.2019.2943329.

[142] A. H. Golnabi, P. M. Meaney, and K. D. Paulsen. “Tomographic Microwave Imaging With Incorporated Prior Spatial Information”. In: *IEEE Transactions on Microwave Theory and Techniques* 61.5 (2013), pp. 2129–2136. DOI: 10.1109/TMTT.2013.2247413.

[143] V. Kolehmainen, M. J. Ehrhardt, and S. R. Arridge. “Incorporating structural prior information and sparsity into EIT using parallel level sets”. In: *Inverse Problems & Imaging* 13 (2019), p. 285.

[144] A. Omrani et al. “Multistatic Uniform Diffraction Tomography Derived Structural-Prior in Bayesian Inversion Framework for Microwave Tomography”. In: *IEEE Transactions on Computational Imaging* 8 (2022), pp. 986–995. DOI: 10.1109/TCI.2022.3212835.

[145] Y. Zhang, A. Omrani, R. Yadav, and M. Fjeld. “Supporting Visualization Analysis in Industrial Process Tomography by Using Augmented

Reality—A Case Study of an Industrial Microwave Drying System". In: *Sensors* 21.19 (2021). ISSN: 1424-8220. DOI: 10.3390/s21196515.

[146] R. Yadav. "Neural network and Bayesian inversion methods for industrial process imaging using microwave tomography". PhD thesis. Itä-Suomen yliopisto, 2022.

[147] J. Kaipio and E. Somersalo. *Statistical and Computational Inverse Problems*. Springer-Verlag, 2005.

[148] R. Autieri, G. Ferraiuolo, and V. Pascazio. "Bayesian Regularization in Nonlinear Imaging: Reconstructions From Experimental Data in Nonlinearized Microwave Tomography". In: *IEEE Transactions on Geoscience and Remote Sensing* 49.2 (2011), pp. 801–813. DOI: 10.1109/TGRS.2010.2059705.

[149] S. Caorsi, G. L. Gragnani, S. Medicina, M. Pastorino, and G. Zunino. "Microwave imaging based on a Markov random field model". In: *IEEE Transactions on Antennas and Propagation* 42.3 (1994), pp. 293–303. DOI: 10.1109/8.280714.

[150] A. Franchois and C. Pichot. "Microwave imaging-complex permittivity reconstruction with a Levenberg-Marquardt method". In: *IEEE Transactions on Antennas and Propagation* 45.2 (1997), pp. 203–215. ISSN: 0018-926X. DOI: 10.1109/8.560338.

[151] C Eyraud, A Litman, A Hérique, and W Kofman. "Microwave imaging from experimental data within a Bayesian framework with realistic random noise". In: *Inverse Problems* 25.2 (2009), p. 024005. DOI: 10.1088/0266-5611/25/2/024005.

[152] H. Rue and L. Held. *Gaussian Markov Random Fields: Theory And Applications (Monographs on Statistics and Applied Probability)*. Chapman Hall/CRC, 2005. ISBN: 1584884320.

[153] C. Rasmussen and C. Williams. *Gaussian Processes for Machine Learning*. The MIT Press, 2006.

[154] R. Yadav, A. Omrani, M. Vauhkonen, G. Link, and T. Lähivaara. "Microwave tomography for moisture level estimation using Bayesian framework". In: *2021 15th European Conference on Antennas and Propagation (EuCAP)*. 2021, pp. 1–5. DOI: 10.23919/EuCAP48036.2020.9135296.

Acknowledgment

So remember Me; I will remember you. Quran S. 2. 152.

I am reminded of the importance of gratitude and remembrance at every step of my journey. With this in mind, I want to express my deepest gratitude to all those who have supported me throughout the journey of completing this thesis.

First and foremost, I would like to express my sincere appreciation to my advisor, Prof. John Jelonnek. His expertise, guidance, and unwavering support have been invaluable. Prof. Jelonnek's insightful feedback and encouragement have significantly shaped this research and contributed to my academic and personal growth. I am deeply grateful for his patience, motivation, countless hours he devoted to me, and real-life lessons. Thank you John!

I am also profoundly grateful to Prof. Mahmoud Shahabadi for his valuable input and assistance. His extensive knowledge and critical insights have vastly enhanced the quality of this research. Prof. Shahabadi's willingness to share his expertise and give helpful and detailed feedback has played a key role in improving my work and expanding the scope of my research.

A special thank you goes to Dr. Guido Link for his kind continuous support and collaboration. Guido's contributions and suggestions have been crucial in completing this thesis. His dedication, encouragement and fruitful discussions have continuously inspired and motivated me. Thank you, Guido, for all the wonderful times we've shared at KIT, in the mountains, or on various trips.

I am thankful to my friends for their unwavering support and encouragement throughout this journey. In particular, Masoud Safari, Dr. Ashkan Azarfar, Mostafa Vahdani, Dr. Rahul Yadav, Dr. Yuchong Zhang, Dr. Pana-

giotis Koulountzios, Vahid Khorashadi-zadeh, Dr. Hadi Mataji, Dr. Sajjad Sadeghi, Dr. Hamidreza Neshasteh, Dr. Sadegh Jalali, Javad Ebrahimi-Zadeh, Mehdi Aghajani, Mohsen Oladpur, and Saeed Aghapour.
I want to also thank all the members of the IHM for their support, in particular, Dominik Neumaier, Dr. Vasileios Ramopoulos, Dr. Nanya Li, Dr. Alexander Marek, Benjamin Ell, Moritz Engler, Lukas Feuerstein, Max Vöhringer, Lucas Silberer, Dr. Laurent Krier, and Dr. Chuanren Wu. Their companionship and words of motivation have been a source of strength for me.

Finally, I am deeply grateful to my family and my wife. Their love, patience, and understanding have been my foundation and have made this achievement possible. Their belief in me has been a driving force behind my efforts. To all of you, I extend my heartfelt thanks.

KARLSRUHER FORSCHUNGSBERICHTE AUS DEM
INSTITUT FÜR HOCHLEISTUNGSIMPULS- UND MIKROWELLENTECHNIK
(ISSN 2192-2764)

Band 1 MATTHIAS BERINGER
Design Studies towards a 4 MW 170 GHz Coaxial-Cavity Gyrotron.
ISBN 978-3-86644-663-2

Band 2 JENS FLAMM
Diffraction and Scattering in Launchers of
Quasi-Optical Mode Converters for Gyrotrons.
ISBN 978-3-86644-822-3

Band 3 MATTIA DEL GIACCO
Investigation of Fretting Wear of Cladding Materials in Liquid Lead.
ISBN 978-3-86644-960-2

Band 4 AMITAVO ROY CHOUDHURY
Investigations of After Cavity Interaction in Gyrotrons
Including the Effect of Non-uniform Magnetic Field.
ISBN 978-3-7315-0129-9

Band 5 MICHAEL BETZ
The CERN Resonant WISP Search (CROWS).
ISBN 978-3-7315-0199-2

Band 6 ANDREAS SCHLAICH
Time-dependent spectrum analysis of high power gyrotrons.
ISBN 978-3-7315-0375-0

Band 7 DHIDIK PRASTIYANTO
Temperature- and Time-Dependent Dielectric Measurements
and Modelling on Curing of Polymer Composites.
ISBN 978-3-7315-0424-5

Band 8 YIMING SUN
Adaptive and Intelligent Temperature Control of Microwave
Heating Systems with Multiple Sources.
ISBN 978-3-7315-0467-2

Die Bände sind unter www.ksp.kit.edu als PDF frei verfügbar oder als Druckausgabe bestellbar.

Band 9 **JIANGHUA ZHANG**
Influence of Emitter surface roughness and Emission inhomogeneity
on Efficiency and stability of high power Fusion gyrotrons.
ISBN 978-3-7315-0578-5

Band 10 **ANTON MALYGIN**
Design and Experimental Investigation of a Second Harmonic 20 kW Class
28 GHz Gyrotron for Evaluation of New Emitter Technologies.
ISBN 978-3-7315-0584-6

Band 11 **JOACHIM FRANCK**
Systematic Study of Key Components for a Coaxial-Cavity
Gyrotron for DEMO.
ISBN 978-3-7315-0652-2

Band 12 **PARTH CHANDULAL KALARIA**
Feasibility and Operational Limits for a 236 GHz Hollow-Cavity
Gyrotron for DEMO.
ISBN 978-3-7315-0717-8

Band 13 **CHUANREN WU**
Conceptual Studies of Multistage Depressed Collectors for Gyrotrons.
ISBN 978-3-7315-0934-9

Band 14 **MARTIN HOCHBERG**
A high-voltage pulsed power modulator
for fast-rising arbitrary waveforms.
ISBN 978-3-7315-0958-5

Band 15 **SEBASTIAN RUESS**
Pushing the KIT 2 MW Coaxial-Cavity Short-Pulse
Gyrotron Towards a DEMO Relevant Design.
ISBN 978-3-7315-1024-6

Band 16 **VASILEIOS RAMOPOULOS**
Energy-efficient, scalable and modular industrial microwave
applicator for high temperature alkaline hydrolysis of PET.
ISBN 978-3-7315-1099-4

Band 17 **ALEXANDER MAREK**
New Type of sub-THz Oscillator and Amplifier Systems Based on
Helical-Type Gyro-TWTs.
ISBN 978-3-7315-1250-9

Die Bände sind unter www.ksp.kit.edu als PDF frei verfügbar oder als Druckausgabe bestellbar.

Band 18 TOBIAS RUESS
A First 2 MW-Class (136)/170/204 GHz Multi-Frequency
Gyrotron Pre-Prototype for DEMO: Design, Construction and
Key Components Verification.
ISBN 978-3-7315-1309-4

Band 19 FABIAN WILDE
Automated Mode Recovery and Electronic Stability Control
for Wendelstein 7-X Gyrotrons.
ISBN 978-3-7315-1160-1

Band 20 JULIA HOFELE
Multi-Physics Modelling towards the Stabilization of PAN Fibers
with Microwaves Based on Experimental Data.
ISBN 978-3-7315-1350-6

Band 21 ADEL OMRANI HAMZEKALAEI
Multistatic Uniform Diffraction Tomography and Time-Reversal Algorithms
for Microwave Imaging of Multilayered Media.
ISBN 978-3-7315-1395-7

Die Bände sind unter www.ksp.kit.edu als PDF frei verfügbar oder als Druckausgabe bestellbar.

Karlsruher Forschungsberichte aus dem Institut für Hochleistungsimpuls- und Mikrowellentechnik
Herausgeber: Prof. Dr.-Ing. John Jelonnek

In this work, a novel application of microwave imaging to microwave drying systems is introduced, overcoming industrial constraints and realtime data demands. Dr.-Ing. Adel Omrani developed novel imaging algorithms that are compatible with low number of antenna arrays and improved spatial resolution. The introduction of the Multistatic Uniform Diffraction Tomography (MUDT) algorithm offers significant advancements, providing real-time imaging with better spatial resolution and compatibility with low numbers of antennas.
Furthermore, Dr.-Ing. Adel Omrani extends existing algorithms to address high-contrast scenarios in multilayered media, enhancing the capability of microwave imaging in complex environments. A real-time method is introduced to extract dielectric information from the imaging domain. This work advances the field of microwave imaging and opens new possibilities for microwave drying systems and beyond, promising developments in real-time imaging technology.

Adel Omrani received the B.Sc. and M.Sc. degrees in Electrical Engineering from Babol Noshirvani University of Technology, and the University of Tehran in 2014 and 2017, respectively. In 2018, he joined the Institute for Pulsed Power and Microwave Technology (IHM), receiving his Dr.-Ing. degree in the KIT Department of Electrical Engineering and Information Technologies in 2024.

ISBN 978-3-7315-1395-7
9 783731 513957

ISSN 2192-2764
ISBN 978-3-7315-1395-7

Gedruckt auf FSC-zertifiziertem Papier